NASA TECHNICAL NOTE

NASA TN D-2776

DETERMINATION OF TRAJECTORY AND ANGLES OF ATTACK OF A SCOUT HEAT-TRANSFER SPACECRAFT DURING REENTRY FLIGHT IN THE ATMOSPHERE

by Robert J. Mayhue

Langley Research Center

Langley Station, Hampton, Va.

NATIONAL AERONAUTICS AND SPACE ADMINISTRATION • WASHINGTON, D. C. • MAY 1965

NASA TN D-2776

DETERMINATION OF TRAJECTORY AND ANGLES OF ATTACK OF A SCOUT HEAT-TRANSFER SPACECRAFT DURING REENTRY FLIGHT IN THE ATMOSPHERE

By Robert J. Mayhue

Langley Research Center
Langley Station, Hampton, Va.

NATIONAL AERONAUTICS AND SPACE ADMINISTRATION

For sale by the Clearinghouse for Federal Scientific and Technical Information
Springfield, Virginia 22151 – Price $3.00

DETERMINATION OF TRAJECTORY AND ANGLES OF ATTACK OF A SCOUT HEAT-TRANSFER SPACECRAFT DURING REENTRY FLIGHT IN THE ATMOSPHERE

By Robert J. Mayhue
Langley Research Center

SUMMARY

A five-stage Scout reentry spacecraft experienced large-amplitude motions during the experimental heating data period as the result of disturbances from a fourth-stage motor failure. Downrange tracking radar failed to acquire the thrusting spacecraft at separation and tracking data for the experiment were limited to partial optical measurements from Bermuda. In order to evaluate the heat-transfer data obtained during the experiment, an analysis of the spacecraft unknown reentry trajectory and angles of attack was made primarily on the basis of telemetered measurements of the spacecraft linear accelerations and angular velocities. Computational procedures established for the analysis individually employed both the flight measurements and the aerodynamic characteristics of the spacecraft from preflight wind-tunnel tests.

The results of the analysis indicated that the spacecraft entered the heating data period with a velocity of about 22 230 feet per second at an altitude of approximately 308 000 feet. These flight conditions were 3 800 feet per second lower in velocity, and at an altitude which was 51 000 feet higher than desired as the result of fourth-stage motor failure. The spacecraft maximum angle of attack at the beginning of the heating data period was approximately 40°, but damped to about 23° at the time the nose cap burned off. After the nose cap burned off, the resultant angle of attack was reduced further to a maximum of about 6° at maximum dynamic pressure, and indicated that the spacecraft was statically and dynamically stable throughout the experimental heating data period.

INTRODUCTION

As part of a general research program on reentry heating, the Langley Research Center has conducted a free-flight test of a blunt-nose conical spacecraft using the five-stage Scout booster vehicle. A malfunction of the fourth-stage rocket motor during the flight test caused premature separation of the spacecraft with large-amplitude coning motions. Tracking radar at Bermuda failed

to acquire the spacecraft at separation, and tracking data for the experiment was limited to 4 seconds of optical measurements of the spacecraft angular position relative to the Bermuda optical tracking station.

The purpose of this report is to describe the results obtained, and the methods employed, in the determination of the unknown trajectory and angles of attack of the spacecraft that were required for evaluation of the heat-transfer measurements. These results were based primarily on analysis of rate gyro and accelerometer measurements recorded during the experiment and were used for analysis of the heat-transfer measurements as reported in reference 1.

The analysis of this report involved many unknown initial conditions and required the use of trial-and-error procedures in order to obtain results from the flight measurements which were consistent with the wind-tunnel aerodynamic characteristics of the spacecraft. The procedures and results that are presented and discussed are as follows:

(1) Integration of the rate gyro and accelerometer measurements,

(2) Simulation of the experimental measurements using wind-tunnel aerodynamics, and

(3) Comparison of the forces and moments computed from the flight measurements with those obtained from wind-tunnel tests.

SYMBOLS

a_L	longitudinal acceleration, g units
$a_{L,D}$	longitudinal acceleration of center of gravity (high-range accelerometer), g units
$a_{L,T}$	longitudinal acceleration of center of gravity (low-range accelerometer), g units
a_N	normal acceleration of center of gravity, g units
a_R	resultant acceleration of center of gravity, g units
a_T	transverse acceleration of center of gravity, g units
C_X, C_Y, C_N	total-force coefficients along X, Y, and Z body axes, respectively
C_R	resultant-force coefficient in body-axis Y,Z plane
C_{m_t}	resultant moment coefficient in body-axis Y,Z plane

C_{N_q}, C_{Y_r}	force coefficients along Y and Z body axes due to pitching and yawing velocities, respectively
C_{m_q}, C_{n_r}	moment coefficients along Y and Z body axes due to pitching and yawing velocities, respectively
d	maximum cross-sectional reference diameter, 1.673 ft
F_X, F_Y, F_Z	total-force components along X, Y, and Z body axes, respectively, lb
$F_{X_A}, F_{Y_A}, F_{Z_A}$	aerodynamic-force components along X, Y, and Z body axes, respectively, lb
G_X, G_Y, G_Z	gravity-force components along X, Y, and Z body axes, respectively, lb
g	acceleration due to gravity at altitude, ft/sec^2
g_o	acceleration due to gravity at surface of earth, ft/sec^2
h	altitude, ft
I_X, I_Y, I_Z	mass moment of inertias about X, Y, and Z body axes, respectively
L	North latitude measured positive from equatorial plane, deg or rad
l_i, m_i, n_i	Euler angle direction cosines between spacecraft body-axis system and local gravity-axis system
M	Mach number
$M_{X_A}, M_{Y_A}, M_{Z_A}$	aerodynamic moments about X, Y, and Z body axes, respectively, ft-lb
m	mass, slugs
$\bar{q}$	free-stream dynamic pressure, lb/sq ft
p,q,r	angular velocities about X, Y, and Z body axes, respectively, rad/sec or deg/sec
R_o	spherical earth radius, 20.890150×10^6 ft
S	maximum cross-sectional reference area, 2.197 sq ft
T	thrust, lb
t	flight time, sec
u,v,w	inertial velocity components along X, Y, and Z body axes, respectively
$\bar{V}$	earth-relative velocity, ft/sec

W	weight, lb
X_g, Y_g, Z_g	orthogonal gravity-axis coordinate system with origin at center of gravity
X, Y, Z	orthogonal body-axis coordinate system with origin at center of gravity
x_{cg}	longitudinal position of center of gravity measured from nose, ft
x_{cp}	longitudinal position of center of pressure measured from nose, ft
α	angle of attack, deg
β	angle of yaw, deg
η	resultant angle of attack, deg
$\bar{\gamma}$	earth-relative flight-path angle, rad or deg
$\bar{\epsilon}$	earth-relative heading angle measured positive from East to South, rad or deg
λ	West longitude measured negative from Greenwich meridian, deg or rad
ρ	free-stream density, slug/cu ft
τ	aerodynamic phase angle, deg
ω_e	angular velocity of rotating earth, 7.292115×10^{-5} rad/sec
θ, ψ, ϕ	spacecraft attitude angles relative to gravity-axis system, rad or deg
Ω	resultant spacecraft attitude angle in θ, ψ plane, rad or deg
ξ	amplitude of coning motion, rad or deg

Subscripts:

o	initial conditions
max	maximum condition
min	minimum condition
b	burnout

A dot over a symbol denotes differentiation with respect to time. Bars indicate earth-relative values.

SPACECRAFT AND INSTRUMENTATION

Spacecraft Description

The spacecraft configuration consisted of a symmetrical blunt-nose, low-fineness-ratio, conical body with a 9° half-angle as illustrated in figure 1. A NOTS 100B 17-inch spherical rocket motor was incorporated in the spacecraft as the final thrusting stage of the Scout ST-8 booster system. An inconel nose cap calorimeter was installed to measure heat-transfer data at the beginning of reentry into the atmosphere. This cap subsequently burned off to expose a new configuration with a Teflon nose cap. Thermal protection for the side walls consisted of a Teflon skin bonded on a magnesium shell.

The mass characteristics of the dynamically balanced spacecraft were obtained from preflight measurements and are listed for each fifth-stage flight event in the following table:

Table I

Flight event	Weight, lb	x_{cg}, from base, in.	$I_Y = I_Z$, slug-ft^2	I_X, slug-ft^2
Fifth-stage ignition	296.25	14.89	6.83	2.12
Fifth-stage burnout	155.45	20.33	3.93	1.31
Inconel nose cap off	146.97	19.74	3.67	1.25

Spacecraft Instrumentation

Telemetered instrumentation was installed in the spacecraft to provide continuous measurements of linear acceleration and angular velocity along each body axis. Accelerometers were alined and fixed near the spacecraft center of gravity, and rate gyros were alined and fixed on the axes about which the mass moments of inertia were taken. The body-axis coordinate system and the sign convention used for the measurements along each axis are shown in figure 2. Ranges selected for the instrumentation are given in the following table:

Table II

Measurement	Range
Longitudinal acceleration:	
(a) High range, $a_{L,D}$	+1g to -60g
(b) Low range, $a_{L,T}$	0 to 10g
Transverse acceleration, a_T . .	+5g to -5g
Normal acceleration, a_N	+5g to -5g
Rate of pitch, q	+100 deg/sec to -100 deg/sec
Rate of yaw, r	+100 deg/sec to -100 deg/sec
Rate of roll, p	1,200 deg/sec

The displacements of the accelerometers from the spacecraft center of gravity during fifth-stage flight events were measured prior to launch and are given in the following table:

Table III

Measurement	Displacement from center of gravity,* ft, of -		
	ΔX	ΔY	ΔZ
Fifth-stage ignition			
$a_{L,T}$	0.6601	0	-0.0427
$a_{L,D}$	.6601	0	.0427
a_T	.5215	-.1538	0
a_N	.5221	0	-.0036
Fifth-stage burnout			
$a_{L,T}$	0.2067	0	-0.0427
$a_{L,D}$	.2067	0	.0427
a_T	.0682	-.1538	0
a_N	.0687	0	-.0036
Nose cap off			
$a_{L,T}$	0.2559	0	-0.0427
$a_{L,D}$	.2559	0	.0427
a_T	.1173	-.1538	0
a_N	.1179	0	-.0036

*Sign convention shown in figure 2.

Ground Facilities

The primary data acquisition was obtained from facilities located at Coopers Island in the Bermuda tracking network. Tracking equipment consisted of an FPS-16 radar and ballistic streak and sequence cameras for optical coverage. Radar acquisition of the spacecraft at separation from the fourth stage was to have been accomplished by means of skin track.

Meteorological data were obtained from Coopers Island with sounding rocket launches conducted before and after the flight test.

Accuracy

Errors in the rate-gyro and accelerometer measurements were estimated to be ±2 percent of the instrumentation full-scale range and are listed in the following table:

Table IV

Measurement	Error
Longitudinal acceleration:	
(a) High range, $a_{L,D}$	±1.22g
(b) Low range, $a_{L,T}$	±0.20g
Transverse acceleration, a_T . .	±0.10g
Normal acceleration, a_N	±0.10g
Rate of pitch, q	±2.0 deg/sec
Rate of yaw, r	±2.0 deg/sec
Rate of roll, p	±24.00 deg/sec

No attempt was made to estimate the accuracy of the radar tracking measurements, since radar failed to acquire the spacecraft at separation and continued to track the burned-out fourth stage. Errors in the optical tracking angular measurements obtained during the experiment were believed to be negligible and were therefore used directly as a primary checkpoint for trajectory computations.

Measurements of the free-stream density and speed of sound obtained from meteorological instruments up to an altitude of about 200 000 feet were estimated to be accurate within approximately ±5 percent. These quantities were extrapolated to the higher reentry altitudes where the effect of these errors became less significant.

FLIGHT TEST

The nominal trajectory and flight events predicted for the experiment are described in figure 3. The mission requirement was to obtain a reentry relative velocity of about 26 000 feet per second at the end of fifth-stage thrusting. The heating data period was to begin at this time at an altitude of about 257 000 feet with a relative flight-path angle of approximately -14.0°.

The actual trajectory and events that occurred during the experiment were as expected up through spinup and ignition of the fourth-stage rocket motor. About halfway through the fourth-stage thrusting period, however, a loss of thrust occurred and was accompanied by large-amplitude oscillations of the vehicle. The analysis of reference 2 showed that this event was caused by a blowout of the fourth-stage motor case which produced large moment disturbances

and loss of rocket-motor chamber pressure. The moments during thrust termination caused the vehicle to diverge to a maximum angle of attack of about 58°, and loss of chamber pressure caused premature ignition of the spacecraft spherical rocket motor through a pressure-decay arming switch.

Bermuda radar which had been beacon tracking the vehicle failed to acquire the thrusting spacecraft as it separated and accelerated away from the fourth stage. Tracking data obtained during the experiment were therefore limited to optical measurements from Bermuda which were obtained about 16 seconds after burnout of the spacecraft spherical rocket motor. These measurements did not provide specific trajectory coordinates, but were restricted to angular measurements of the spacecraft azimuth and elevation relative to the tracking station at 1-second intervals from 436 seconds to 440 seconds of flight time.

Telemetered accelerometer and rate-gyro measurements were recorded during the reentry flight of the spacecraft and are presented in figures 4 to 8. Figure 4 presents time histories of the spacecraft angular velocities from fifth-stage ignition through about 73 seconds of coasting flight. Ignition of the fifth-stage motor occurred at 377.85 seconds with burnout at about 420.85 seconds. Predicted times for these events were 393.8 seconds and 436.8 seconds, respectively. Cross plots of the rate-gyro measurements during fifth-stage thrusting and the beginning of coasting flight are presented in figure 5. Figure 5(a) illustrates the large-amplitude circular coning motions, with jet damping effects that were experienced by the spacecraft during thrusting of the fifth-stage motor. After motor burnout, figure 5(b) shows that the spacecraft entered the heating data period with residual coning motions, and continued to oscillate with increasing angular velocities as indicated by figures 5(c) and 5(d). A sudden change in the amplitude of the angular velocities was observed at about 439 seconds in figure 5(d) which indicated burnoff of the inconel nose cap. This event was verified by the start of heating measurements on the exposed Teflon nose as reported in reference 1. Continuation of the cross plots of the rate gyro measurements through maximum dynamic pressure is shown in figures 5(c) to 5(m).

Figure 6 presents time histories of the spacecraft normal and transverse accelerations along the Y and Z body axes, as well as the resultant of these accelerations in the Y,Z plane. Cross plots of these measurements during coasting flight in the atmosphere through maximum acceleration are presented in figure 7. Longitudinal accelerations along the X body axis are presented in figure 8 from fifth-stage ignition through maximum acceleration of about -48.6g units. All accelerometer data presented in figures 6 to 8 were corrected for errors due to displacement of the instrumentation from the spacecraft center of gravity.

It should be noted in figures 4 and 6 that the ranges of the rate gyros and accelerometers were exceeded and that the peak values were faired during the time intervals indicated. Fairings through data noise periods were also required at other time intervals as shown.

Figures 9 and 10 present free-stream atmospheric data obtained from Bermuda radiosonde and sounding rocket measurements. A comparison of the

measured values with 1959 ARDC 1962 standard atmosphere is included. This comparison indicated that the measured density became increasingly lower than standard through the altitude range that measurements were obtained. Extrapolation of the free-stream density to the higher altitudes, therefore, was based on an increasing percentage deviation as shown in figure 9. The values for speed of sound presented in figure 10, based on the free-stream temperature shown, were used to determine Mach number variations during all reentry trajectory computations.

The time history of the spacecraft weight during thrusting of the NOTS 100-B spherical rocket motor was computed from the longitudinal accelerometer measurements and predicted specific impulse of the motor. No drag or thrust misalinement being assumed, the computed propellant weight time history is presented and compared with predicted nominal values in figure 11. Since comparison with the predicted nominal indicated good agreement, these data were used to compute time histories of the spacecraft weight, center of gravity, and moments of inertia as presented in figure 12. Initial values for these quantities were obtained from preflight measurements of the spacecraft mass characteristics.

Figure 13 presents the thrust time history of the NOTS 100-B motor as computed from longitudinal accelerometer measurements and the spacecraft weight variation in figure 12. Comparison of the computed thrust with predicted nominal values indicated that the thrust level during flight was slightly higher, and thrust tail-off occurred about 3 seconds earlier than predicted.

METHOD OF ANALYSIS

Computational Procedures

A knowledge of the reentry trajectory and angles of attack was required for analysis of the primary heat-transfer measurements for about the first 19 seconds of coasting flight. Flight times for this data period were from burnout of the fifth-stage motor at about 421 seconds to loss of the calorimeter nose cap at approximately 439 seconds. Trajectory and angle-of-attack computations to 460 seconds were also required for evaluation of ablation measurements through maximum dynamic pressure.

Computation of the unknown trajectory and angles of attack of the spacecraft by means of the rate gyro and accelerometer measurements presented a problem involving many unknown initial conditions. Extensive trial-and-error analysis using the two independent computational procedures was therefore required. The first computation, described in detail in reference 2 and appendix A of this report, was based on continuous integration of the rate-gyro and accelerometer measurements which provided increments of body-axis inertial velocities during the flight. The spacecraft aerodynamics were not required in this computation, and the aerodynamic forces and moments derived from these results were dependent on initial conditions. Constraints were imposed, therefore, which required that the aerodynamic characteristics derived from

integration of the rate-gyro and accelerometer measurements must be consistent with those from preflight wind-tunnel tests of reference 3.

In order to monitor results from integration of the flight measurements, and to conduct initial-condition studies, a second independent computational procedure using wind-tunnel aerodynamics was established for the analysis. This computation was a six-degree-of-freedom analog simulation of the flight measurements during coasting flight in the atmosphere and is described in appendix B.

Initial Conditions

If the Bermuda radar measurements of the spacecraft position coordinates at fifth-stage ignition were used, the equations of appendix A show that computation of the trajectory and angles of attack from rate-gyro and accelerometer measurements required six unknown initial conditions involving the body-axis inertial velocities u_o, v_o, and w_o and the Euler attitude angles θ_o, ψ_o, and ϕ_o.

Since the pitch and yaw rate-gyro measurements near fifth-stage ignition were essentially sinusoidal, circular coning motions being indicated, the initial Euler angles were varied in the analysis by trial-and-error displacement of the coning motion from the velocity vector. The objective of this investigation was to determine the spacecraft thrusting attitude variations which would result in flight through the azimuth and elevation angles from Bermuda that were measured 16 to 20 seconds after burnout. In addition, trajectory increments as the result of thrusting off the velocity vector were required that would generate a dynamic-pressure time history compatible with wind-tunnel longitudinal-force data as illustrated by the following equation:

$$C_X = \frac{1}{\bar{q}}\left(\frac{Wa_{L,D}}{S}\right) \tag{1}$$

Determination of a trajectory which would result in agreement with Bermuda optical tracking measurements depended on the time histories of the spacecraft latitude, longitude, and altitude which varied according to the following equations:

$$\left.\begin{aligned} L &= L_o + \int -\frac{\bar{V}\cos\bar{\gamma}\sin\bar{\epsilon}}{R_o + h}\,dt \\ \lambda &= \lambda_o + \int \frac{\bar{V}\cos\bar{\gamma}\cos\bar{\epsilon}}{(R_o + h)\cos L}\,dt \\ h &= h_o + \int \bar{V}\sin\bar{\gamma}\,dt \end{aligned}\right\} \tag{2}$$

Equation (1) shows that for a given variation of velocity, the longitudinal-force coefficient derived from the computed dynamic pressure was dependent only on the density-altitude relationship specified by the flight-path-angle variation. The spacecraft position coordinates computed from equations (2), however, were dependent on the combined variations of heading and flight-path angles. Therefore, various coning-axis locations in the θ,ψ plane were assumed (see following sketch) until the interchange of heading and flight-path-angle increments during thrusting, as well as the velocity and altitude increments, yielded a reentry coasting trajectory in the atmosphere that agreed with optical and wind-tunnel measurements.

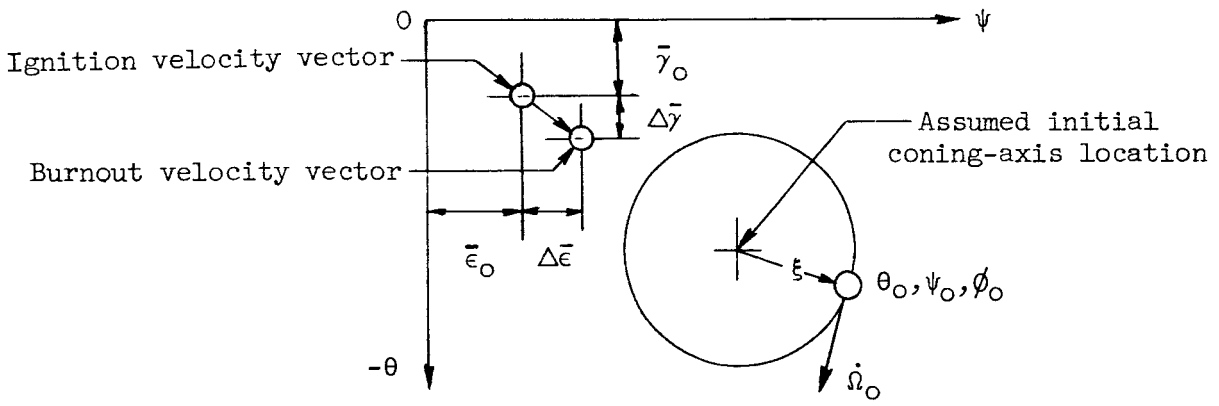

The amplitude of the initial displaced coning motion was estimated by assuming that no external moments were present near ignition, and that the motions were centered about a total angular momentum vector fixed in space at the coning axis. The initial coning amplitude was then defined by the following expression for the angle between the spacecraft spin axis and the total angular momentum vector:

$$\tan \xi = \frac{I_Y \sqrt{q_o^2 + r_o^2}}{p_o I_X} \tag{3}$$

The starting point on the coning circle at θ_o,ψ_o and the tangent slope $\dot{\Omega}_o$ at this point were chosen graphically in order to generate motions about the selected coning-axis orientation. The initial roll angle ϕ_o required to produce the initial slope $\dot{\Omega}_o$ was computed from the following expressions:

$$\left.\begin{aligned} \dot{\theta}_o &= q_o \cos \phi_o - r_o \sin \phi_o \\ \dot{\psi}_o &= \frac{r_o \cos \phi_o + q_o \sin \phi_o}{\cos \theta} \end{aligned}\right\} \tag{4}$$

where solving for ϕ_o gives:

$$\phi_o = \tan^{-1}\left(-\frac{\frac{r_o}{\cos\theta_o}\dot{\Omega}_o - q_o}{\frac{q_o}{\cos\theta_o}\dot{\Omega}_o + r_o}\right) \tag{5}$$

and

$$\dot{\Omega}_o = \frac{\dot{\theta}_o}{\dot{\psi}_o} \tag{6}$$

The initial pitch and yaw rates were obtained from rate-gyro measurements, and the quadrant of ϕ_o was determined by the sign of the individual slopes $\dot{\theta}_o$ and $\dot{\psi}_o$ in equations (4).

For a given set of initial Euler angles, the direction cosines for transformation of quantities in the gravity-axis system to the body-axis system were computed from equations (A9) in appendix A. The initial body-axis inertial velocities were then determined from the following equations:

$$\left.\begin{aligned} u_o &= \dot{X}_{g_o} l_1 + \dot{Y}_{g_o} l_2 - \dot{h}_o l_3 \\ v_o &= \dot{X}_{g_o} m_1 + \dot{Y}_{g_o} m_2 - \dot{h}_o m_3 \\ w_o &= \dot{X}_{g_o} n_1 + \dot{Y}_{g_o} n_2 - \dot{h}_o n_3 \end{aligned}\right\} \tag{7}$$

where the inertial velocities in the gravity-axis system were found from the equations:

$$\left.\begin{aligned} \dot{X}_{g_o} &= \frac{\dot{Y}_{g_o}}{\tan\bar{\epsilon}_o} + (R_o + h)_o\,\omega_e \cos L_o \\ \dot{Y}_{g_o} &= \frac{\dot{h}_o \sin\bar{\epsilon}_o}{\tan\bar{\gamma}_o} \\ \dot{h}_o &= \bar{V}_o \sin\bar{\gamma}_o \end{aligned}\right\} \tag{8}$$

The spacecraft position coordinates X_{g_o}, Y_{g_o}, L_o, λ_o and velocity-vector magnitude and orientation $\bar{V}_o$, $\bar{\epsilon}_o$, $\bar{\gamma}_o$ required for solution and integration of equations (8) were obtained from Bermuda radar measurements at fifth-stage ignition.

Preliminary integration results.- An example of the results obtained from preliminary trial-and-error integration of the flight measurements during thrusting is shown in figure 14. The initial conditions at fifth-stage ignition used for this computation resulted in divergence in the motions after burnout and were unacceptable, since corresponding analog simulation indicated that the spacecraft motions near burnout always precessed toward and eventually damped around the velocity vector. Additional integrations were made by graphically rotating and translating the previous θ,ψ motion patterns until a possible solution of the spacecraft trajectory and motions during thrusting was obtained as shown in figure 15. Motions during thrusting are shown only near ignition and near burnout for clarity. The significant results of this integration was the discrepancy between the precessional characteristics of the motions after burnout that were computed from the flight measurements and wind-tunnel aerodynamics as shown in figures 16(a) and 16(b). Analog simulation results using wind-tunnel aerodynamics in figure 16(b) indicated that the oscillation amplitudes were larger than those obtained from integration of the flight measurements in figure 16(a). From the results of figure 17, which presents a comparison between the angles of attack computed from faired and unfaired roll-rate measurements, the differences between the motions in figures 16(a) and 16(b) were attributed to the differences in roll-rate input data. The motions computed from faired roll-rate measurements are presented in figure 16(c). These motions compared favorably with analog simulation results which generated angular rates with marked simularity to the measured rates up to 435 seconds as illustrated in figure 18.

Final initial conditions.- By using faired roll-rate input data, trial-and-error integration of the flight measurements were made through maximum dynamic pressure until initial conditions at fifth-stage ignition were found that provided the best agreement with Bermuda optical tracking measurements and the wind-tunnel aerodynamic characteristics of the spacecraft. The final initial conditions assumed for the analysis are presented in the following table:

Table V

Quantity	Initial condition at -	
	Ignition	Burnout
Flight time, sec	377.85	420.85
$\bar{V}_o$, ft/sec	17 761	22 227
h_o, ft	557 800	308 082
$\bar{\gamma}_o$, deg	-13.69	-20.25
$\bar{\epsilon}_o$, deg	48.63	51.12
θ_o, deg	-54.70	-24.02
ψ_o, deg	81.70	80.37
ϕ_o, deg	65.24	33.40
u_o, ft/sec	11 479	19 953
v_o, ft/sec	-12 683	-9854
w_o, ft/sec	5512	5928
X_{g_o}, ft	311 693	887 446
Y_{g_o}, ft	272 448	891 156
λ_o, deg	-68.82	-67.18
L_o, deg	32.92	31.26

It should be noted that some of the radar measurements at fifth-stage ignition were revised for better agreement with Bermuda optical tracking measurements. The revised initial conditions are listed and compared with radar measurements in the following table:

Table VI

Quantity	Radar value	Revised value	Difference, percent
$\bar{V}_o$, ft/sec	17 104	17 761	-3.7
h_o, ft	563 582	557 800	1.0
$\bar{\gamma}_o$, deg	-13.69	-12.80	6.5
$\bar{\epsilon}_o$, deg	48.83	44.50	8.9

Although it was difficult to assess the errors in the radar measurements at the time of spacecraft separation and loss of radar tracking, the differences in the initial velocity and altitude are believed to be within the accuracy of the measurements. Since the radar measurements of initial latitude and longitude were assumed to be approximately correct, the largest changes required to obtain the best agreement with Bermuda optical tracking measurements were in the radar flight-path and heading angle as shown in figure 19. A comparison of the time histories of latitude and longitude is presented in figure 20. Although the revised initial flight-path angle in figure 19 appeared to be a reasonable extrapolation of earlier radar measurements, the difference in the initial heading angles was significant. However, a better match with Bermuda optical measurements was obtained with the revised heading angle as shown in figure 21. Although both radar and revised initial conditions gave good agreement in the elevation plane, a large change in initial heading angle was required to obtain closer agreement in the azimuth plane.

The dynamic-pressure time histories obtained from both flight-data integration and six-degree-of-freedom simulation with wind-tunnel aerodynamics are compared in figure 22. Agreement between integration and simulation values for both radar and revised initial conditions was good during the buildup to maximum dynamic pressure. Both values of longitudinal-force coefficient derived from integration results were within the scatter band of wind-tunnel test results. The differences after maximum dynamic pressure, however, indicated that the best agreement was obtained with revised fifth-stage initial conditions. In addition, the dynamic pressure computed from the measured acceleration and constant value of $C_X = 0.575$ was independent of initial conditions and agreed very well with both the integrated and simulation results. This comparison verified wind-tunnel predictions of constant longitudinal-force coefficient with Mach number up to angles of attack of about 20°.

Trajectory initial condition study.- In order to determine whether there was any other combination of initial conditions which would result in the final dynamic-pressure time history of figure 22, a six-degree-of-freedom analog study of the effects of altitude, velocity, and flight-path angle on the spacecraft acceleration time history was made starting at fifth-stage burnout. The

longitudinal-force coefficient of $C_X = 0.575$, derived from the final dynamic-pressure time history, was assumed to be constant with angle of attack and Mach number for this investigation. The spacecraft motions, therefore, had little effect on the acceleration time history since the displaced coning motions at burnout precessed toward the velocity vector and eventually damped to angles of attack of less than 20° early in the flight.

Families of reentry acceleration time histories were computed for a range of burnout altitudes, velocities, and flight-path angles. Two points on the acceleration time histories were assumed as necessary conditions for matching the flight measurements. These points consisted of the magnitude and time of occurrence of the maximum acceleration $a_{L,max}$ and maximum rate of change of acceleration $\dot{a}_{L,max}$. For each change of initial conditions, then, the magnitude of $a_{L,max}$ and $\dot{a}_{L,max}$ were determined at the same time that these quantities were measured during the flight. A summary grid of these results is presented in figure 23, which shows the variation of $a_{L,max}$ and $\dot{a}_{L,max}$ with burnout flight-path angles for various combinations of altitude and velocity at fifth-stage burnout. Figure 23 indicated that only one combination of altitude, velocity, and flight-path angle would result in an acceleration time history that would match the magnitude of both $a_{L,max}$ and $\dot{a}_{L,max}$ that were measured during the flight. This combination agreed very well with those determined from trial-and-error integration of the flight measurements, and verified the uniqueness of the final initial conditions used to compute the spacecraft trajectory and motions.

For other values of longitudinal-force coefficient within the scatter band of wind-tunnel test data, the velocity, altitude, and flight-path angle computed from the final initial conditions would be in error by approximately the amounts shown in figure 24. These errors represent a range of burnout flight conditions that would match the measured accelerations using wind-tunnel data and indicated that the final burnout velocity from integration of the flight measurements was within ± 420 feet per second with an altitude and flight-path angle range of ± 6200 feet and $\pm 0.4^\circ$, respectively. It is believed that these increments also indicated the overall accuracy of the computed trajectory, since these errors would be incremental throughout the coasting trajectory.

Data noise.- One of the problems encountered in integration of the flight measurements was the sudden shifts in the orientation of the computed motions, and divergence of the resultant angle-of-attack time history, as illustrated in figures 25(a) and 25(b). These results were caused by arbitrary fairing of telemeter measurements through noise periods which occurred at the flight times shown. New initial conditions were required, therefore, after each noise interval, and these conditions were determined by assuming that the motions were always around the velocity vector as indicated by earlier analog simulation studies. Table VII presents the initial conditions after each noise period required for integration of the flight measurements through maximum dynamic pressure.

Table VII

Quantity	Initial conditions	
Flight time, sec	434.05	447.45
$\bar{V}_o$, ft/sec	22 334	18 552
h_o, ft	205 734	105 436
$\bar{\gamma}_o$, deg	-20.43	-20.67
$\bar{\epsilon}_o$, deg	51.14	51.40
θ_o, deg	-13.60	-20.70
ψ_o, deg	67.35	47.60
ϕ_o, deg	161.25	231.56
u_o, ft/sec	21 890	19 334
v_o, ft/sec	7473	-29
w_o, ft/sec	-340	526

RESULTS AND DISCUSSION

Reentry Trajectory

Figure 26 presents the time histories of the spacecraft relative velocity and altitude computed from integration of the flight measurements using the final initial conditions of table V. These results are compared with measurements obtained from radar which was tracking the combined fourth and fifth stage before separation, and the burned-out fourth stage after separation. Comparison between radar and computed quantities shows that the spacecraft separated from the fourth stage and accelerated to a velocity of about 22 230 feet per second at burnout of the fifth-stage motor at an altitude of about 308 000 feet. These results indicated that the fourth-stage motor failure caused a loss in experimental velocity of about 3800 feet per second at the beginning of the heating data period near burnout at about 420 seconds flight time. The altitude at this time was higher than desired by approximately 51 000 feet. The variations of the Reynolds number and dynamic pressure with Mach number obtained during the experimental heating data period are presented in figure 27.

Spacecraft Motions

The motions of the spacecraft obtained from integration of the flight measurements during thrusting and coasting flight are shown by the Euler angle θ,ψ cross plots in figures 28(a) to 28(d). The motions are plotted with respect to a fixed gravity-axis system since the rotation of the axis system traveling with the spacecraft was negligible during the time intervals shown.

Figure 28(a) shows that the displacement of the coning axis at separation of the spacecraft was about 25° below and 5° to the right of the initial velocity vector. The coning half-angle at this time was approximately 26° and was damped during thrusting of the fifth-stage motor to about 14° at burnout. Damping of the motions did not occur symmetrically about a coning axis fixed in space, but was about an axis which precessed in the yaw direction and indicated the presence of asymmetric external moments during motor burning.

Figures 28(b) to 28(d) show the residual coning motions at burnout which precessed toward and eventually damped around the velocity vector as the aerodynamic restoring moments began to build up. It is interesting to note that the general shape of the motion pattern near burnout could have been established by integration of the flight measurements from the origin. For a given initial velocity vector, given attitude angle, and given attitude rate, the desired precession could then have been obtained by graphically translating and rotating the basic motion pattern as shown in figure 29.

Figure 30 presents the time history of the spacecraft angles of attack associated with the motions shown in figure 28. These results indicated that the spacecraft began coning at separation with a maximum resultant angle of attack of about 49°. The angle of attack decreased to about 34° during the first 27 seconds of thrusting, and then began to build up to a maximum of about 40° at burnout. This buildup appeared to start near the beginning of thrust tailoff and continued through burnout to about 426 seconds.

A comparison of the envelopes of the resultant angle of attack after burnout computed from the flight measurements and wind-tunnel aerodynamics is presented in figure 31. During the time nose-cap calorimeter data were being recorded from burnout to about 438 seconds, the analog simulation results showed good agreement with flight data integration. The maximum angle of attack during this time varied from 40° to about 23° and indicated that the spacecraft was statically and dynamically stable with the nose cap on. After the nose cap burned off, the results from flight-data integration showed a sudden change in amplitude of the oscillations which indicated that burnoff of the nose cap imparted an impulsive moment to the spacecraft in a direction to reduce the amplitude of the oscillations. Since the simulation did not account for this event, the angle-of-attack envelope continued at a higher level with amplitudes and trends similar to the integration results. Figures 30 and 31 show that the spacecraft angles of attack after the nose cap burned off continued to damp to a maximum of about 6° at maximum dynamic pressure. These results then indicated that the spacecraft was statically and dynamically stable throughout the experimental heating data period.

Aerodynamic Results and Comparisons

A check on the amplitude and phasing of the computed angle-of-attack time history, as well as the computed dynamic pressure, was obtained from comparison of wind-tunnel test results with force and moment coefficients derived from the accelerometer and rate-gyro flight measurements. Figure 32(a) presents the envelopes of the resultant-force-coefficient oscillations during flight in the

atmosphere with dynamic pressures greater than 100 lb/sq ft. Resultant angle-of-attack envelopes predicted by wind-tunnel tests for the flight resultant-force coefficients are compared with the angles of attack computed from integration of the flight data in figure 32(b). Fairly good agreement between the envelopes substantiated the trends and amplitudes of the final computed angle-of-attack time history.

The phasing of the computed angle-of-attack oscillations was checked by comparison of the flight force and moment coefficients with the static wind-tunnel results. Figure 33 presents comparisons with the nose cap on and off through a Mach number range from about $M = 20.6$ to $M = 9.7$. The arrows on the continuous flight data show the manner in which the spacecraft computed forces and moments varied with time. For a known configuration immediately before and after the nose cap burned off at about $M = 20.5$, the flight force and moment variations showed fairly good agreement with static wind-tunnel results as shown in figures 33(a) and 33(b). Agreement at the minimum and maximum oscillation peaks was also good. Although the flight data included dynamic effects, the similarity of the nonlinear characteristics of the data was especially noted. The resultant moment coefficients obtained from flight data in figure 33(a) indicated the presence of a trim and hysteresis effect prior to burnoff of the nose cap. After the transient moments due to burnoff of the nose cap disappeared, agreement between the wind-tunnel and flight moments was exceptionally good as shown in figure 33(b). Figure 33(c) is presented to illustrate the erratic variation of the computed forces and moments after the nose cap came off. Part of this behavior at the higher Mach numbers may be attributed to changes in the nose configuration as the result of ablation. Phasing errors or dynamic effects in the computed resultant angles of attack during this part of the flight may account for some of the discrepancies in the force comparisons. In general, however, the variations in the flight forces and moments were centered about the wind-tunnel static test results.

Figure 34 presents another comparison between the normal- and longitudinal-force coefficients from flight data and from wind-tunnel results. The flight normal-force coefficients and angles of attack in figure 34(a) were obtained from oscillation envelopes for angle of sideslip β approximately equal to zero. Again, the wind-tunnel results represented a good average for the computed flight data. The longitudinal-force coefficients are compared in figure 34(b) and showed that the flight values were within the scatter band of the results from various test facilities.

CONCLUDING REMARKS

An analysis of the Scout ST-8 spacecraft reentry trajectory and angles of attack during the experimental data period has been made based on partial downrange optical tracking data, preflight wind-tunnel aerodynamic test results, and flight measurements of the spacecraft linear accelerations and angular velocities. The results indicated by this analysis are summarized as follows:

1. The relative velocity attained by the spacecraft at the beginning of the primary heat-transfer data period was about 22 230 feet per second at an

altitude of approximately 308 000 feet. The initial experimental velocity was 3800 feet per second lower than nominal at an altitude which was 51 000 feet higher as the result of fourth-stage motor malfunction.

2. As the result of disturbances from fourth-stage motor failure, the spacecraft began coning at separation with a half-angle of about 26°. The coning axis at this time was displaced about 25° below and 5° to the right of the velocity vector. The maximum resultant angle of attack occurred near ignition and was approximately 49°. During the thrusting period, the maximum angles of attack damped to about 34° and then increased to about 40° as the spacecraft entered the heating data period near burnout.

3. The spacecraft maximum angles of attack during the primary heat-transfer data period varied from 40° near burnout to about 23° at the time the nose-cap calorimeter burned off. After this time, the maximum angles of attack continued to damp through the ablation data period to about 6° at maximum dynamic pressure. These results indicated that the spacecraft was statically and dynamically stable throughout the heating data period.

4. The force and moment coefficients corresponding to the computed trajectory and angles of attack were generally in good agreement with preflight wind-tunnel test results.

Langley Research Center,
National Aeronautics and Space Administration,
Langley Station, Hampton, Va., January 28, 1965.

APPENDIX A

EQUATIONS AND COMPUTATIONAL PROCEDURE FOR INTEGRATION OF RATE-GYRO AND ACCELEROMETER MEASUREMENTS

As described in reference 2, body-axis equations of motion with a local gravity-axis system fixed at the spacecraft center of gravity (fig. 2) were programed for a spherical rotating earth on an IBM 7090 electronic data processing machine. Rate-gyro and accelerometer flight measurements were continuously recorded on digital tape and used as input quantities in the equations of motion.

The accelerometer measurements, corrected for errors caused by displacement of the instrumentation from the spacecraft center of gravity (ref. 2), provided the body-axis external forces (total force less gravity force) as illustrated by the following equations:

$$\left.\begin{aligned} g_o a_L &= \frac{F_X}{m} - \frac{G_X}{m} \\ g_o a_T &= \frac{F_Y}{m} - \frac{G_Y}{m} \\ g_o a_N &= -\frac{F_Z}{m} + \frac{G_Z}{m} \end{aligned}\right\} \tag{A1}$$

where G_X, G_Y, and G_Z are the body-axis components of the spacecraft gravity force. The gravity forces were determined by introducing three unknown direction cosines as follows:

$$\left.\begin{aligned} G_X &= -W \sin\theta \\ G_Y &= W \cos\theta \sin\phi \\ G_Z &= W \cos\theta \cos\phi \end{aligned}\right\} \tag{A2}$$

With the use of equations (A1) and (A2), the body-axis inertial velocities were obtained from integration of the flight measurements (p, q, r, a_L, a_T, and a_N) with the following basic equations:

$$\left.\begin{aligned} u &= u_o + \int (g_o a_L - g_o \sin\theta + vr - wq)dt \\ v &= v_o + \int (g_o a_T + g_o \cos\theta \sin\phi + wp - ur)dt \\ w &= w_o + \int (-g_o a_N + g_o \cos\theta \cos\phi + uq - vp)dt \end{aligned}\right\} \quad (A3)$$

In order to determine the Euler angle direction cosines required for solution of equations (A3), the measured angular velocities p, q, and r were used in the following equations defining the spacecraft Euler angles:

$$\left.\begin{aligned} \theta &= \theta_o + \int (q \cos\phi - r \sin\phi + K_\theta)dt \\ \psi &= \psi_o + \int \left(\frac{r \cos\phi + q \sin\phi}{\cos\theta} + K_\psi\right)dt \\ \phi &= \phi_o + \int \left(p + \dot{\psi} \sin\theta + K_\phi\right)dt \end{aligned}\right\} \quad (A4)$$

where K_θ, K_ψ, and K_ϕ are the body-axis components of the angular velocity of the local gravity-axis system moving with the spacecraft with respect to an inertial reference. These quantities were a function of the spacecraft latitude and longitude as shown by the following equations:

$$\left.\begin{aligned} K_\theta &= \dot{L} \sin\psi - (\omega_e + \dot{\lambda})\cos L \cos\psi \\ K_\psi &= \dot{L} \cos\psi \tan\theta + (\omega_e + \dot{\lambda})(\sin L + \cos L \sin\psi \tan\theta) \\ K_\phi &= \dot{L} \frac{\cos\psi}{\cos\theta} + (\omega_e + \dot{\lambda})\cos L \frac{\sin\psi}{\cos\theta} \end{aligned}\right\} \quad (A5)$$

where

$$\left.\begin{aligned} L &= L_o + \int \dot{L}\, dt \\ \lambda &= \lambda_o + \int \dot{\lambda}\, dt \end{aligned}\right\} \quad (A6)$$

and

$$\left.\begin{aligned} \dot{L} &= -\frac{\dot{Y}_g}{R_o + h} \\ \dot{\lambda} &= \frac{\dot{X}_g}{(R_o + h)\cos L} - \omega_e \end{aligned}\right\} \tag{A7}$$

Transformation of the body-axis inertial velocities to the local gravity-axis system was determined as follows:

$$\begin{bmatrix} \dot{X}_g \\ \dot{Y}_g \\ \dot{Z}_g \end{bmatrix} = \begin{bmatrix} l_1 & m_1 & n_1 \\ l_2 & m_2 & n_2 \\ l_3 & m_3 & n_3 \end{bmatrix} \begin{bmatrix} u \\ v \\ w \end{bmatrix} \tag{A8}$$

where l_i, m_i, and n_i are the Euler angle direction cosines between the spacecraft body-axis system and the local gravity-axis system as determined by the following equations:

$$\left.\begin{aligned} l_1 &= \cos\theta \cos\psi \\ l_2 &= \cos\theta \sin\psi \\ l_3 &= -\sin\theta \\ m_1 &= \sin\theta \sin\phi \cos\psi - \cos\phi \sin\psi \\ m_2 &= \sin\theta \sin\phi \sin\psi + \cos\phi \cos\psi \\ m_3 &= \cos\theta \sin\phi \\ n_1 &= \sin\theta \cos\phi \cos\psi + \sin\phi \sin\psi \\ n_2 &= \sin\theta \cos\phi \sin\psi - \sin\phi \cos\psi \\ n_3 &= \cos\theta \cos\phi \end{aligned}\right\} \tag{A9}$$

and

$$\left.\begin{aligned} X_g &= X_{g_o} + \int \dot{X}_g \, dt \\ Y_g &= Y_{g_o} + \int \dot{Y}_g \, dt \\ Z_g &= Z_{g_o} + \int \dot{Z}_g \, dt \end{aligned}\right\} \tag{A10}$$

The spacecraft flight-path and heading angles were then computed from the following equations:

$$\left.\begin{aligned} \bar{\gamma} &= \sin^{-1}\left(-\frac{\dot{Z}_g}{\bar{V}}\right) \\ \bar{\epsilon} &= \tan^{-1}\left[\frac{\dot{Y}_g}{\dot{X}_g - (R_o + h)\omega_e \cos L}\right] \end{aligned}\right\} \tag{A11}$$

The magnitude of the earth-relative velocity in equation (A12) was determined, the assumption being made that no winds were present through the altitude range of the experiment, from the following equations:

$$\bar{V} = \sqrt{\bar{u}^2 + \bar{v}^2 + \bar{w}^2} \tag{A12}$$

where the earth-relative velocity components along the body axis were found from

$$\left.\begin{aligned} \bar{u} &= u - l_1(R_o + h)\omega_e \cos L \\ \bar{v} &= v - m_1(R_o + h)\omega_e \cos L \\ \bar{w} &= w - n_1(R_o + h)\omega_e \cos L \end{aligned}\right\} \tag{A13}$$

The resultant angle of attack of the spacecraft was computed from the earth-relative velocity components in equation (A13) as follows:

$$\eta = \tan^{-1}\frac{\sqrt{\bar{v}^2 + \bar{w}^2}}{\bar{u}} \tag{A14}$$

where the component angles of attack and yaw were defined by:

$$\left.\begin{aligned} \alpha &= \tan^{-1}\frac{\bar{w}}{\bar{u}} \\ \beta &= \tan^{-1}\frac{\bar{v}}{\sqrt{\bar{u}^2 + \bar{w}^2}} \end{aligned}\right\} \tag{A15}$$

In order to compare the results from integration of the flight measurements with preflight wind-tunnel test results, the aerodynamic forces during coasting flight in the atmosphere were computed simultaneously from the following equations:

$$\left.\begin{aligned} C_X &= \frac{Wa_{L,D}}{\bar{q}S} \\ C_R &= \sqrt{C_N^2 + C_Y^2} = \frac{W}{\bar{q}S}\sqrt{a_N^2 + a_T^2} \end{aligned}\right\} \tag{A16}$$

where the dynamic pressure $\bar{q}$ was determined by using the earth-relative velocity in equation (A12), and the free-stream density measured at the altitude computed from equations (A10):

$$\bar{q} = \frac{1}{2}\bar{\rho}V^2 \tag{A17}$$

The thrust of the fifth-stage spherical rocket motor was determined from the following equation, negligible aerodynamic forces at the higher thrusting altitudes being assumed:

$$T = Wa_{L,T} \tag{A18}$$

The resultant moment coefficient during coasting flight in the atmosphere was found from the equation:

$$C_{m_t} = \frac{\sqrt{M_{Y_A}^2 + M_{Z_A}^2}}{\bar{q}Sd} = \frac{1}{\bar{q}Sd}\sqrt{\left[\dot{q}I_Y - pr\left(I_Y - I_X\right)\right]^2 + \left[\dot{r}I_Y + pq\left(I_Y - I_X\right)\right]^2} \tag{A19}$$

It should be noted that the coefficients computed from the rate-gyro and accelerometer measurements in equations (A16) and (A19) were the summation of the forces and moments including effects due to pitching and yawing angular velocities.

APPENDIX B

EQUATIONS AND COMPUTATIONAL PROCEDURES FOR SIMULATION OF RATE-GYRO AND ACCELEROMETER FLIGHT MEASUREMENTS

Six-degree-of-freedom equations of motion over a spherical rotating earth were programed on an analog computer using nonlinear aerodynamic characteristics of the spacecraft from preflight wind-tunnel tests of reference 3. Equations (A3) were used to compute the body-axis inertial velocities during coasting flight in the atmosphere by substitution of the spacecraft aerodynamic forces for the accelerometer measurements as follows:

$$\left.\begin{aligned} u &= u_o + \int \left(F_{X_A} - g_o \sin\theta + vr - wq\right)dt \\ v &= v_o + \int \left(F_{Y_A} + g_o \cos\theta \sin\phi + wp - ur\right)dt \\ w &= w_o + \int \left(F_{Z_A} + g_o \cos\theta \cos\phi + uq - vp\right)dt \end{aligned}\right\} \qquad \text{(B1)}$$

where the aerodynamic forces were computed from

$$\left.\begin{aligned} F_{X_A} &= C_X \bar{q} S \\ F_{Y_A} &= C_Y \bar{q} S = \left(-C_R \sin\tau + C_{N_q} \frac{rd}{2\bar{V}}\right)\bar{q}S \\ F_{Z_A} &= -C_N \bar{q} S = \left(-C_R \cos\tau - C_{N_q} \frac{qd}{2\bar{V}}\right)\bar{q}S \end{aligned}\right\} \qquad \text{(B2)}$$

The aerodynamic phase angle τ was defined by the equations:

$$\tau = \sin^{-1} \frac{\bar{v}}{\sqrt{\bar{v}^2 + \bar{w}^2}} = \cos^{-1} \frac{\bar{w}}{\sqrt{\bar{v}^2 + \bar{w}^2}} \qquad \text{(B3)}$$

The angular velocities p, q, and r required for solution of equations (B1), and comparison with rate-gyro measurements, were determined from the following equations written for a symmetrical spacecraft with no products of inertia and $I_Y = I_Z$:

$$\left.\begin{aligned} p &= p_o \\ q &= q_o + \int \left[\frac{M_{Y_A}}{I_Y} + pr\left(\frac{I_Y - I_X}{I_Y}\right)\right] dt \\ r &= r_o + \int \left[\frac{M_{Z_A}}{I_Y} - pq\left(\frac{I_Y - I_X}{I_Y}\right)\right] dt \end{aligned}\right\} \tag{B4}$$

where the total aerodynamic moments of the spacecraft were defined as

$$\left.\begin{aligned} M_{X_A} &= 0 \\ M_{Y_A} &= \left[\left(C_R \cos \tau\right)\left(\frac{x_{cg} - x_{cp}}{d}\right) + C_{m_q}\left(\frac{qd}{2\bar{V}}\right)\right]\bar{q}Sd \\ M_{Z_A} &= \left[\left(-C_R \sin \tau\right)\left(\frac{x_{cg} - x_{cp}}{d}\right) + C_{m_q}\left(\frac{rd}{2\bar{V}}\right)\right]\bar{q}Sd \end{aligned}\right\} \tag{B5}$$

The force coefficients C_X and C_R in equations (B2) and (B5), and the spacecraft center of pressure x_{cp} in equations (B5) were programed as a function of Mach number and angle of attack from the wind-tunnel tests of reference 3. The results obtained on both the model $\left(N_3B_3\right)$ with the nose cap on, and the model $\left(N_4B_4\right)$ with nose cap off were used. The damping force and moment coefficients were estimated from Newtonian impact theory and were assumed to be equal in magnitude $\left(C_{N_q} = C_{Y_r} \text{ and } C_{m_q} = C_{n_r}\right)$ for the symmetrical spacecraft. The spacecraft center-of-gravity position in equation (B5) was obtained from preflight measurements with and without the nose cap installed.

The spacecraft linear accelerations were computed for comparison with accelerometer flight measurements from equations (B2) as follows:

$$\left.\begin{aligned} a_L &= \frac{F_{X_A}}{W} = \frac{C_X \bar{q} S}{W} \\ a_T &= \frac{F_{Y_A}}{W} = \frac{C_Y \bar{q} S}{W} \\ a_N &= -\frac{F_{Z_A}}{W} = \frac{C_N \bar{q} S}{W} \end{aligned}\right\} \tag{B6}$$

The remaining equations defining the trajectory and motions of the spacecraft were the same as those used for integration of the rate-gyro and accelerometer measurements as presented in appendix A.

REFERENCES

1. Rashis, Bernard; and O'Hare, Brian J.: Free-Flight Investigation of Reentry Heat Transfer and Ablation at Velocities up to 22,500 Feet Per Second. NASA TM X-970, 1964.

2. Lovelace, Uriel M.; Hoffman, Sherwood; and Mayhue, Robert J.: Analysis of the Trajectory and Large-Amplitude Motions of a Scout Vehicle During Fourth-Stage Reentry Flight. NASA TN D-2309, 1964.

3. Johnston, Patrick J.: Longitudinal Aerodynamic Characteristics of Several Fifth-Stage Scout Reentry Vehicles From Mach Number 0.60 to 24.4 Including Some Reynolds Number Effects on Stability at Hypersonic Speeds. NASA TN D-1638, 1963.

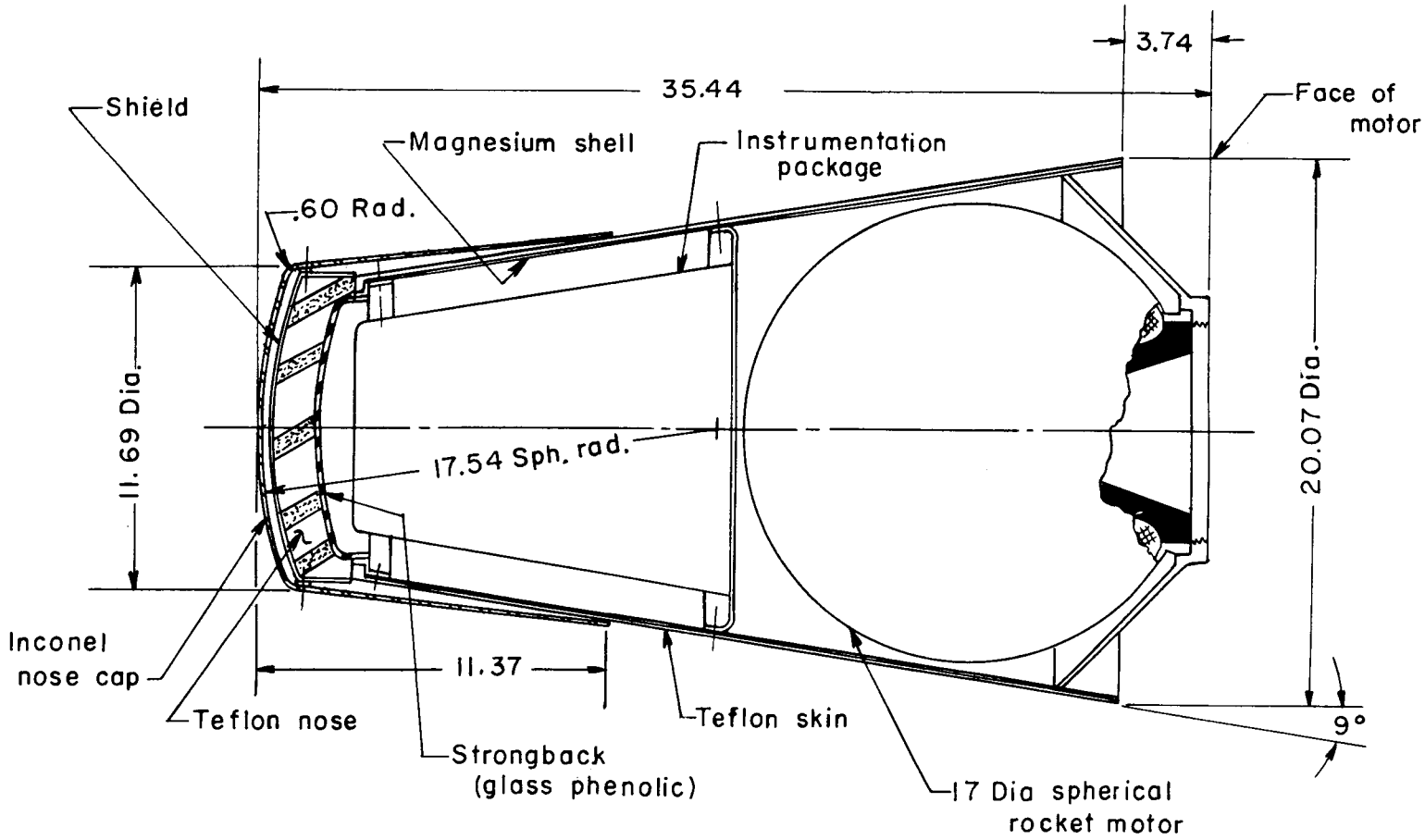

Figure 1.- Scout heat-transfer spacecraft. All dimensions are in inches unless otherwise noted.

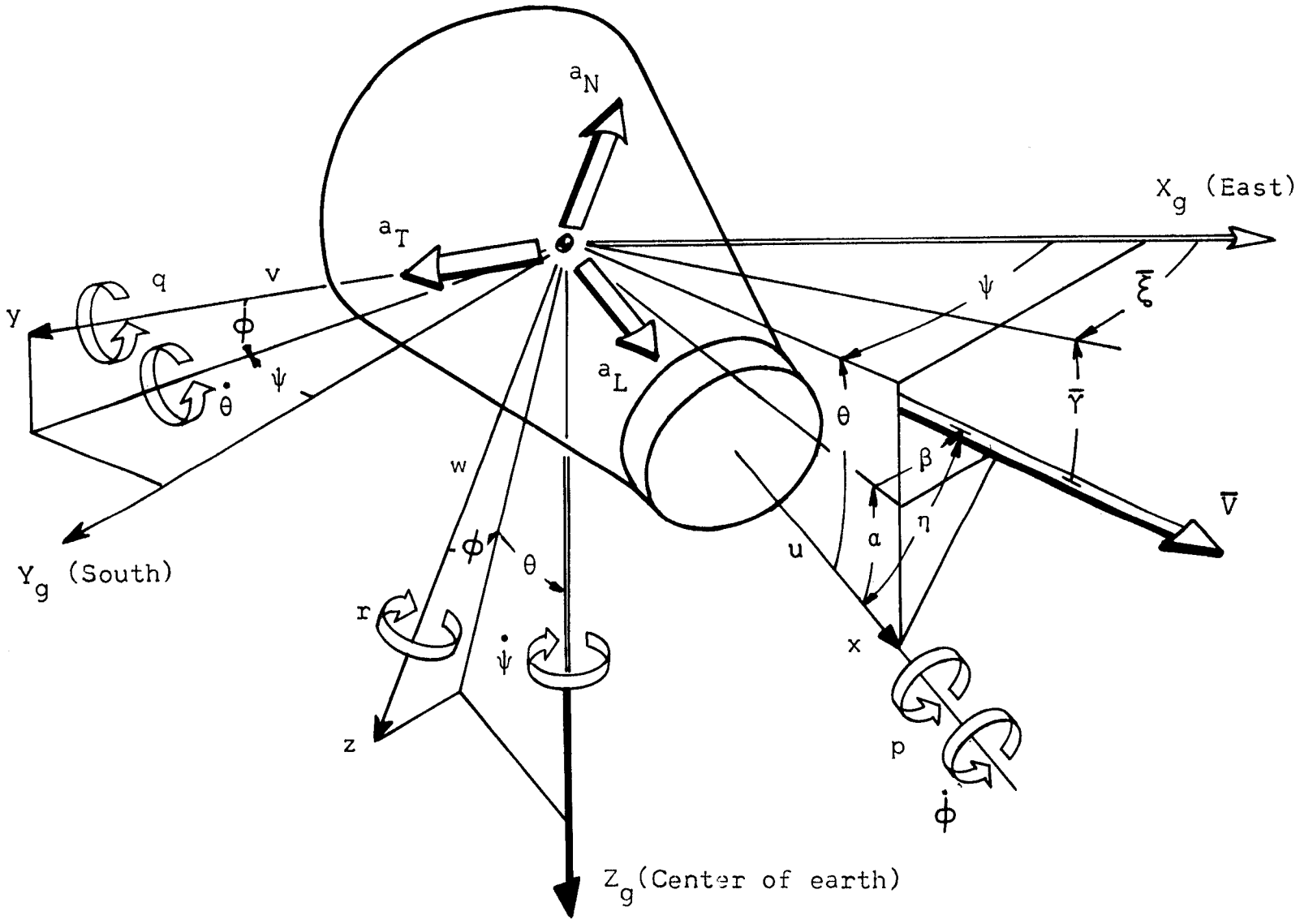

Figure 2.- Spacecraft coordinate systems and sign convention.

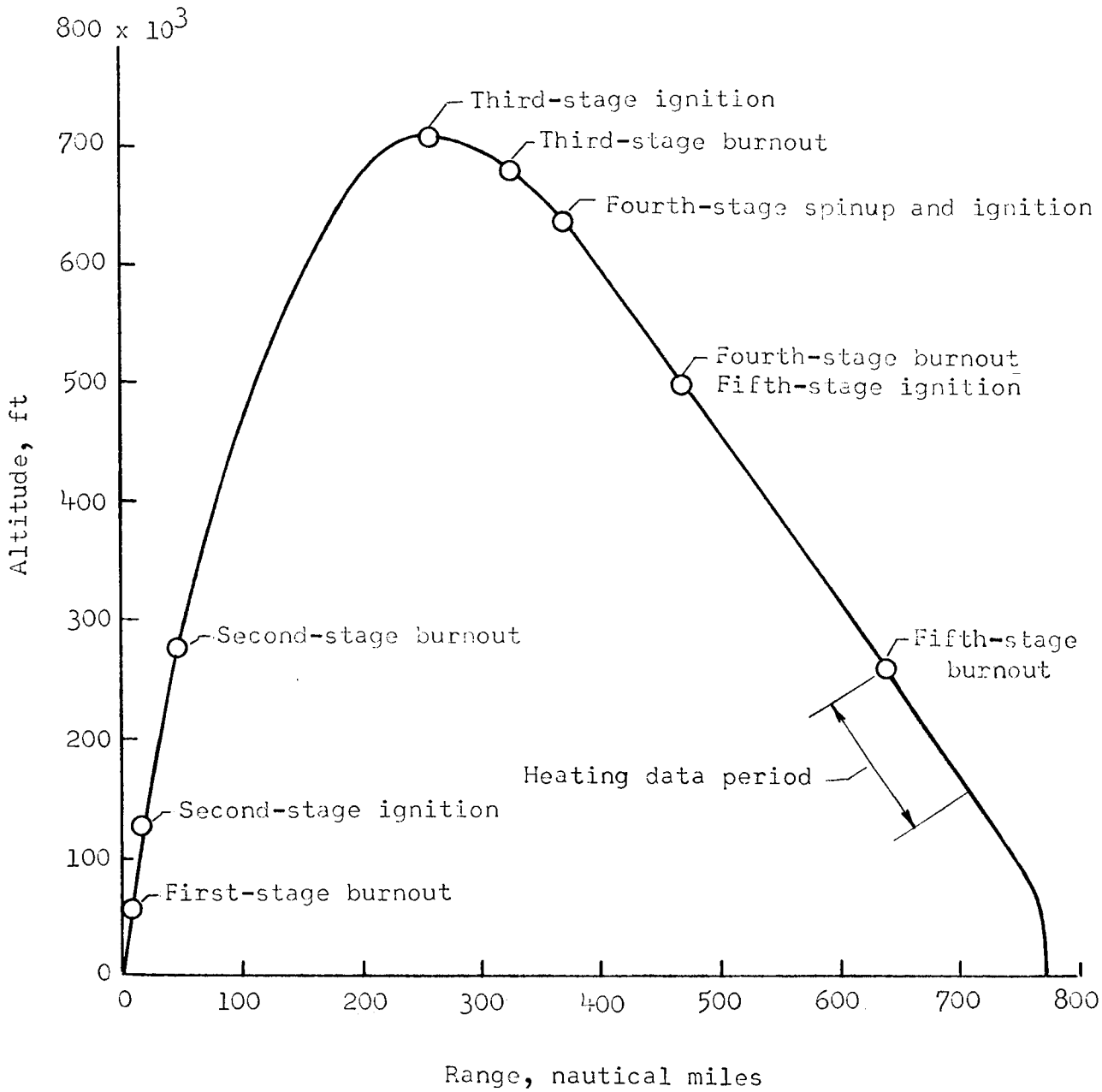

Figure 3.- Preflight nominal trajectory and flight events.

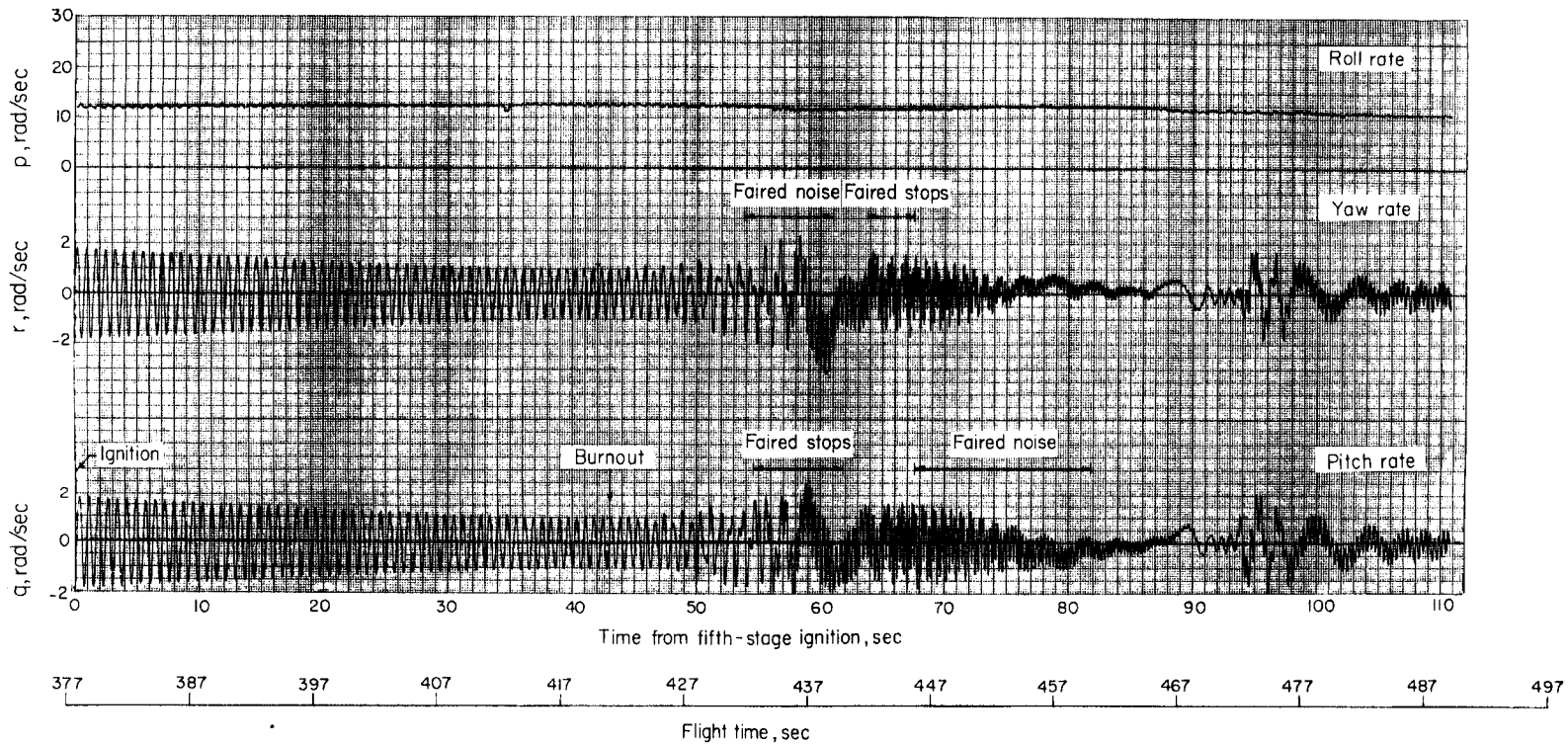

Figure 4.- Time histories of measured angular velocity in roll, yaw, and pitch.

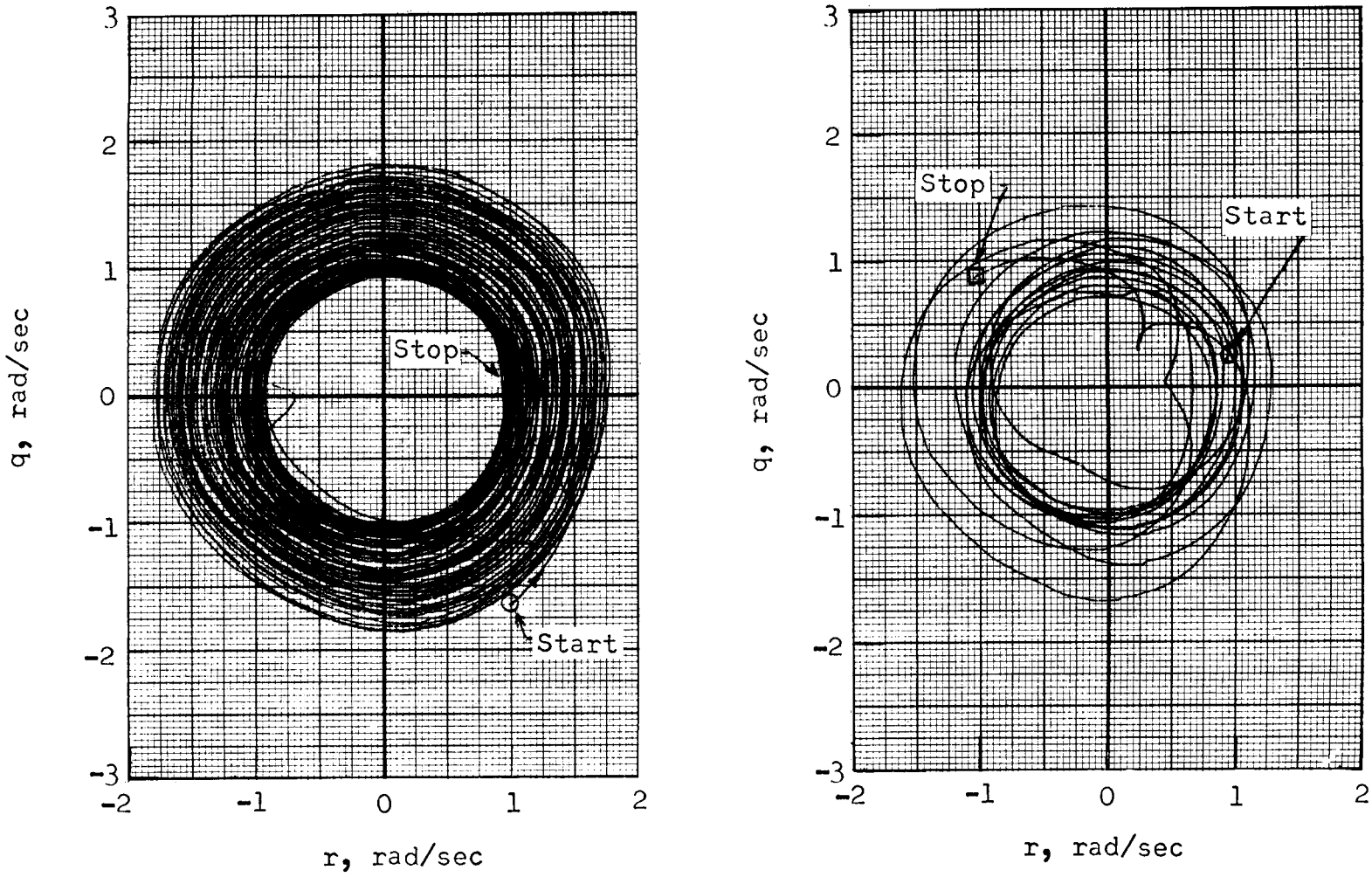

(a) t = 377.85 to 420.85 sec.

(b) t = 420.87 to 430.85 sec.

Figure 5.- Cross plots of measured angular velocities in pitch and yaw.

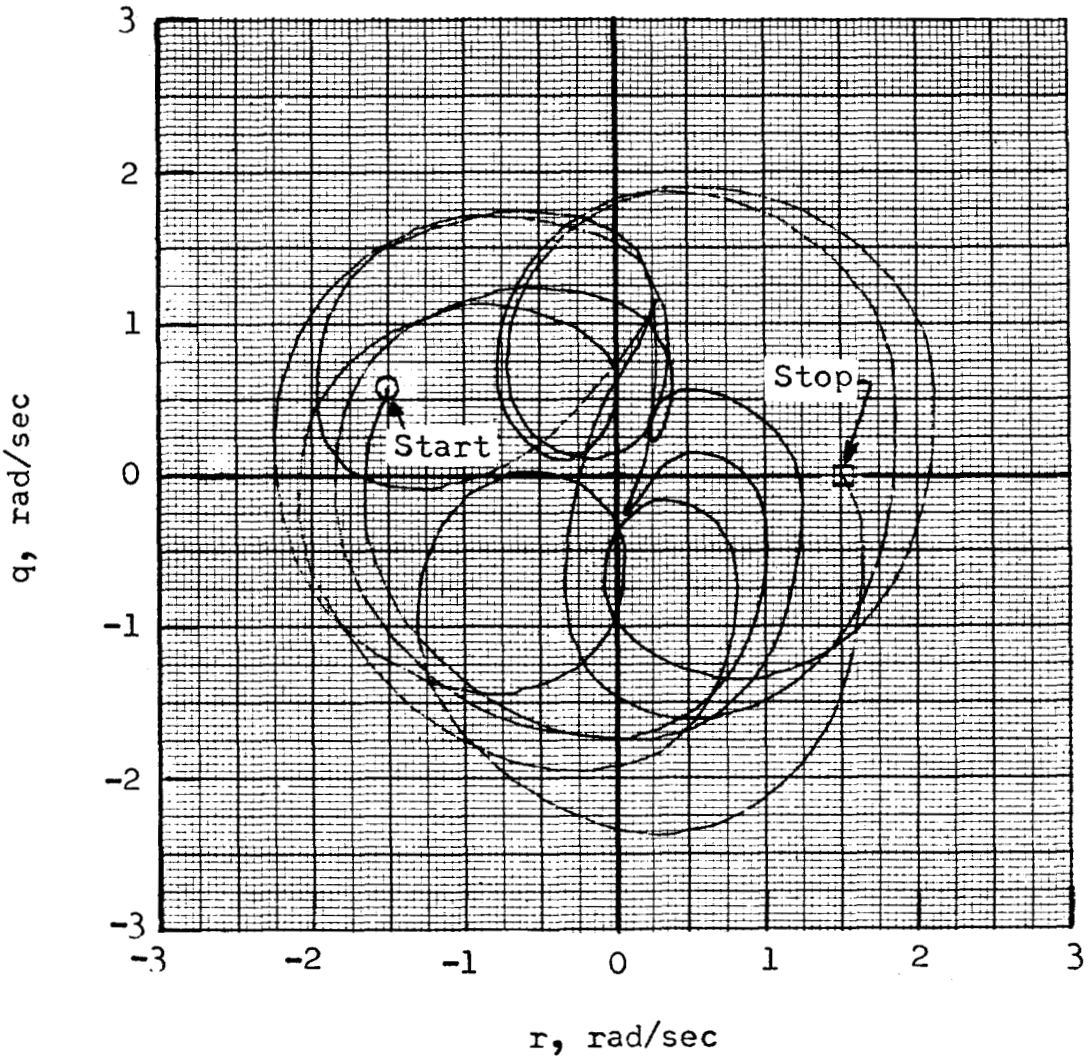

(c) t = 430.87 to 435.85 sec.

Figure 5.- Continued.

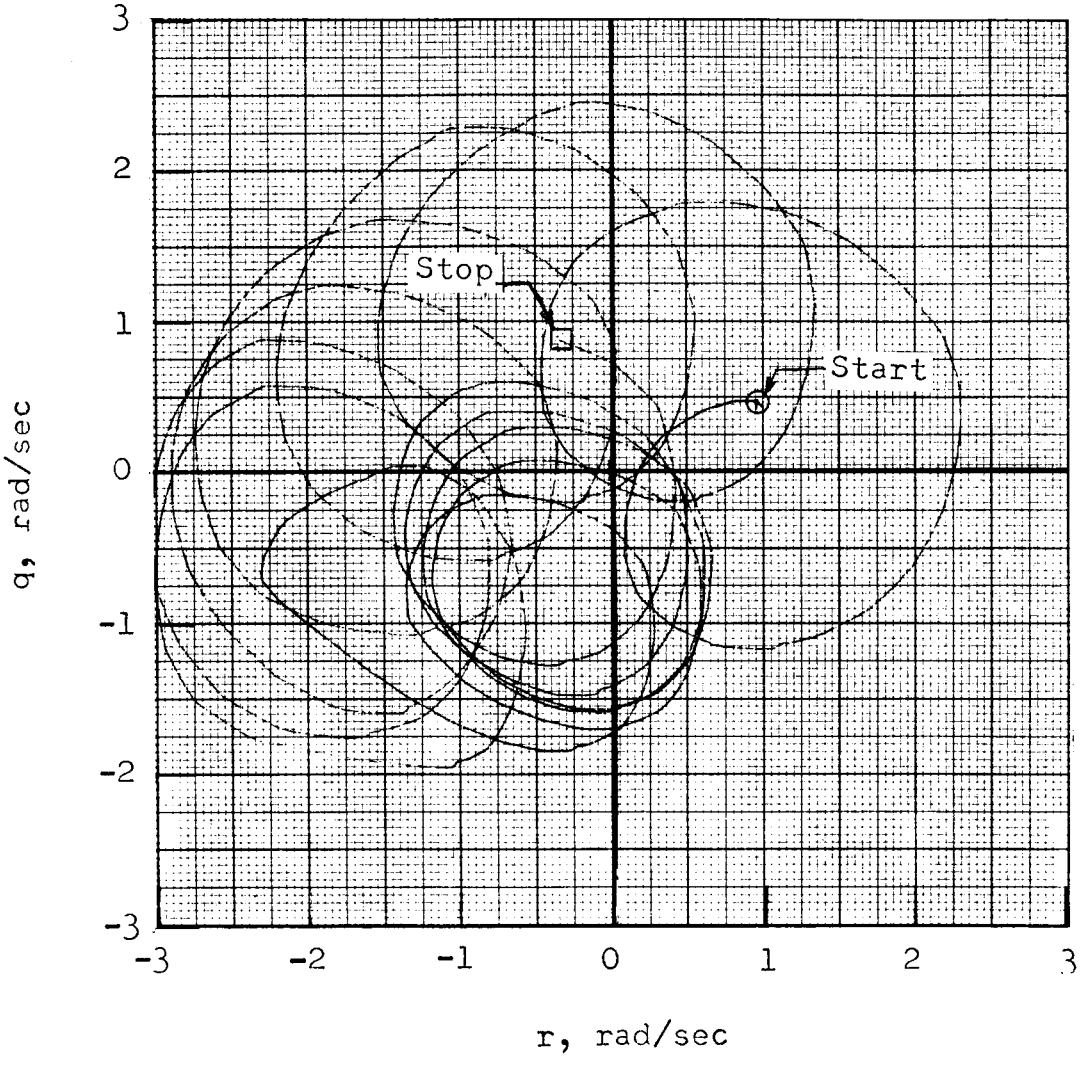

(d) t = 435.87 to 440.85 sec.

Figure 5.- Continued.

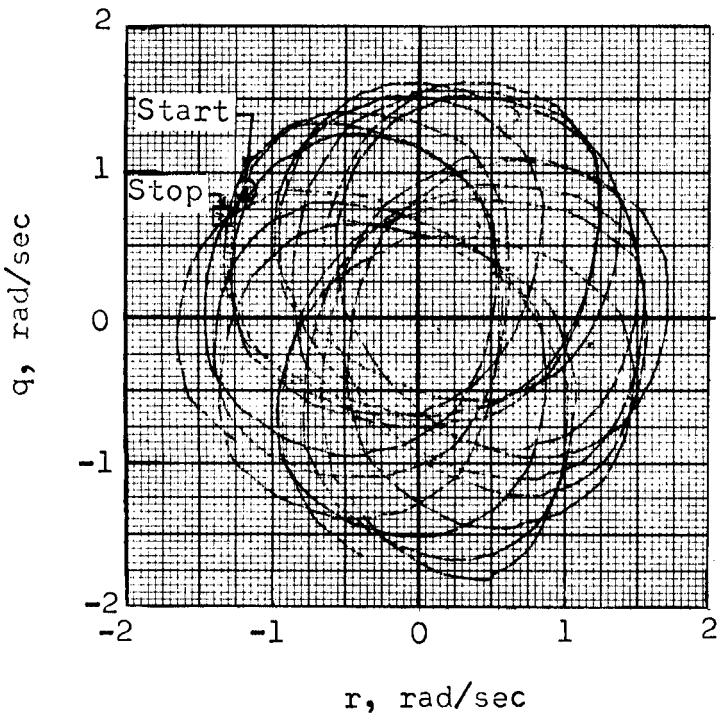

(e) t = 440.87 to 445.85 sec.

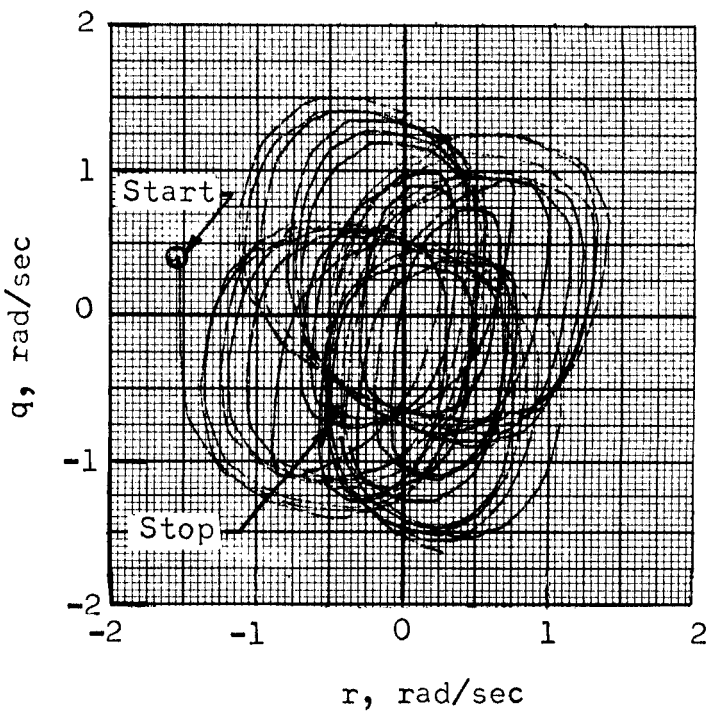

(f) t = 445.87 to 452.85 sec.

Figure 5.- Continued.

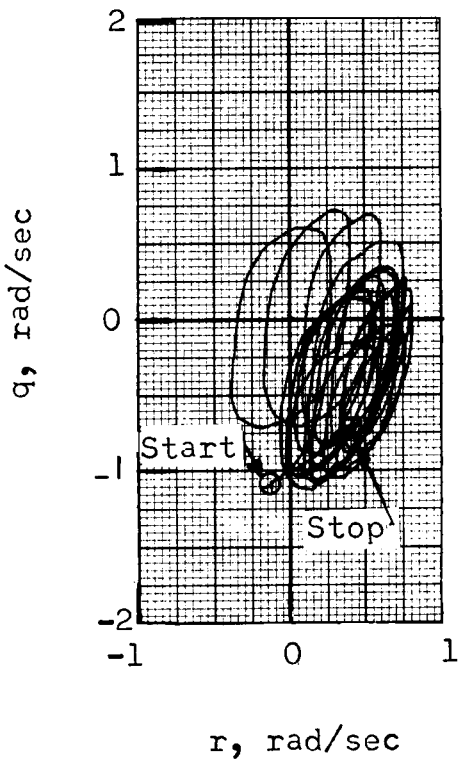

(g) t = 452.87 to 457.85 sec.

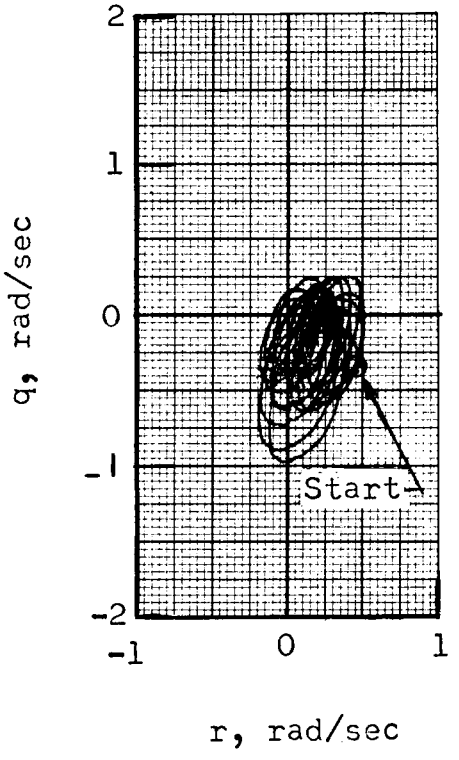

(h) t = 457.87 to 462.85 sec.

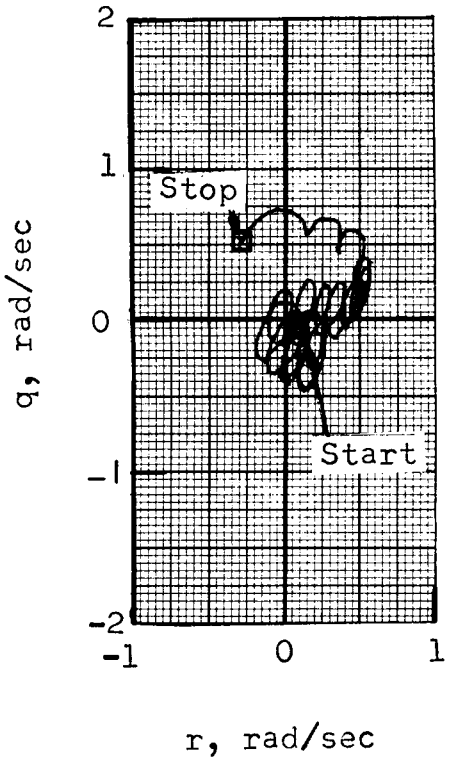

(i) t = 462.87 to 467.85 sec.

Figure 5.- Continued.

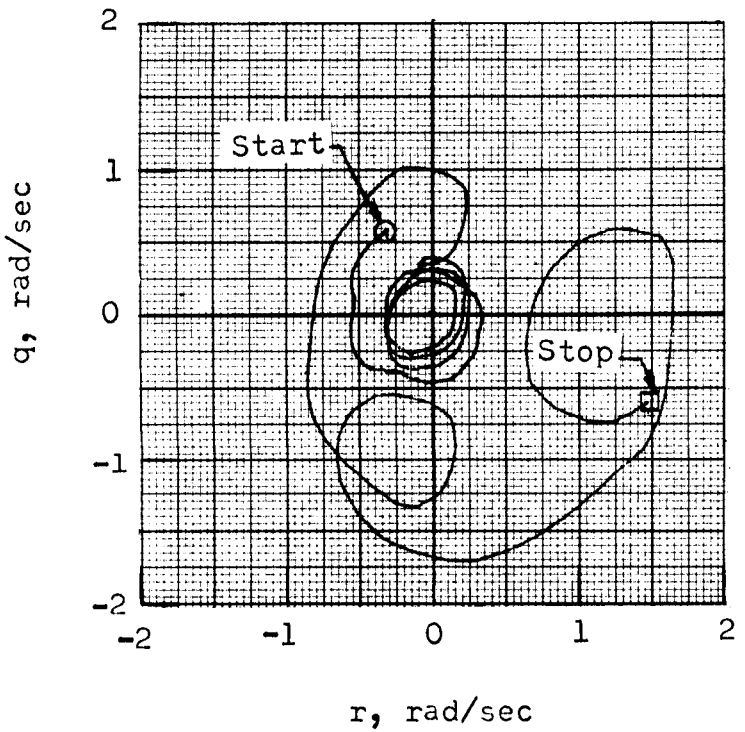

(j) t = 467.87 to 472.85 sec.

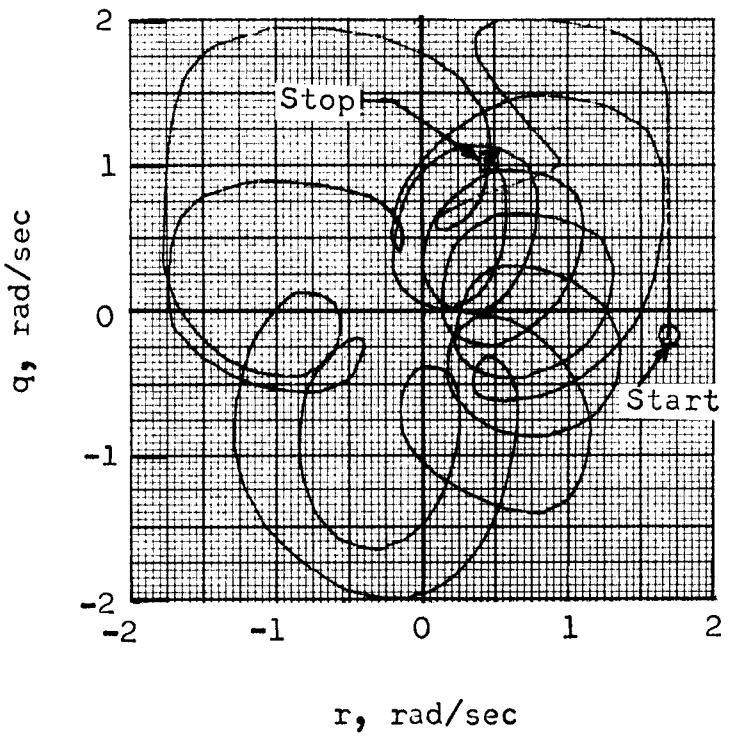

(k) t = 472.87 to 477.85 sec.

Figure 5.- Continued.

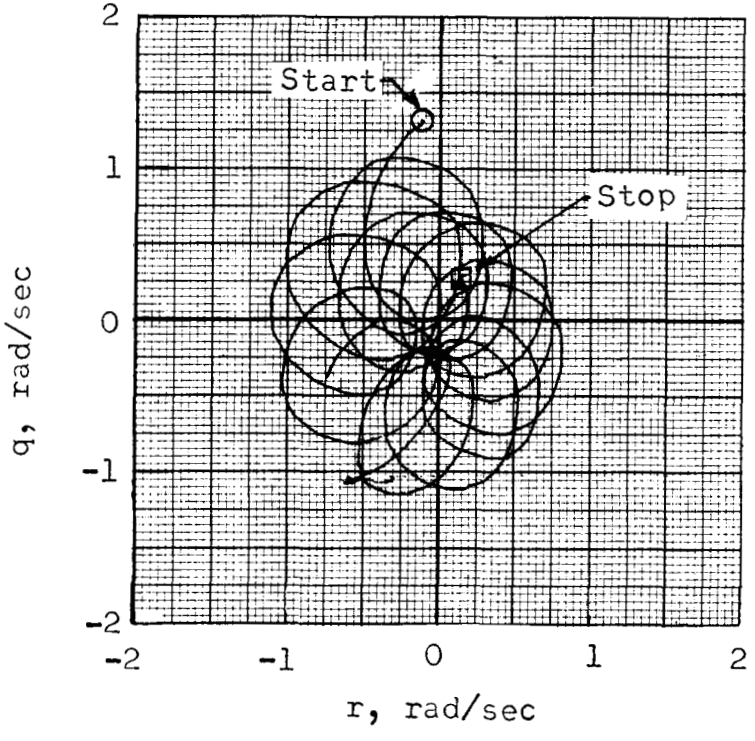

(l) t = 477.87 to 482.85 sec.

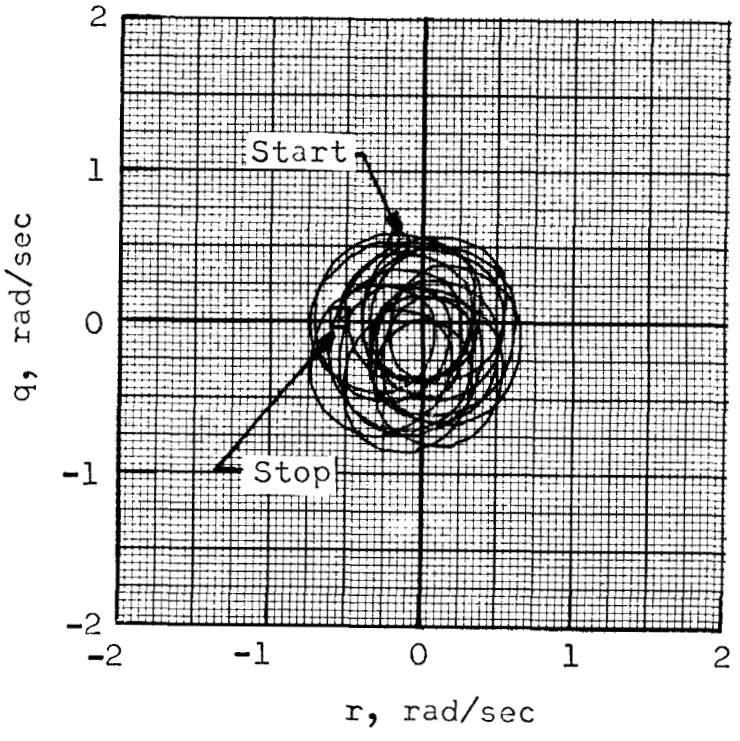

(m) t = 482.87 to 488.65 sec.

Figure 5.- Concluded.

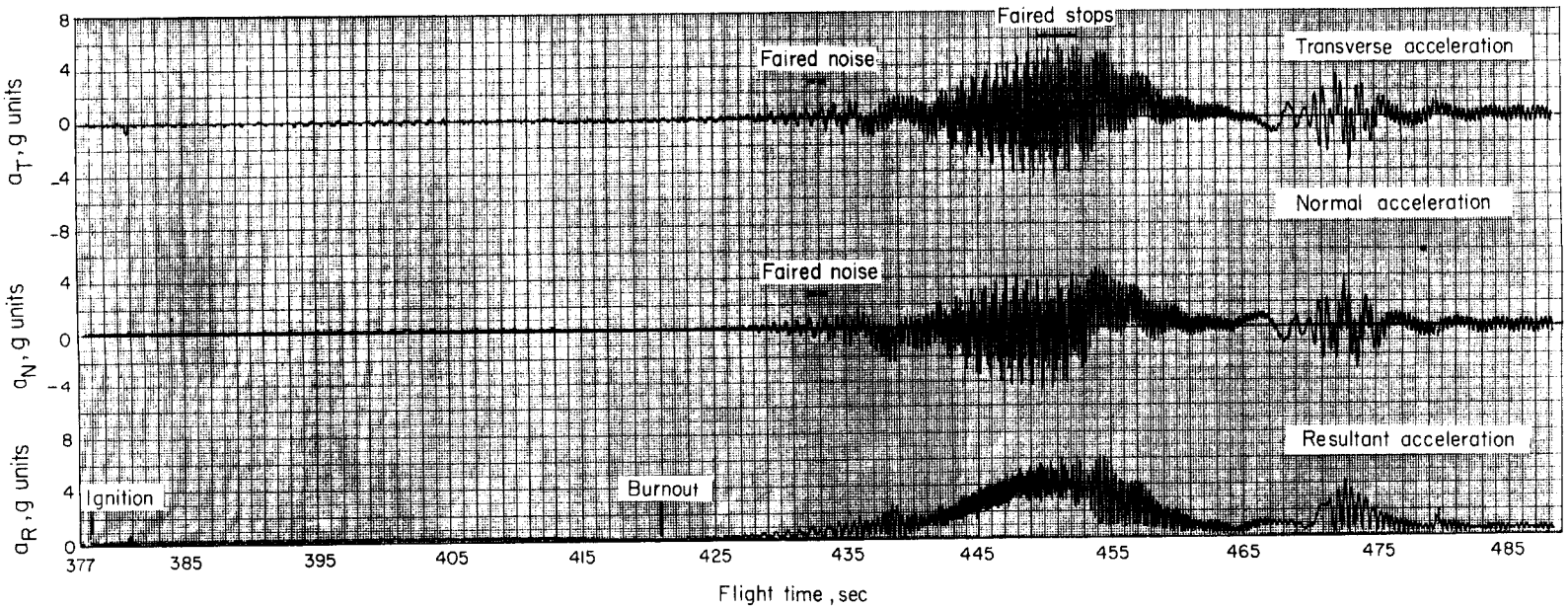

Figure 6.- Time histories of measured normal and transverse accelerations corrected for instrumentation displacement errors.

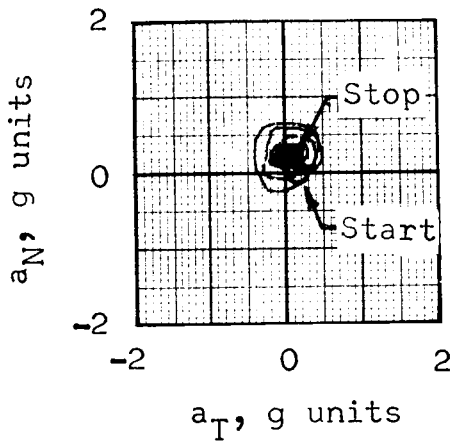

(a) t = 420.85 to 430.83 sec.

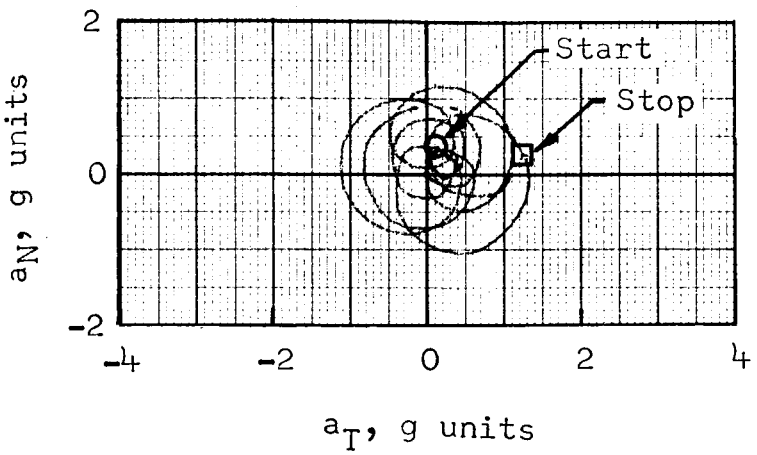

(b) t = 430.85 to 435.83 sec.

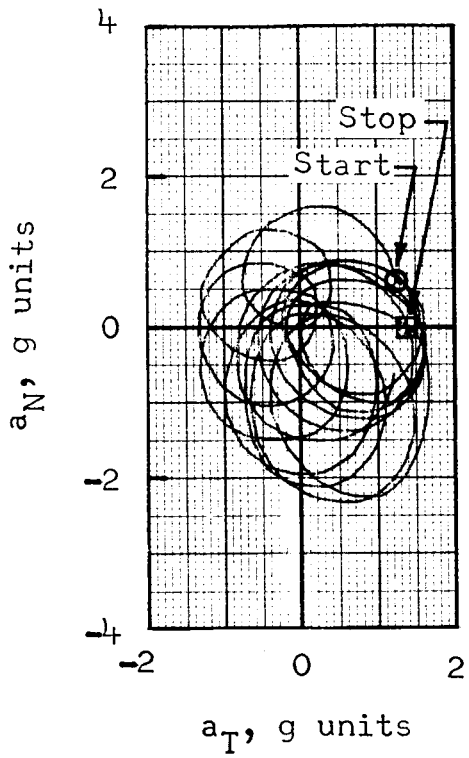

(c) t = 435.85 to 440.83 sec.

Figure 7.- Cross plots of measured normal and transverse acceleration corrected for instrumentation displacement error.

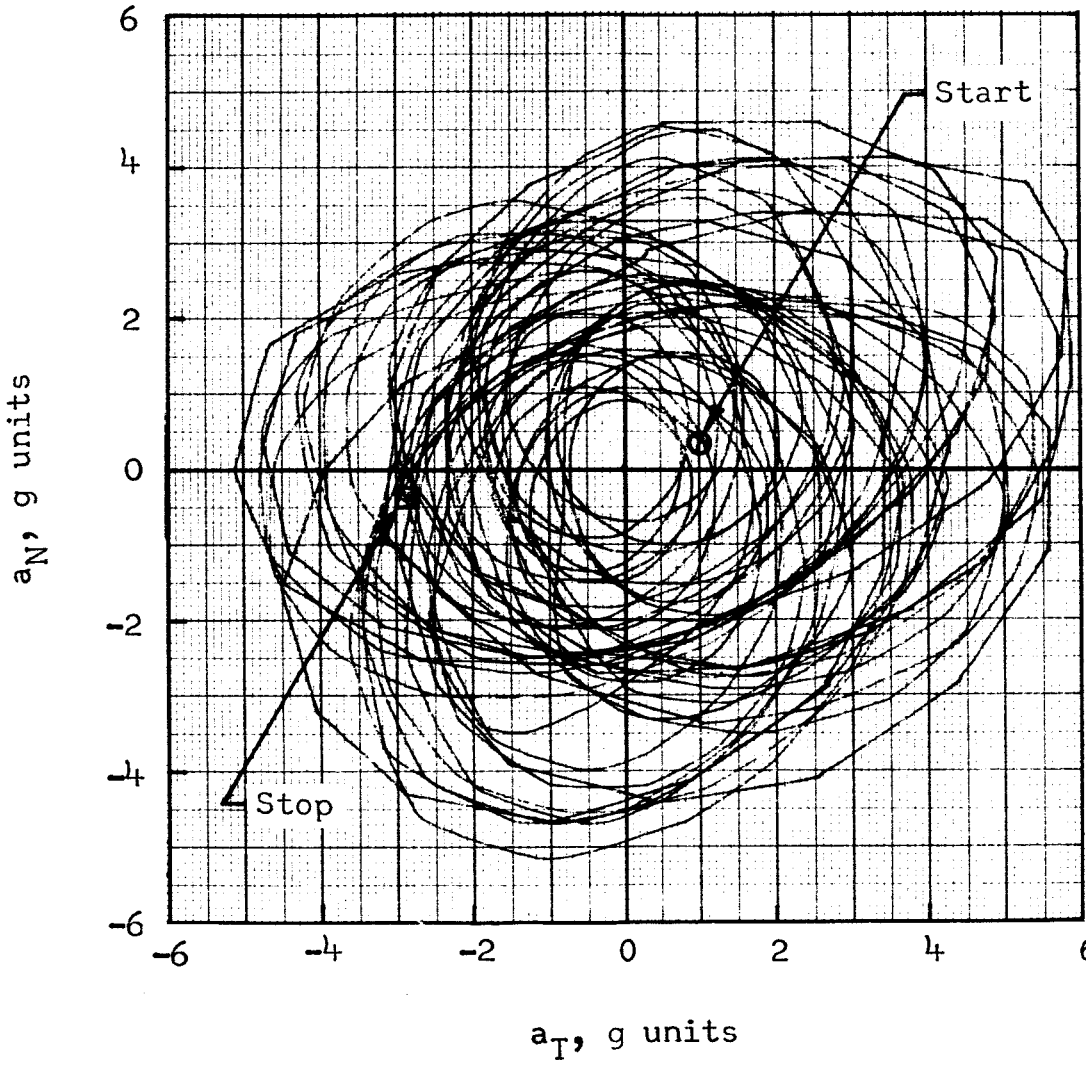

(d) t = 440.85 to 452.83 sec.

Figure 7.- Continued.

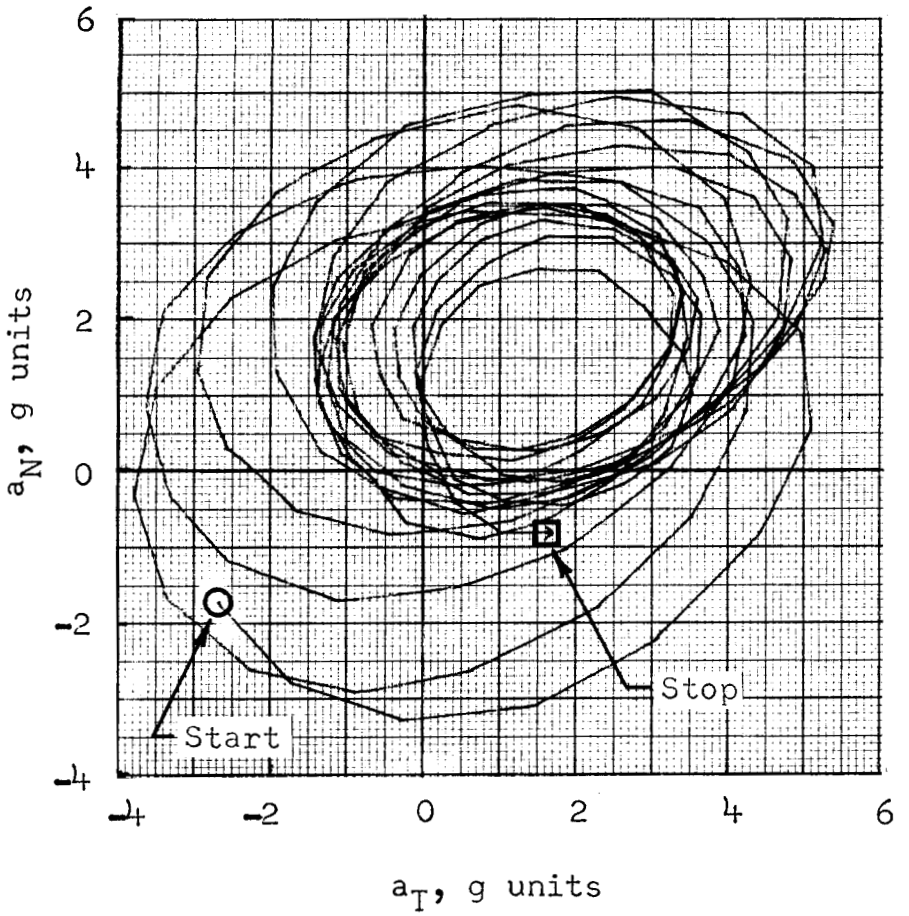

(e) t = 452.85 to 457.83 sec.

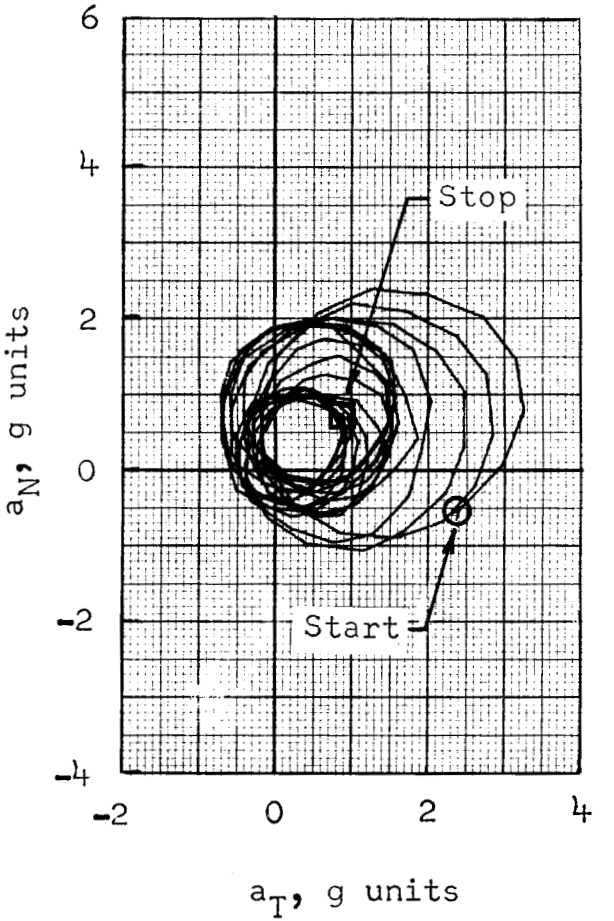

(f) t = 457.85 to 462.83 sec.

Figure 7.- Continued.

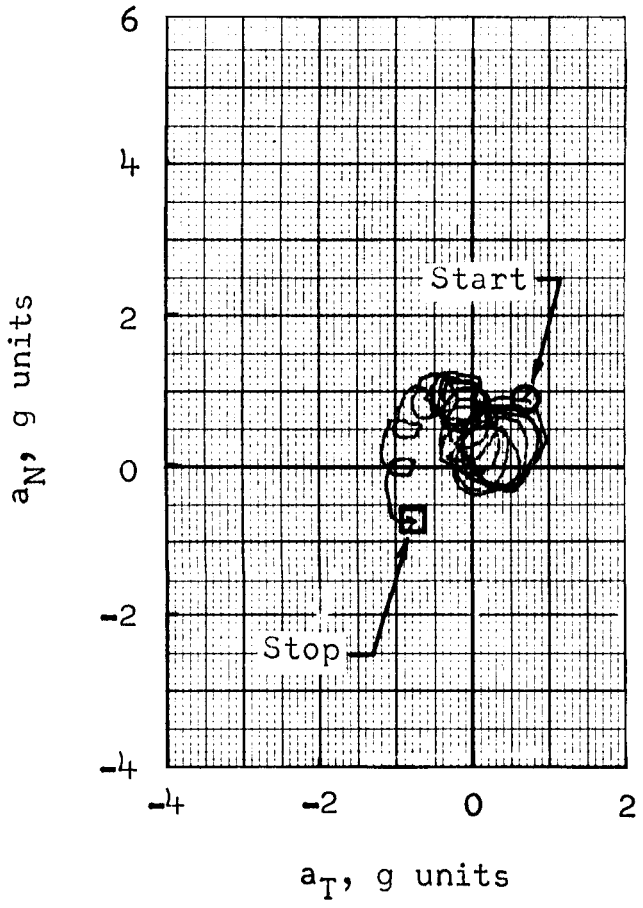

(g) t = 462.85 to 467.83 sec.

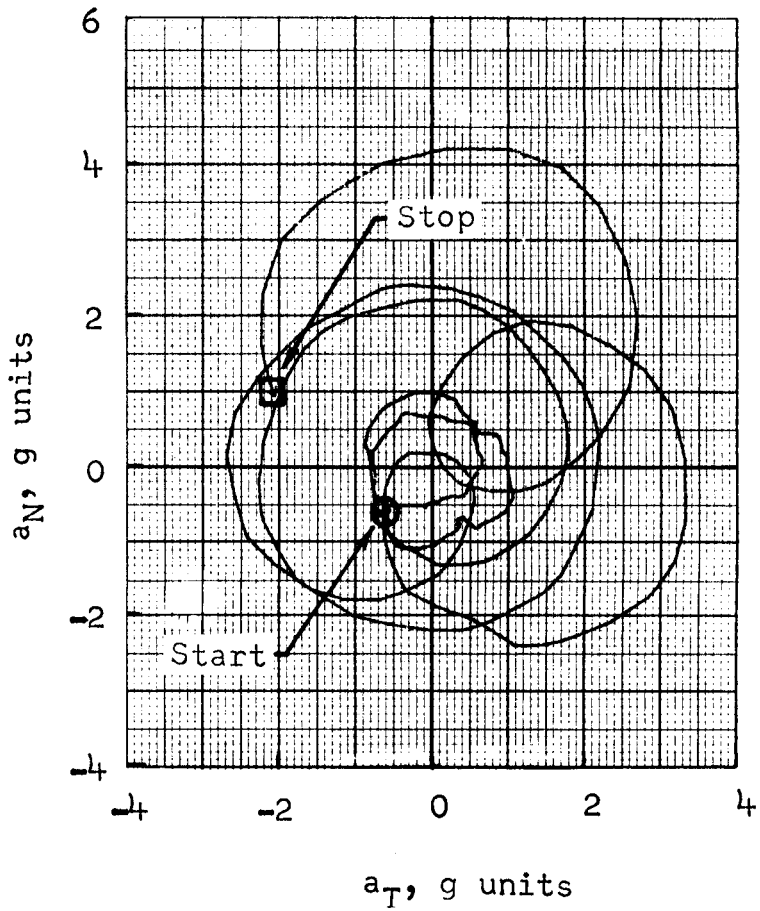

(h) t = 467.85 to 472.83 sec.

Figure 7.- Continued.

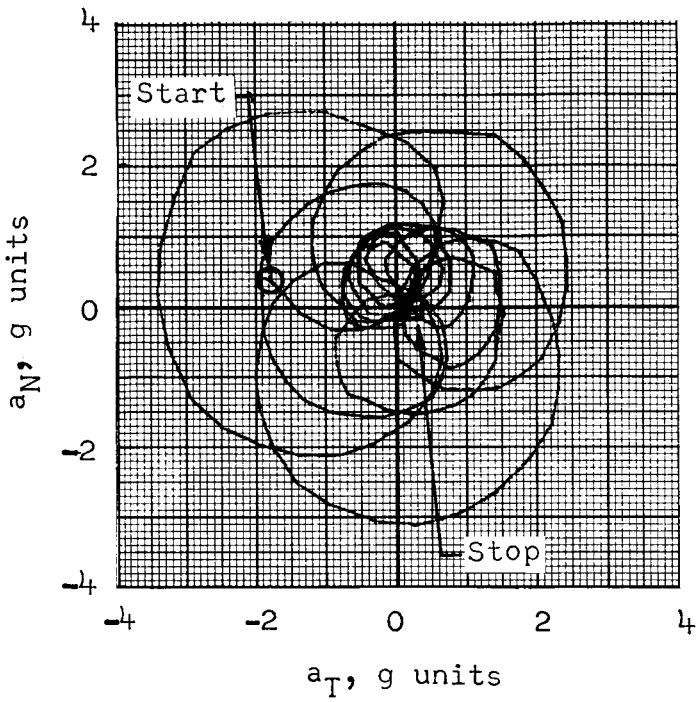

(i) t = 472.85 to 477.83 sec.

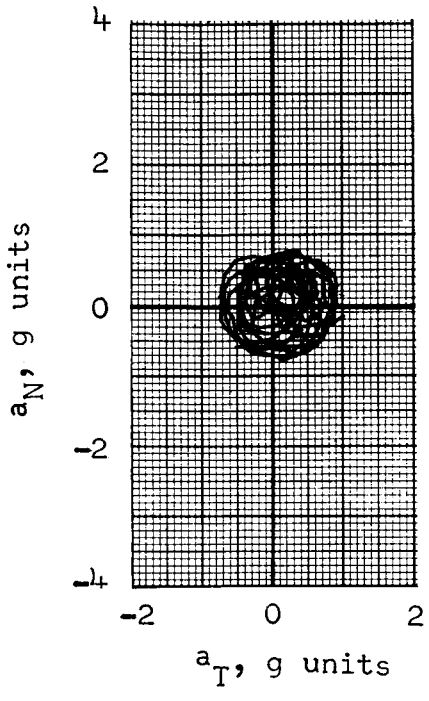

(j) t = 477.85 to 482.83 sec.

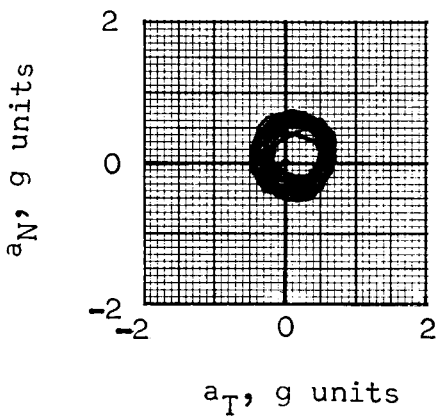

(k) t = 482.85 to 488.49 sec.

Figure 7.- Concluded.

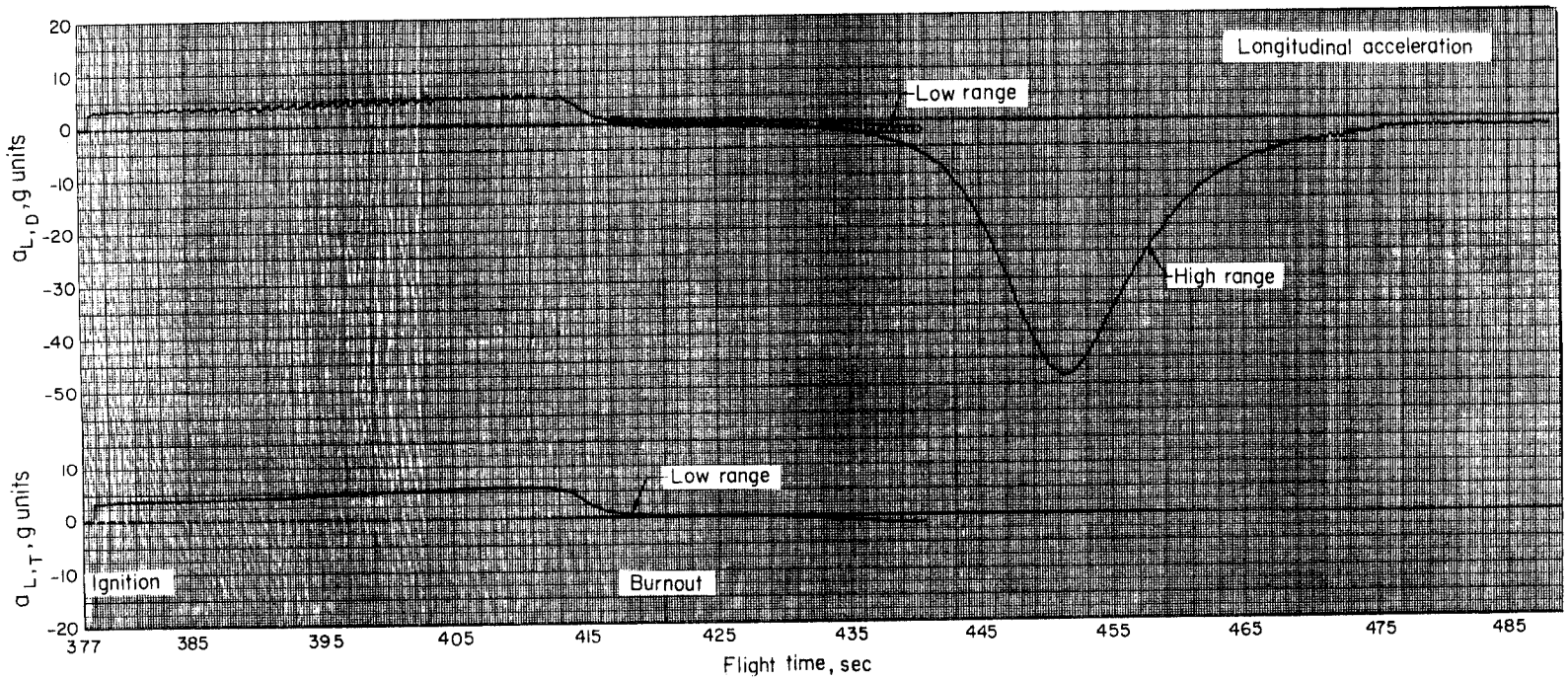

Figure 8.- Time history of measured longitudinal acceleration corrected for instrumentation displacement error.

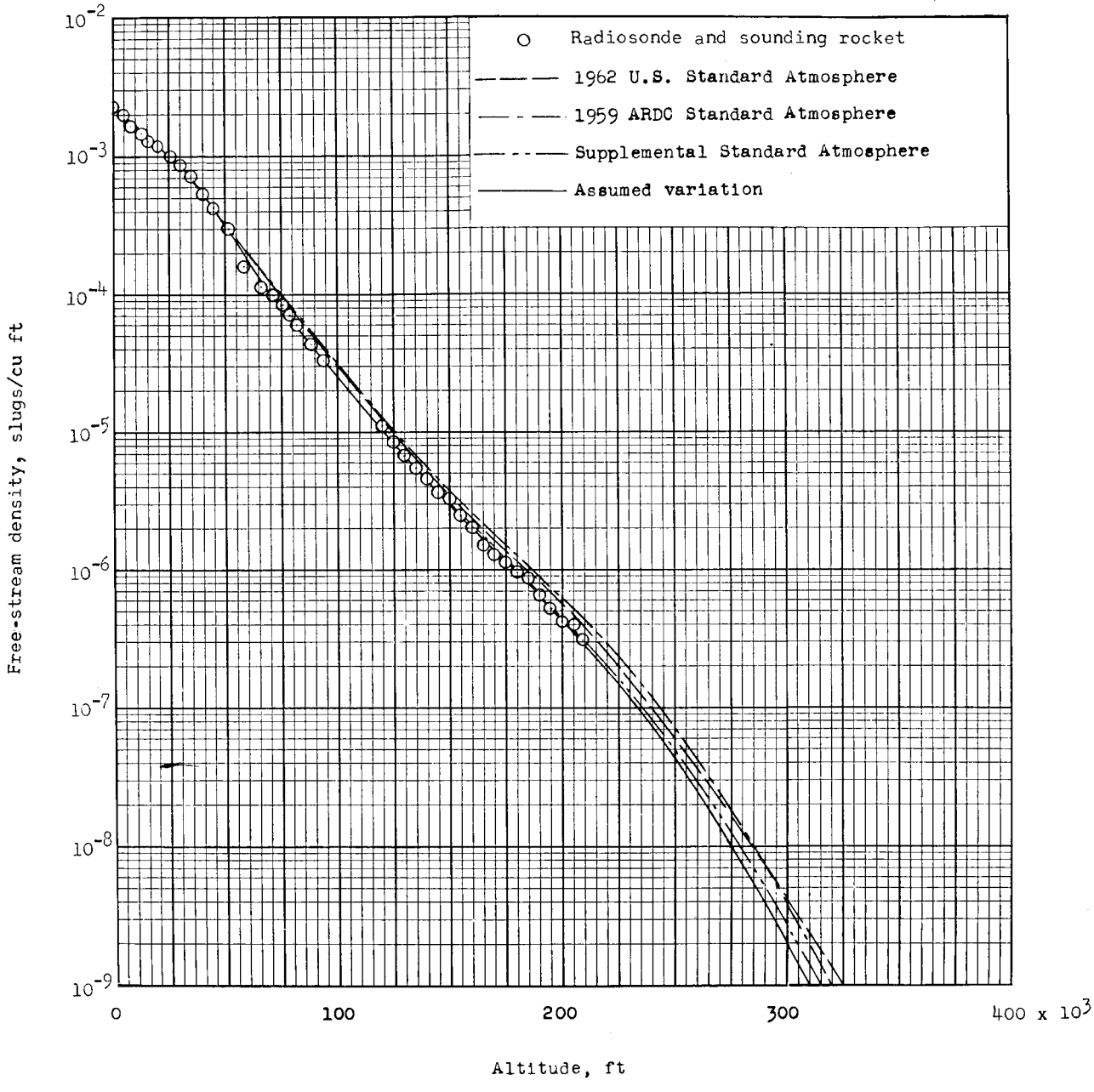

Figure 9.- Variation of free-stream density with altitude.

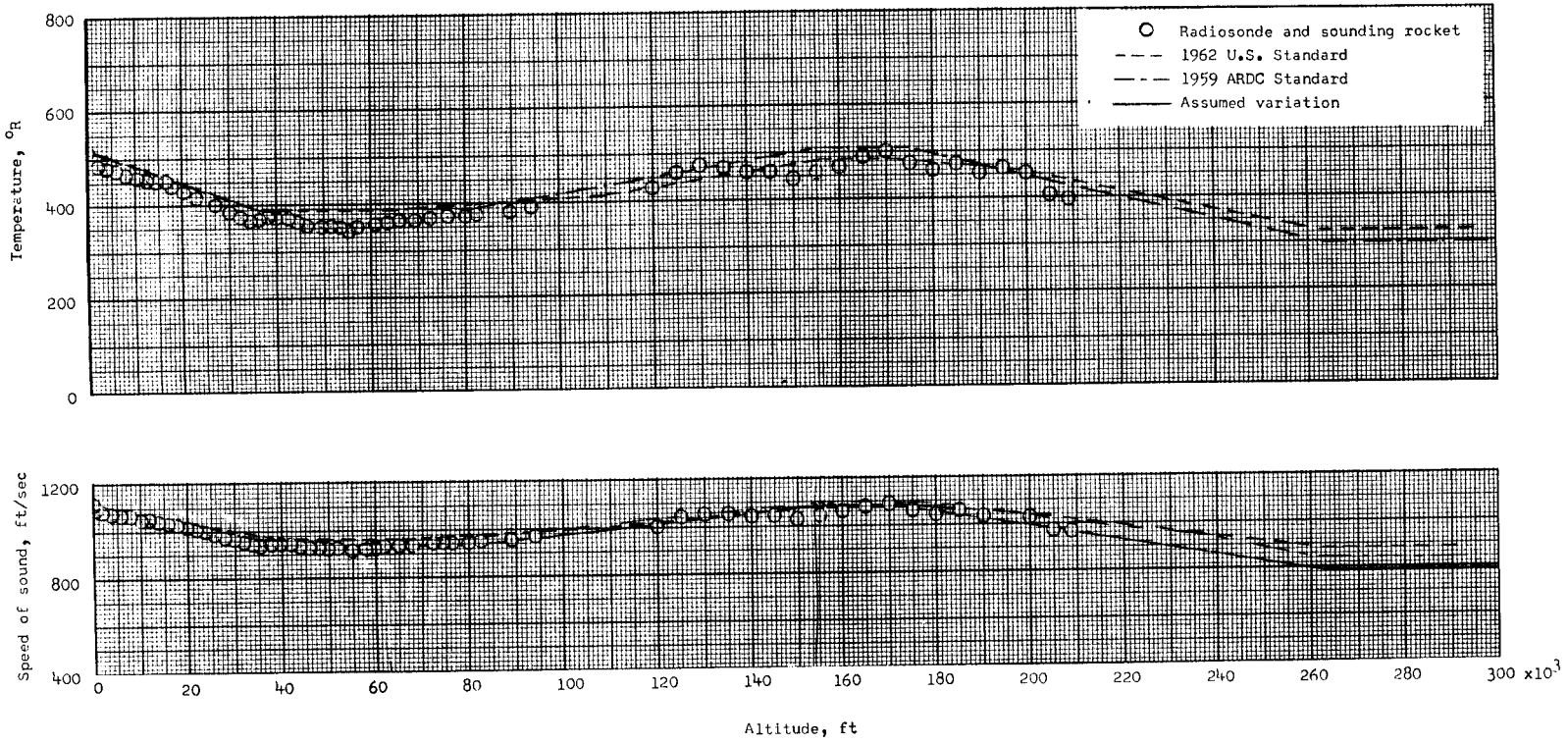

Figure 10.- Variation of measured free-stream temperature and speed of sound with altitude.

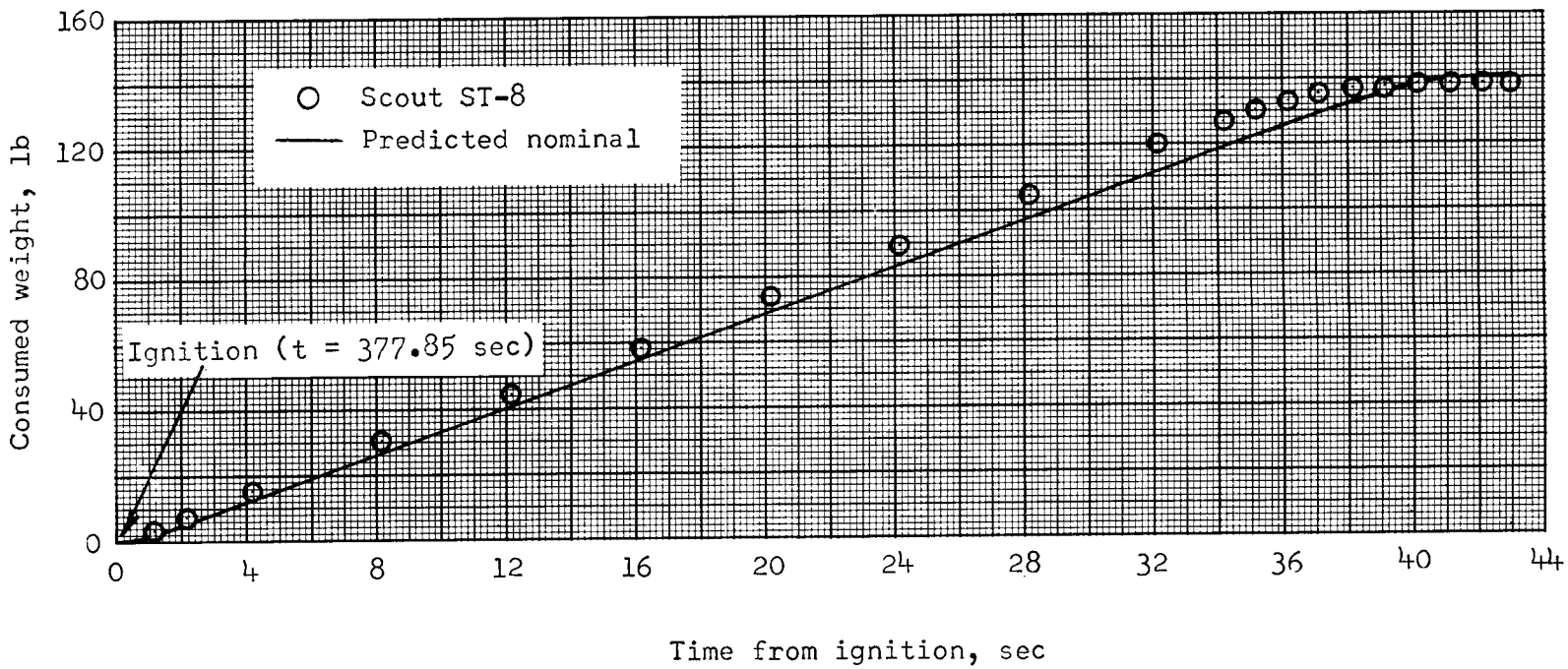

Figure 11.- Comparison between nominal and computed consumed weight during fifth-stage thrusting. (NOTS 100B) 17-inch spherical motor.

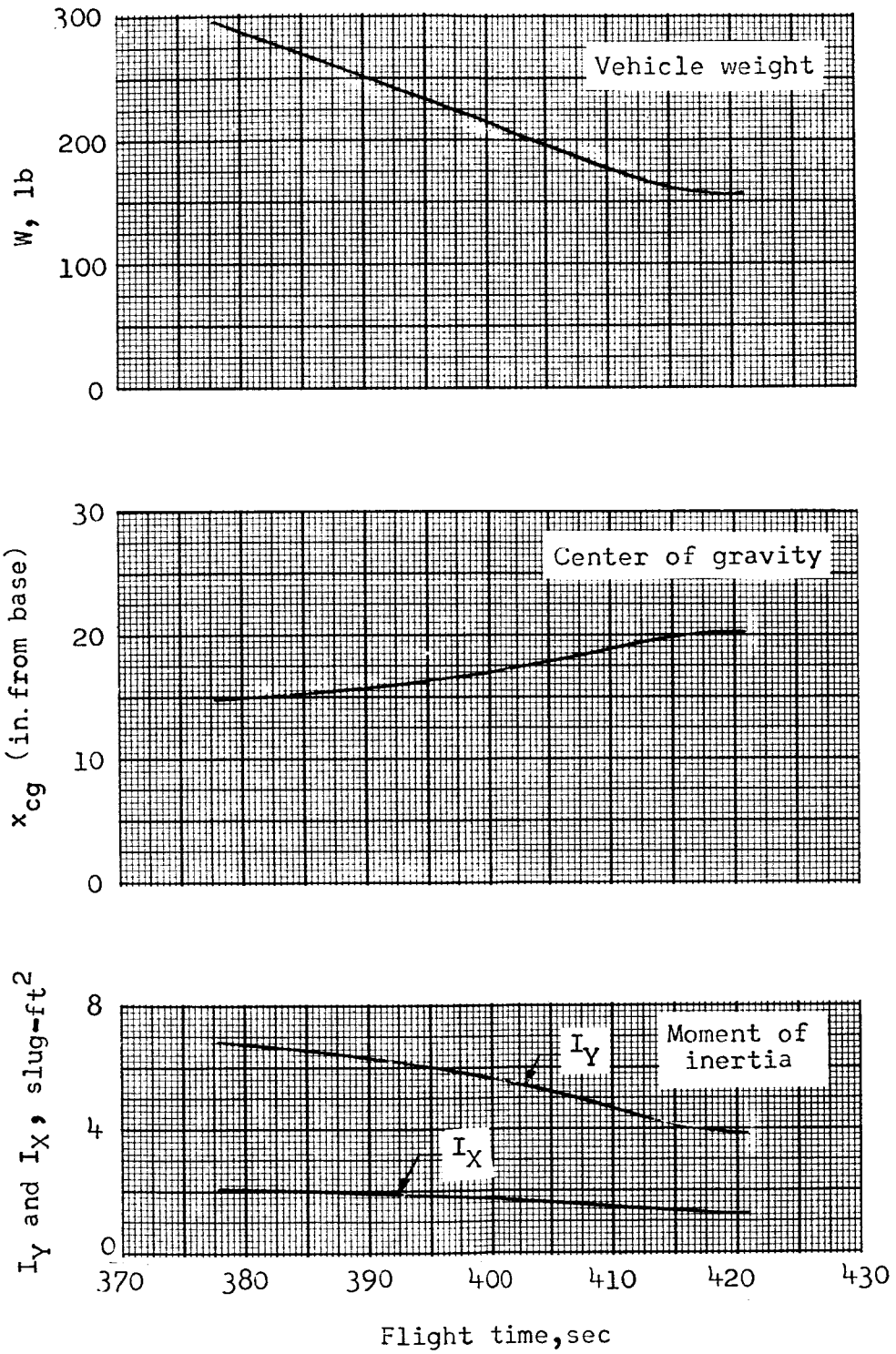

Figure 12.- Time histories of computed spacecraft weight, center of gravity, and moments of inertia during fifth-stage thrusting.

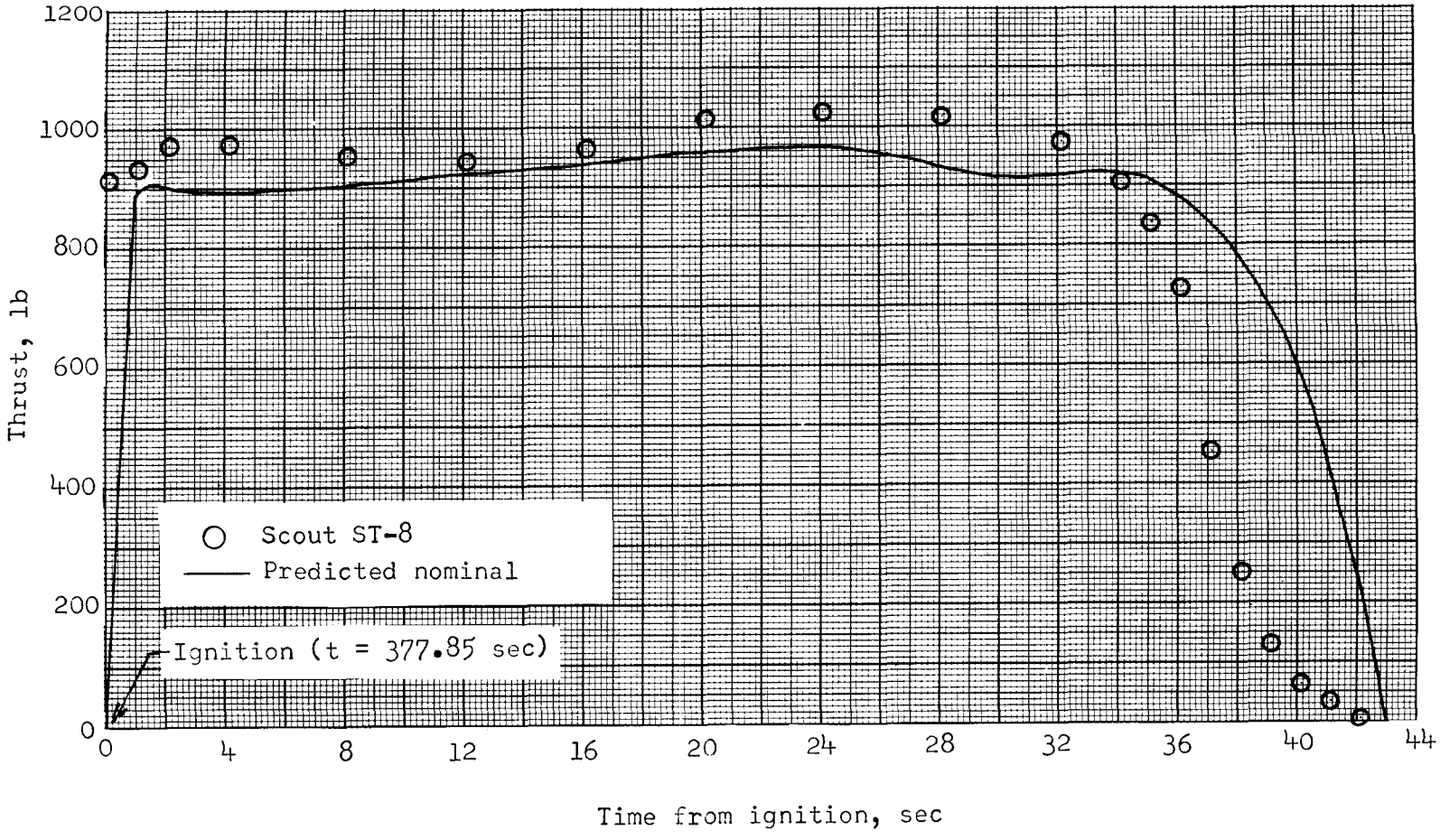

Figure 13.- Comparison between nominal and computed flight thrust time histories. (NOTS 100B) 17-inch spherical motor.

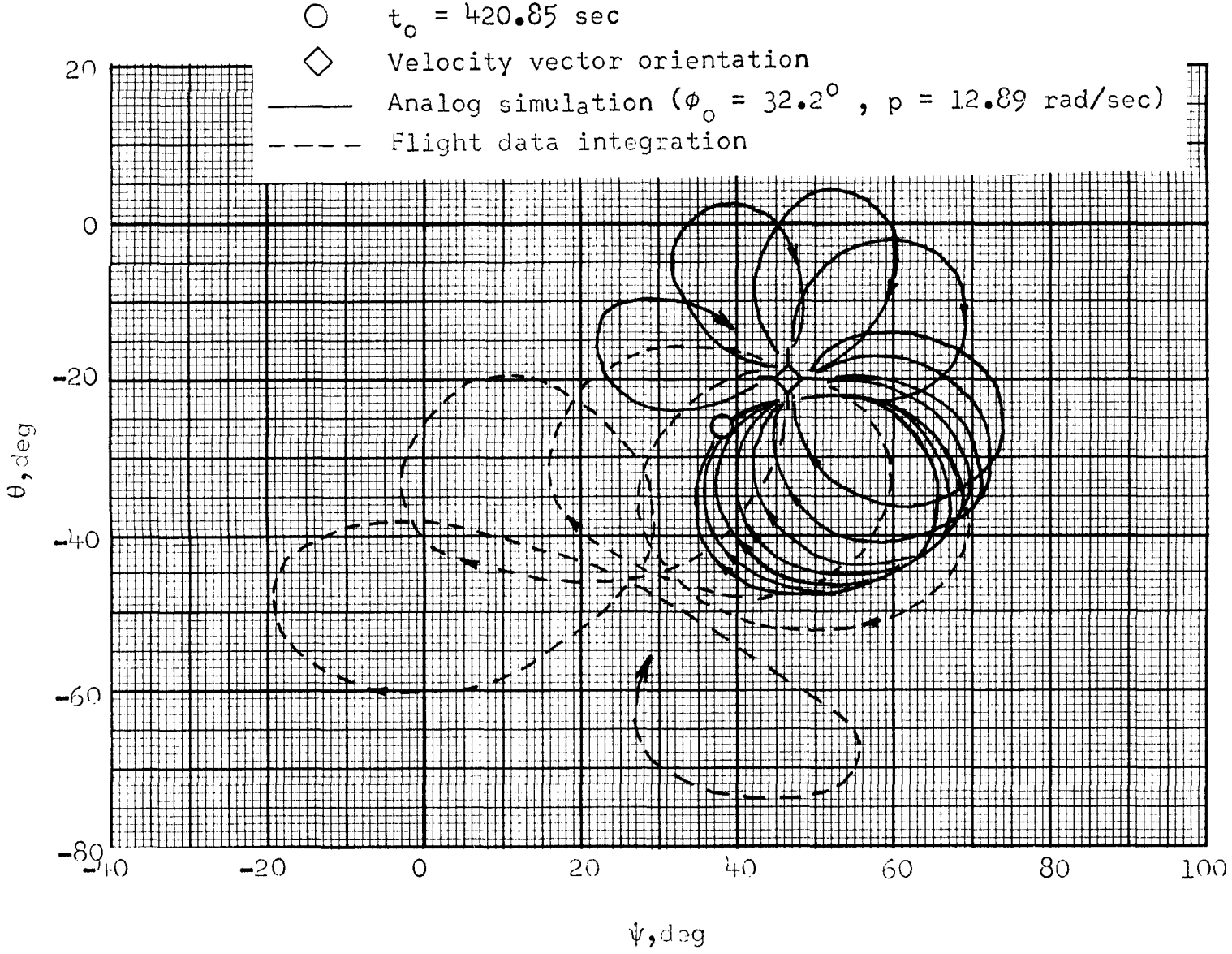

Figure 14.- Typical comparison of motions from flight data integration and analog simulation near fifth-stage burnout.

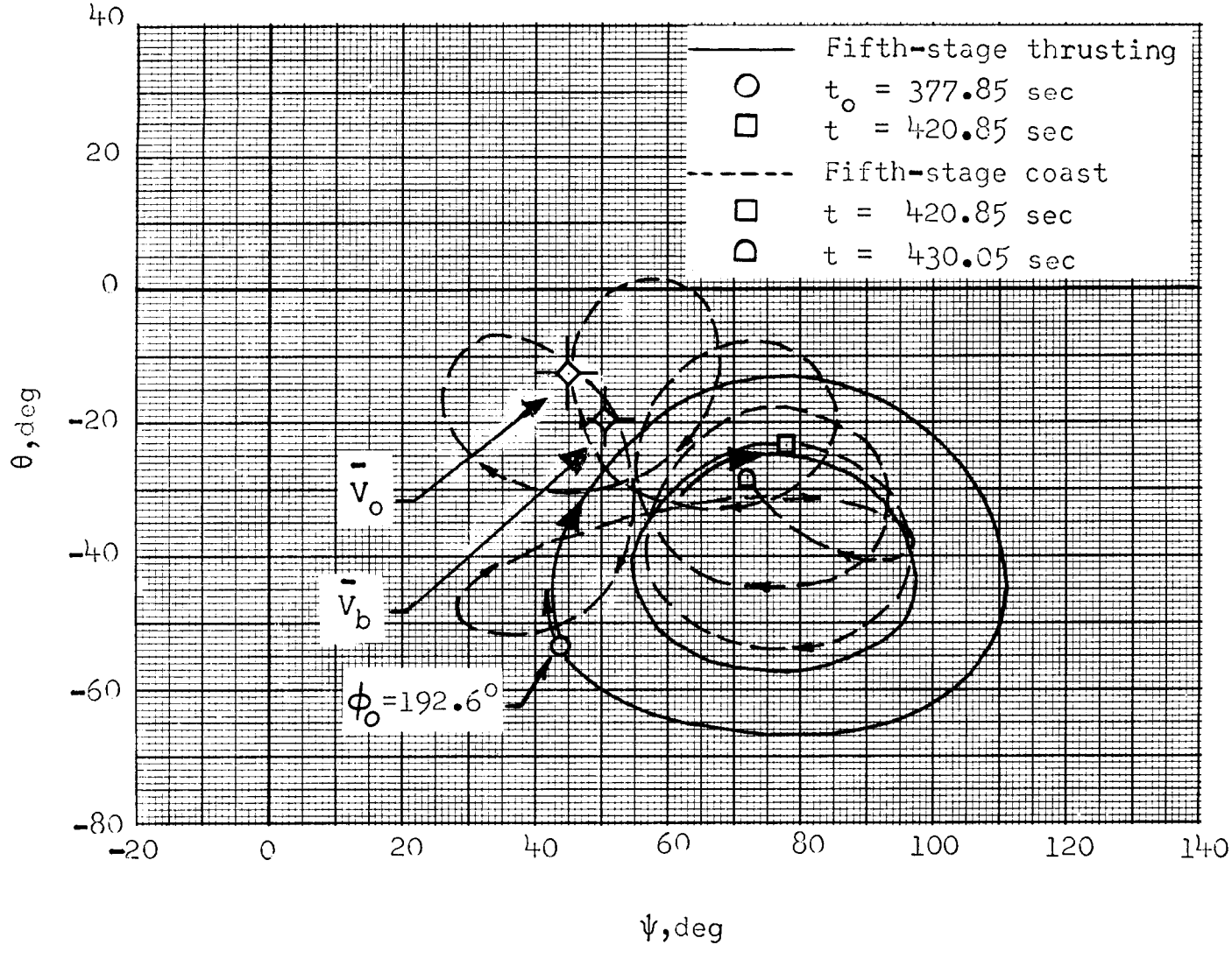

Figure 15.- Possible solution of trajectory and motions from flight data integration during fifth-stage thrusting.

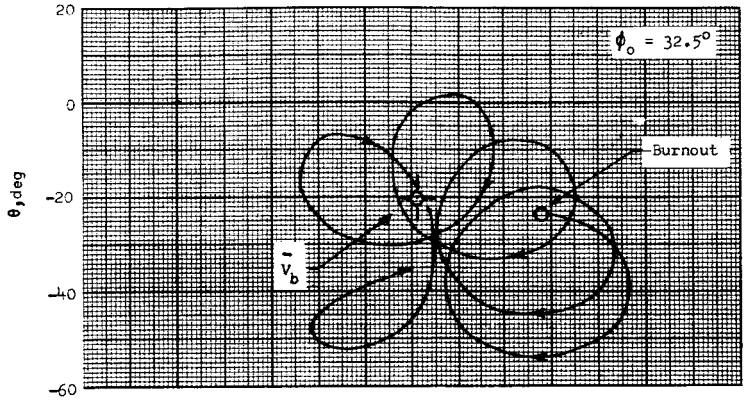

(a) Flight data integration (unfaired roll rate).

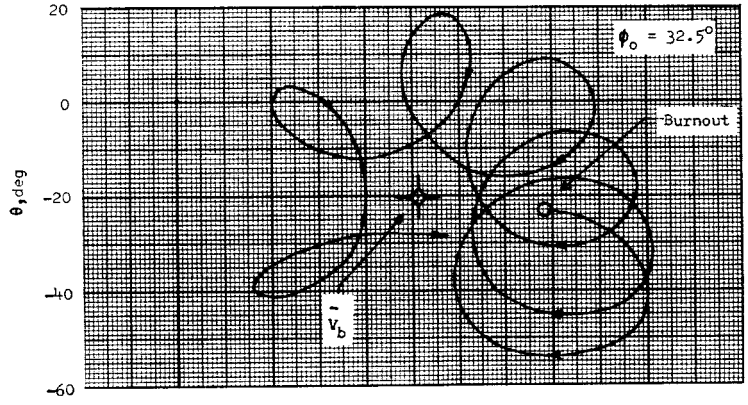

(b) Analog simulation (p = 12.3 rad/sec).

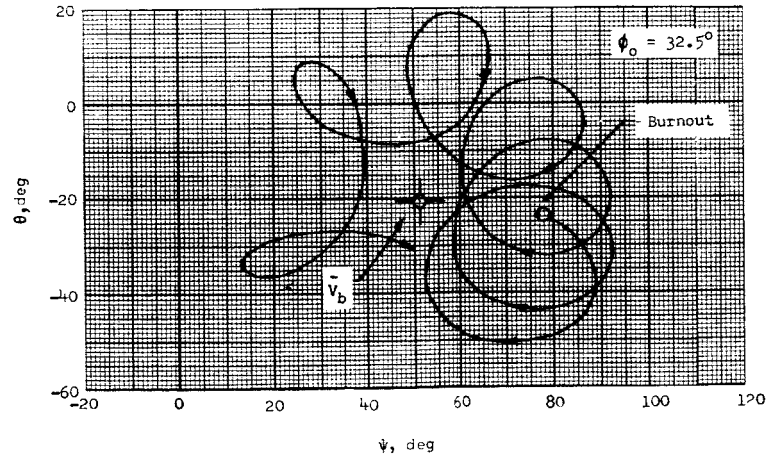

(c) Flight data integration (faired roll rate).

Figure 16.- Comparison of motions near burnout from flight data integration and analog simulation with faired and unfaired roll rates.

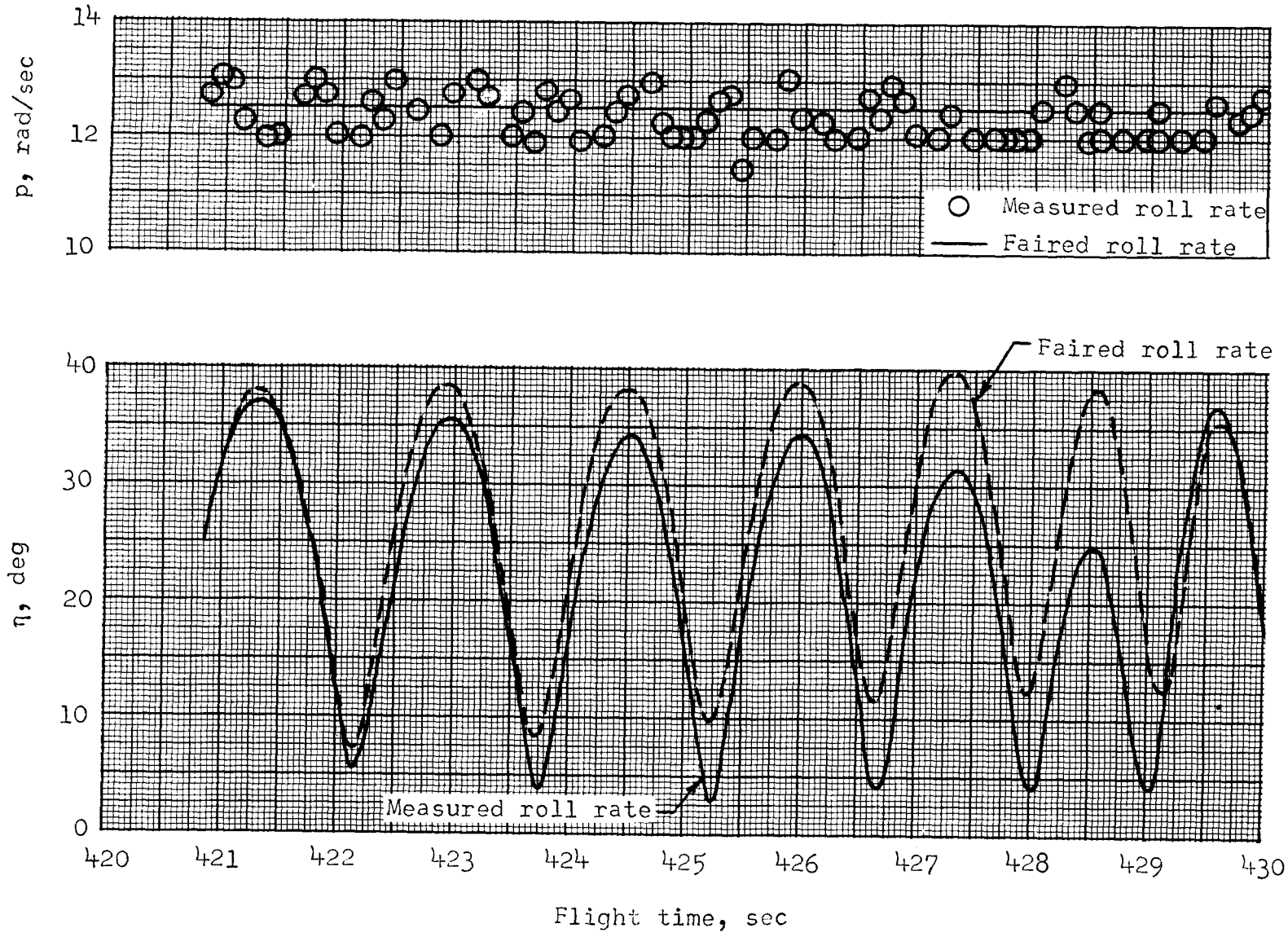

Figure 17.- Variation of computed resultant angle of attack with faired and unfaired roll-rate data.

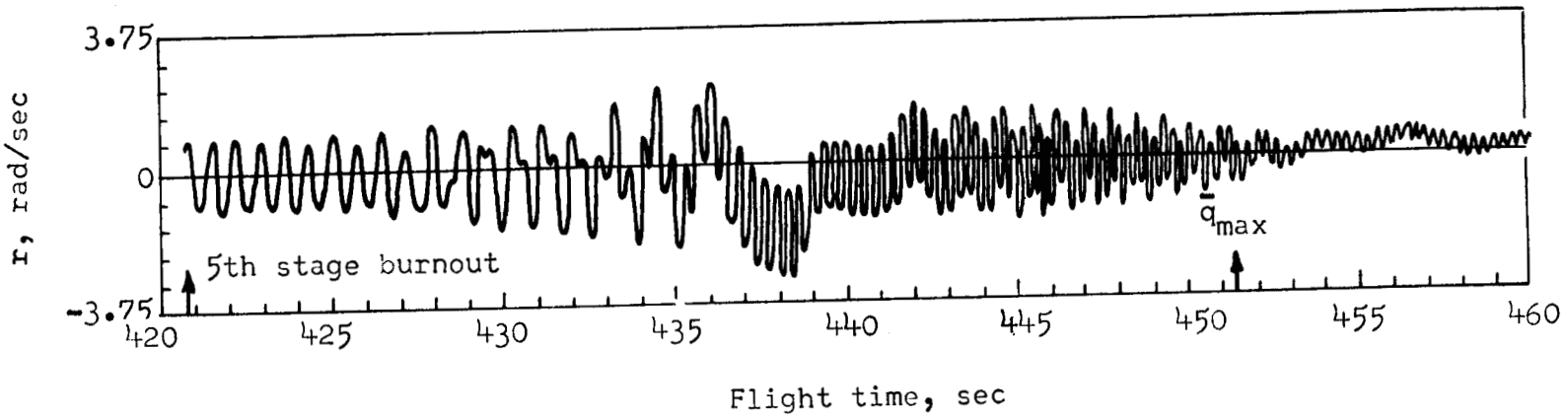

(a) Flight measurement.

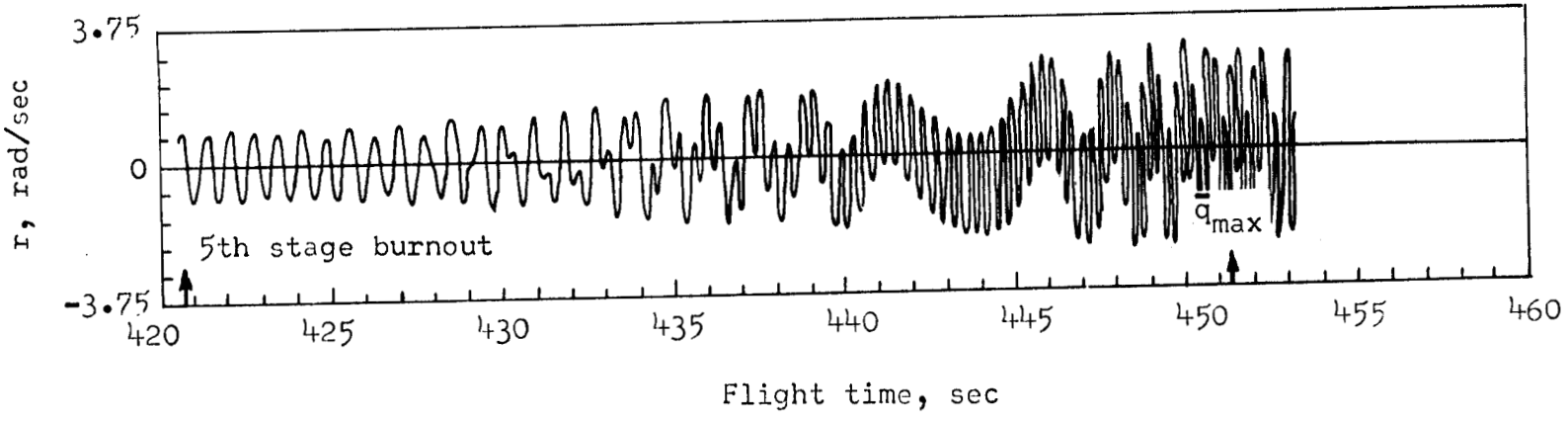

(b) Analog simulation.

Figure 18.- Comparison of analog simulation of yaw rate with flight measurement.

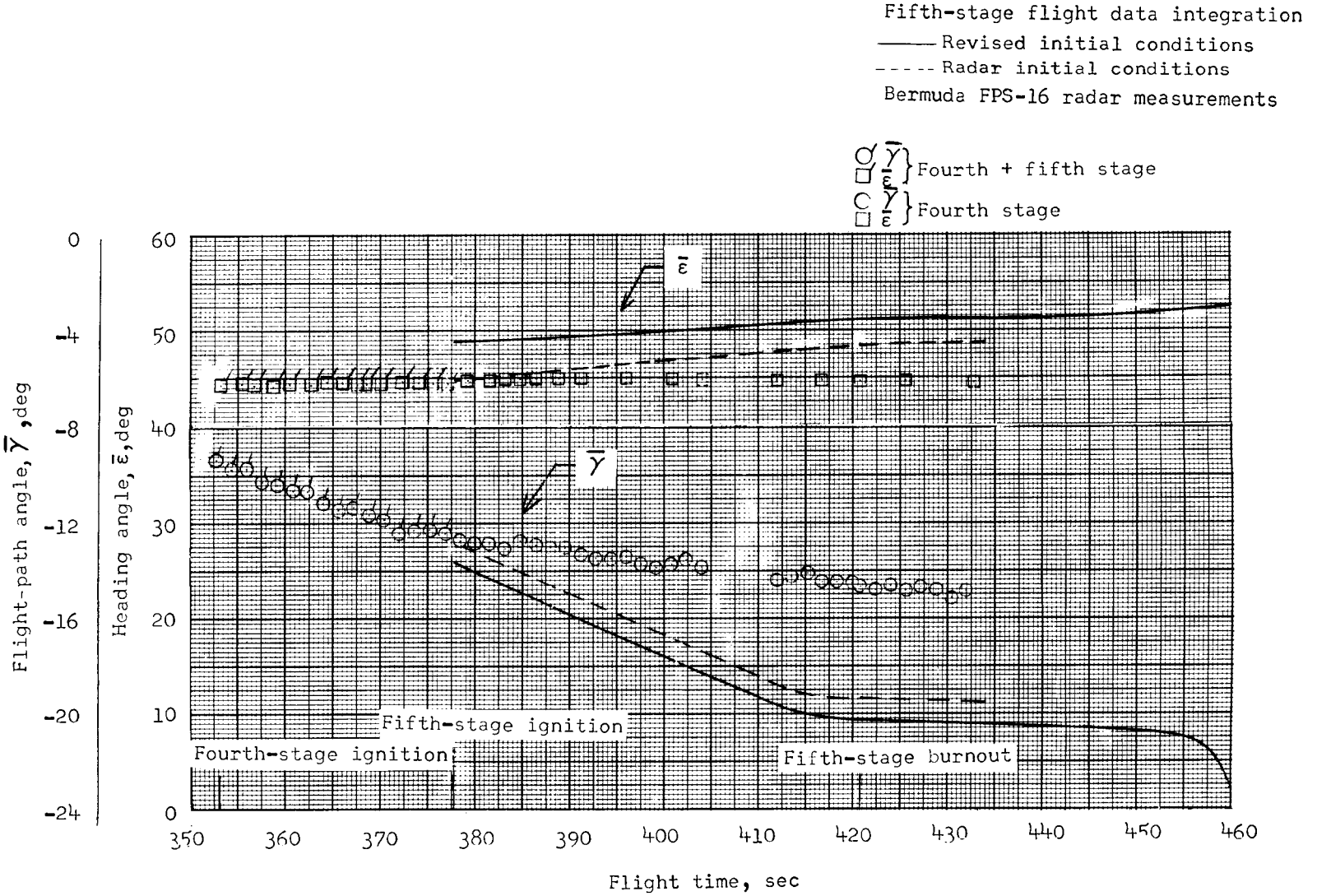

Figure 19.- Time histories of computed heading and flight-path angles.

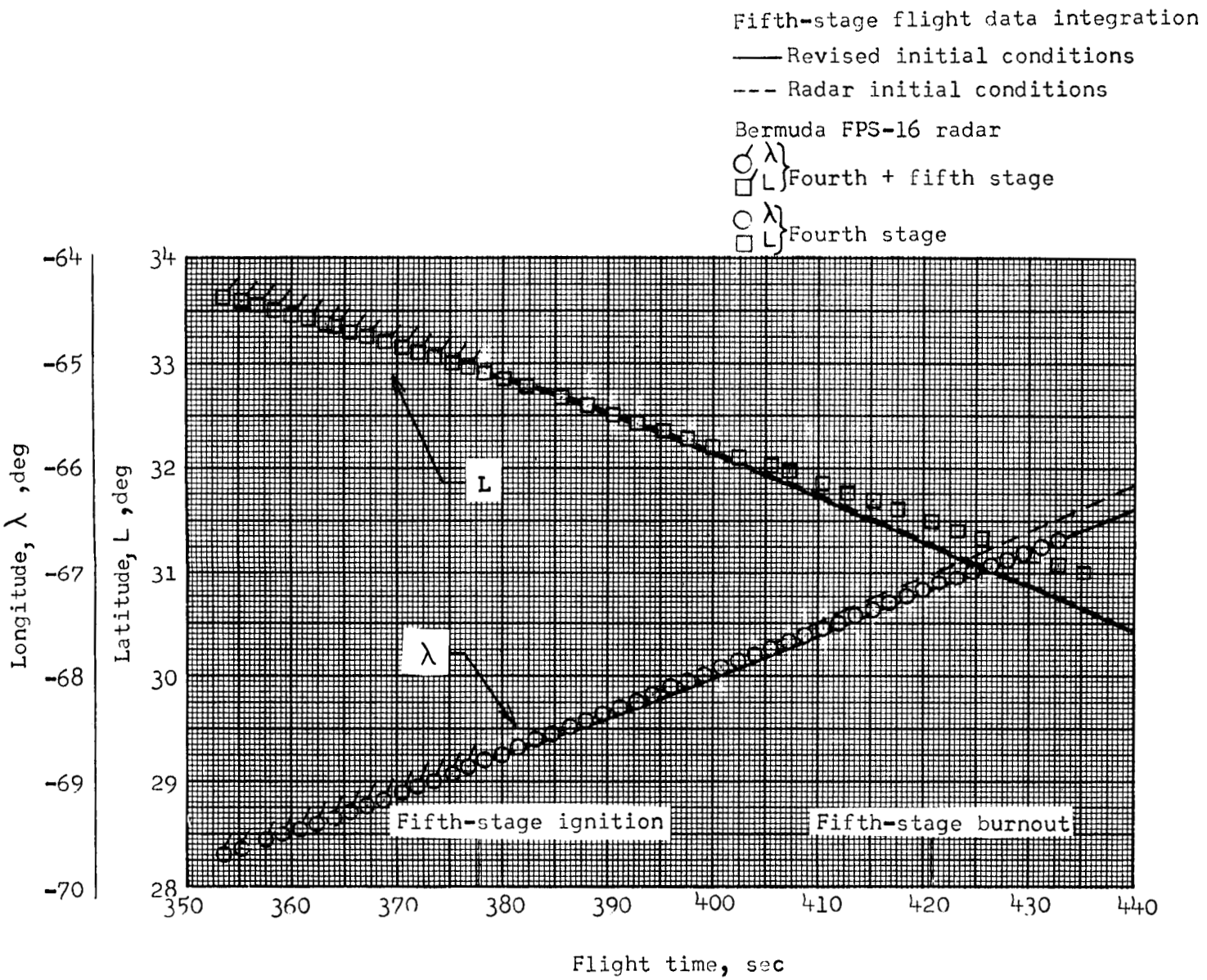

Figure 20.- Time histories of computed longitude and latitude.

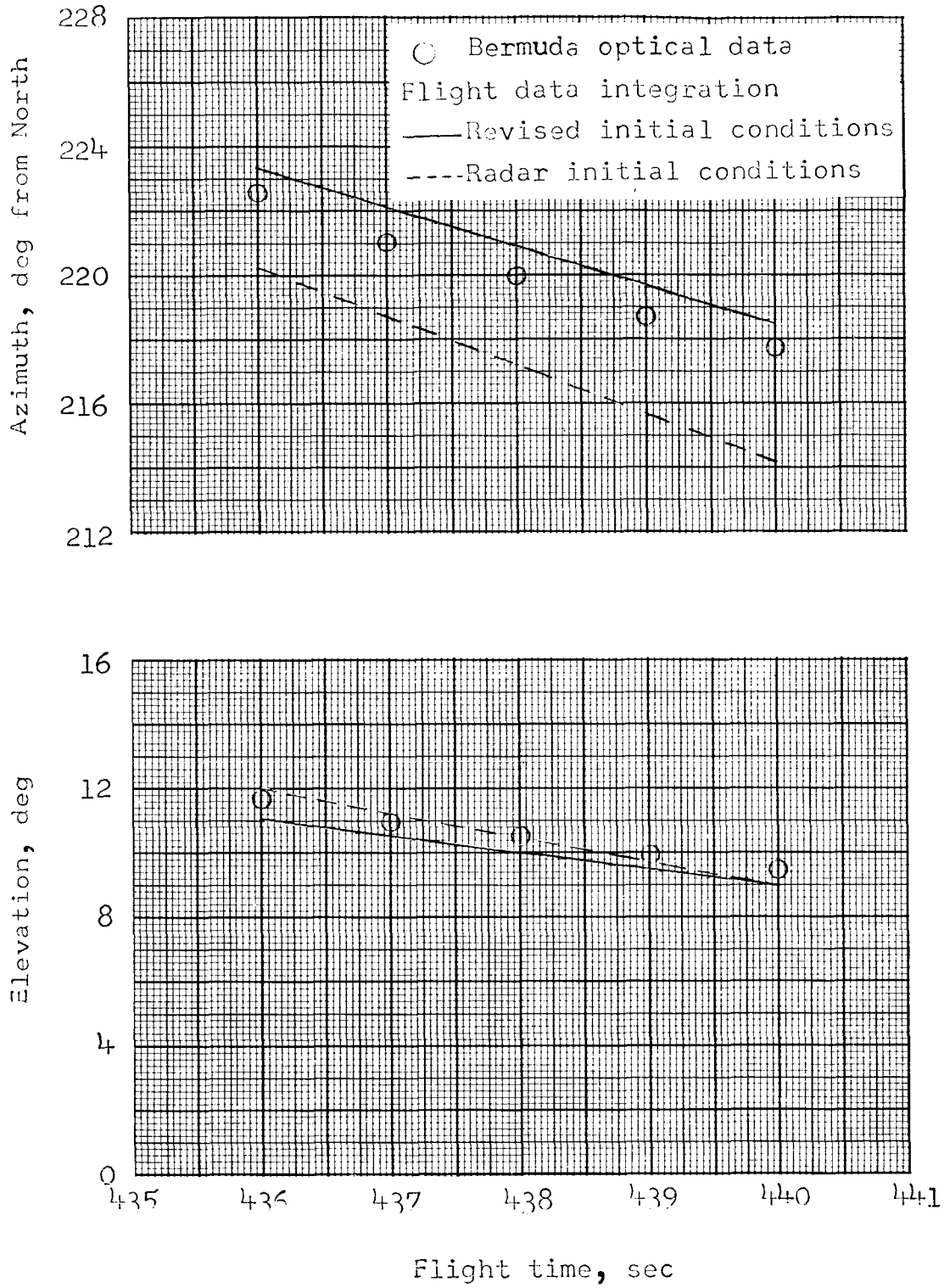

Figure 21.- Comparison of Bermuda optical tracking measurements with computed trajectory.

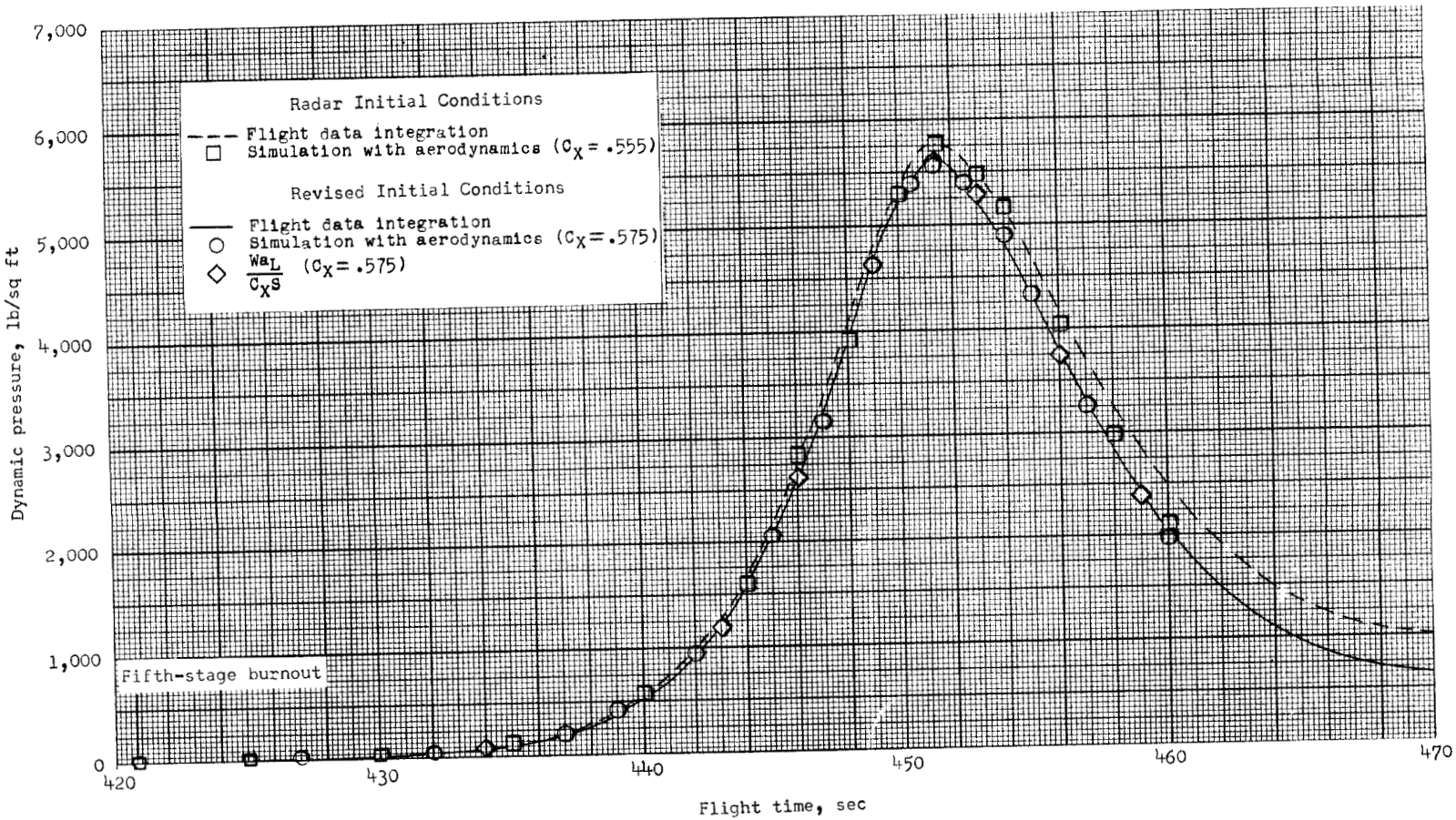

Figure 22.- Comparison of computed dynamic-pressure time histories.

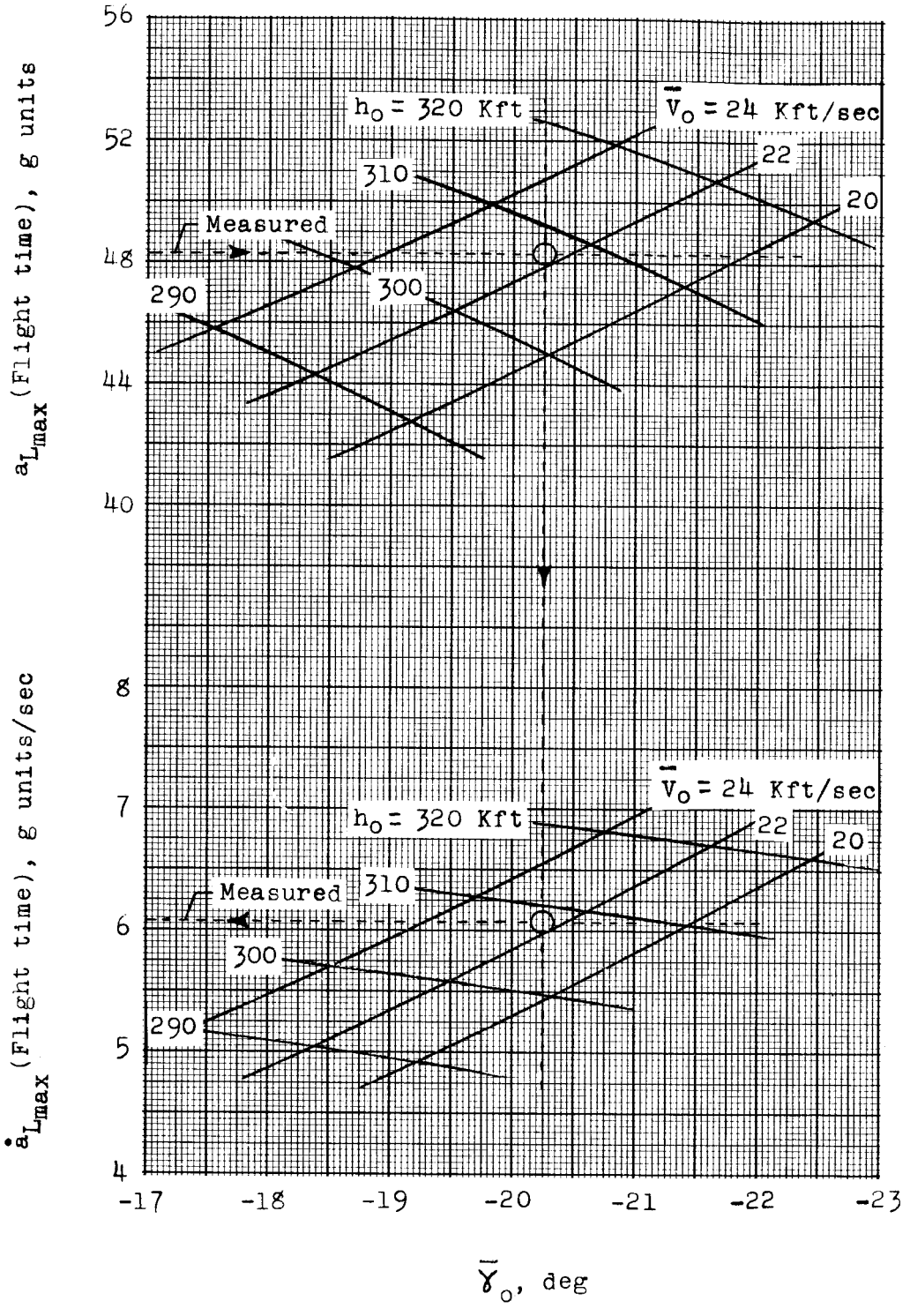

Figure 23.- Results of an analog initial-condition study at fifth-stage burnout. C_X = 0.575.

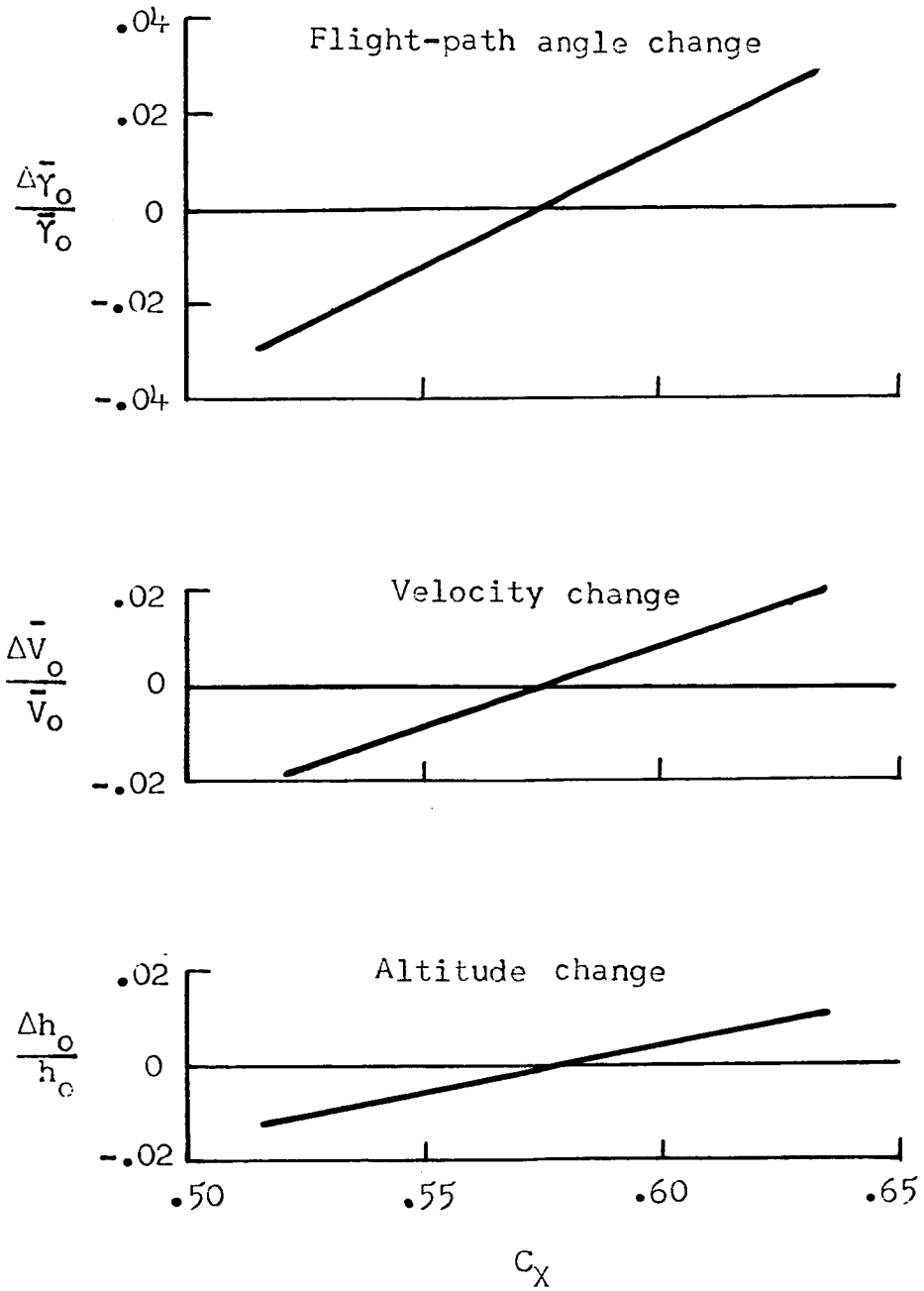

Figure 24.- Changes in burnout flight-path angle, velocity, and altitude with longitudinal-force-coefficient errors.

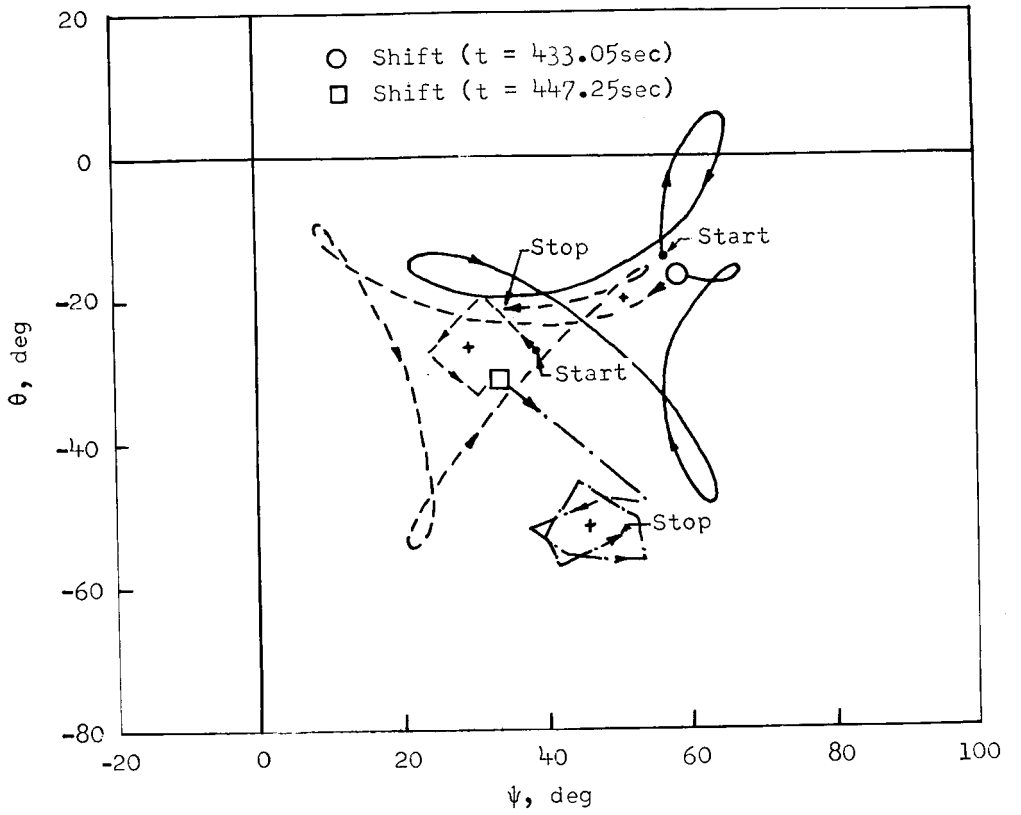

(a) Euler angle displacement.

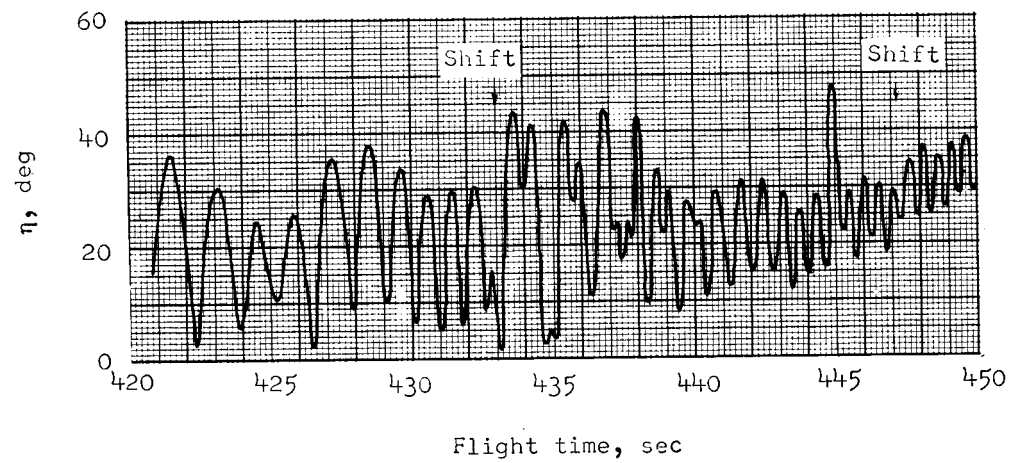

(b) Resultant angle-of-attack displacement.

Figure 25.- Shifts in Euler angles and resultant angle of attack during integration of flight data.

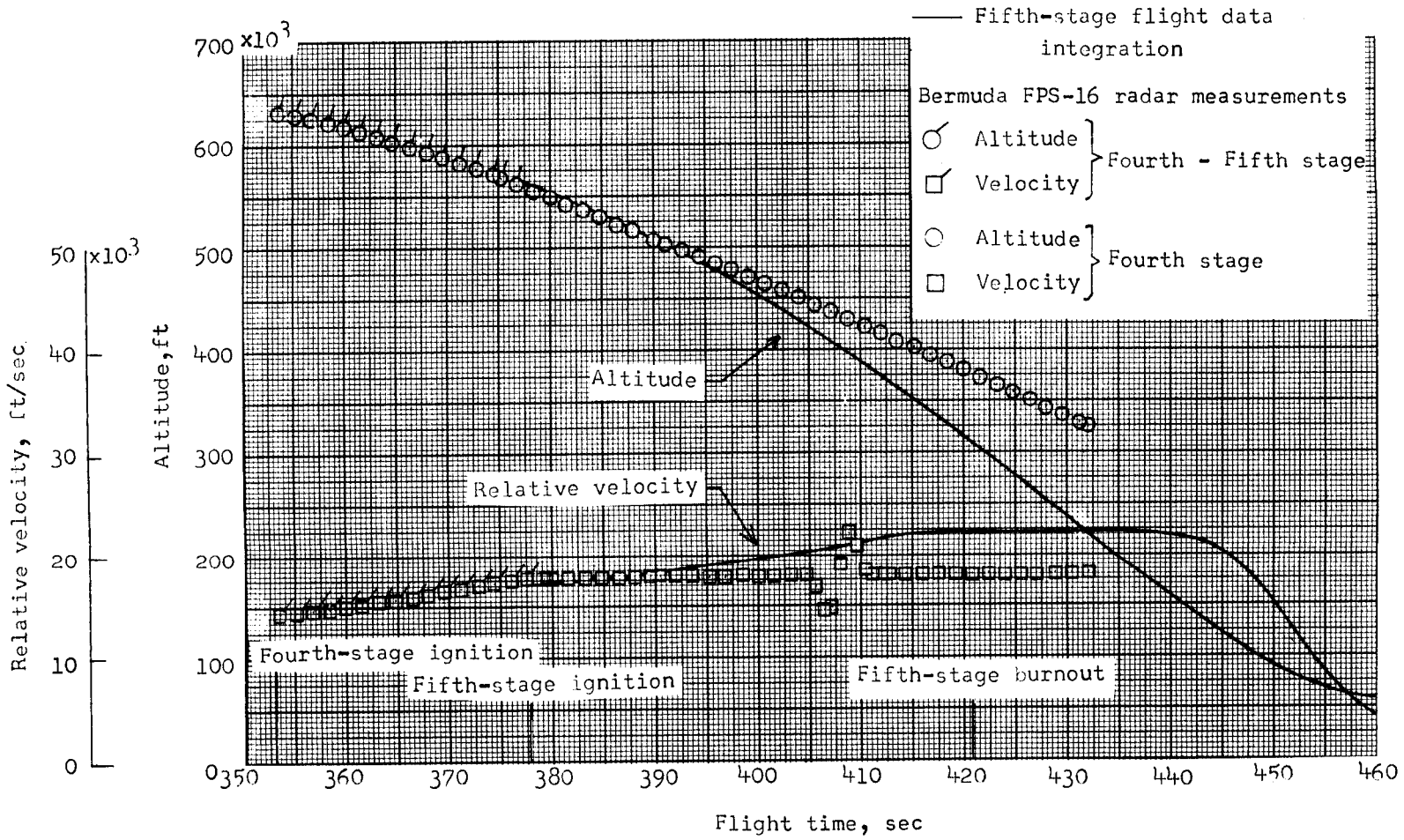

Figure 26.- Time histories of computed velocity and altitude.

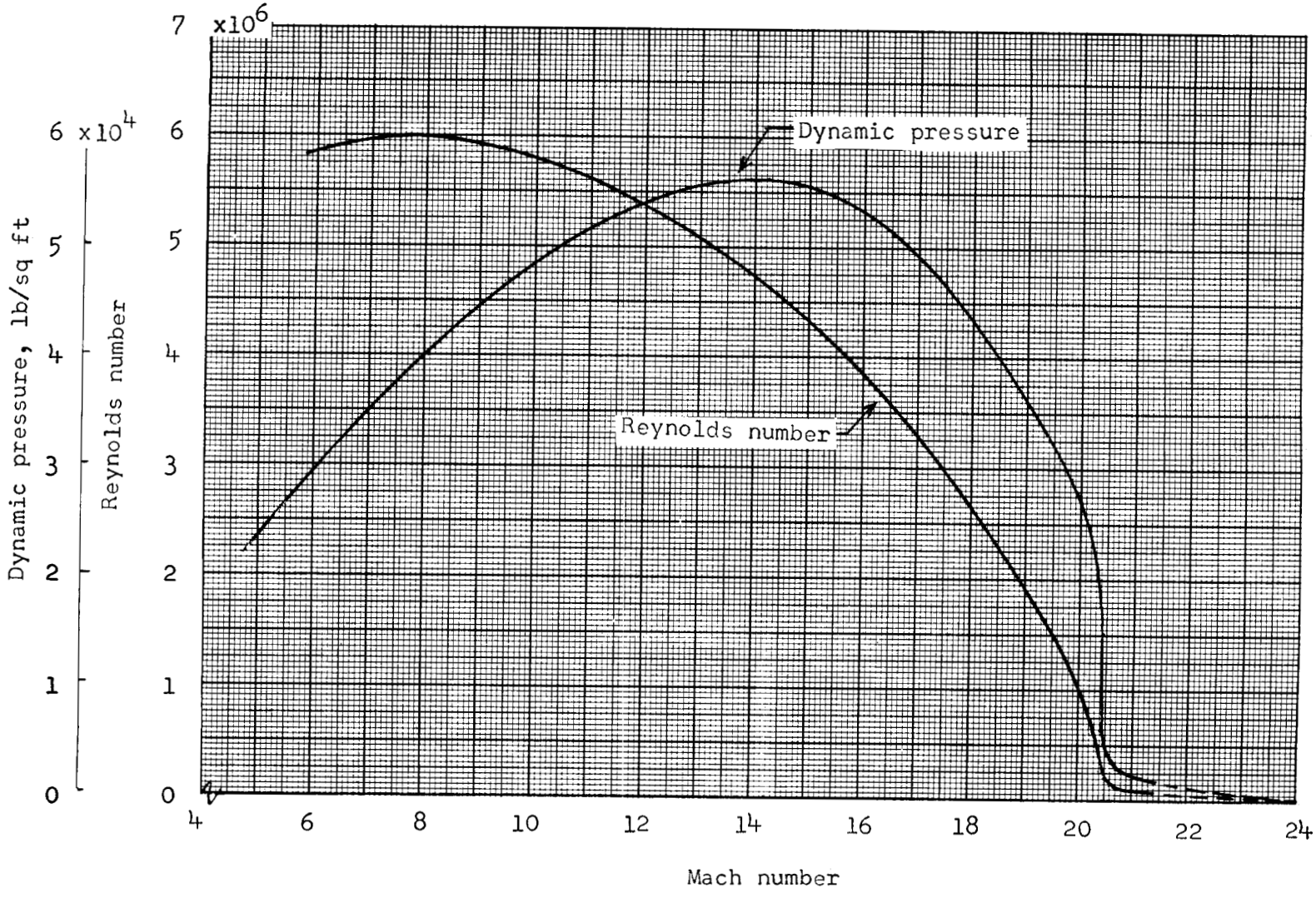

Figure 27.- Variation of computed Reynolds number and dynamic pressure with free-stream Mach number.

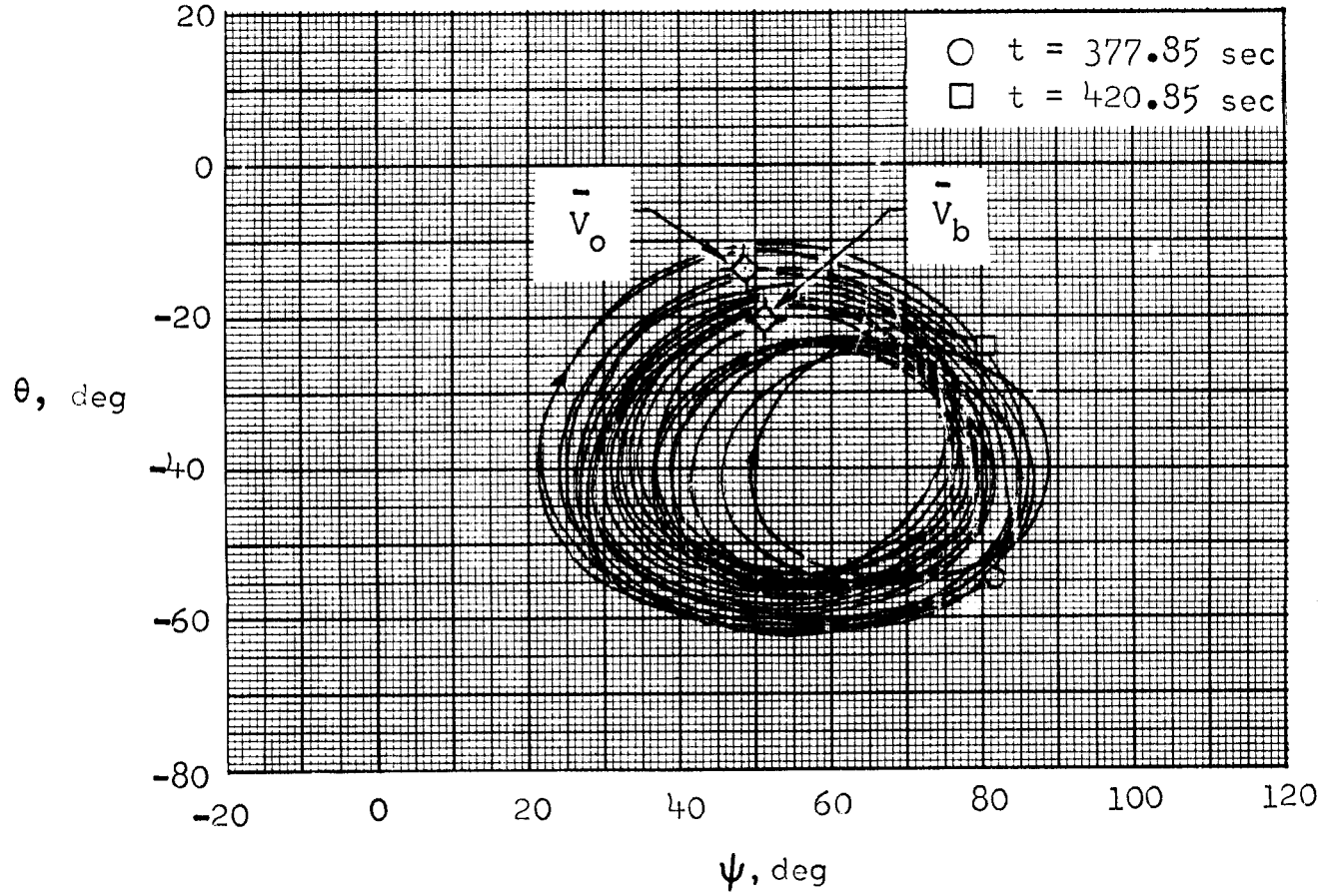

(a) Fifth-stage thrusting (t = 377.85 to 420.85 sec).

Figure 28.- Computed spacecraft motions.

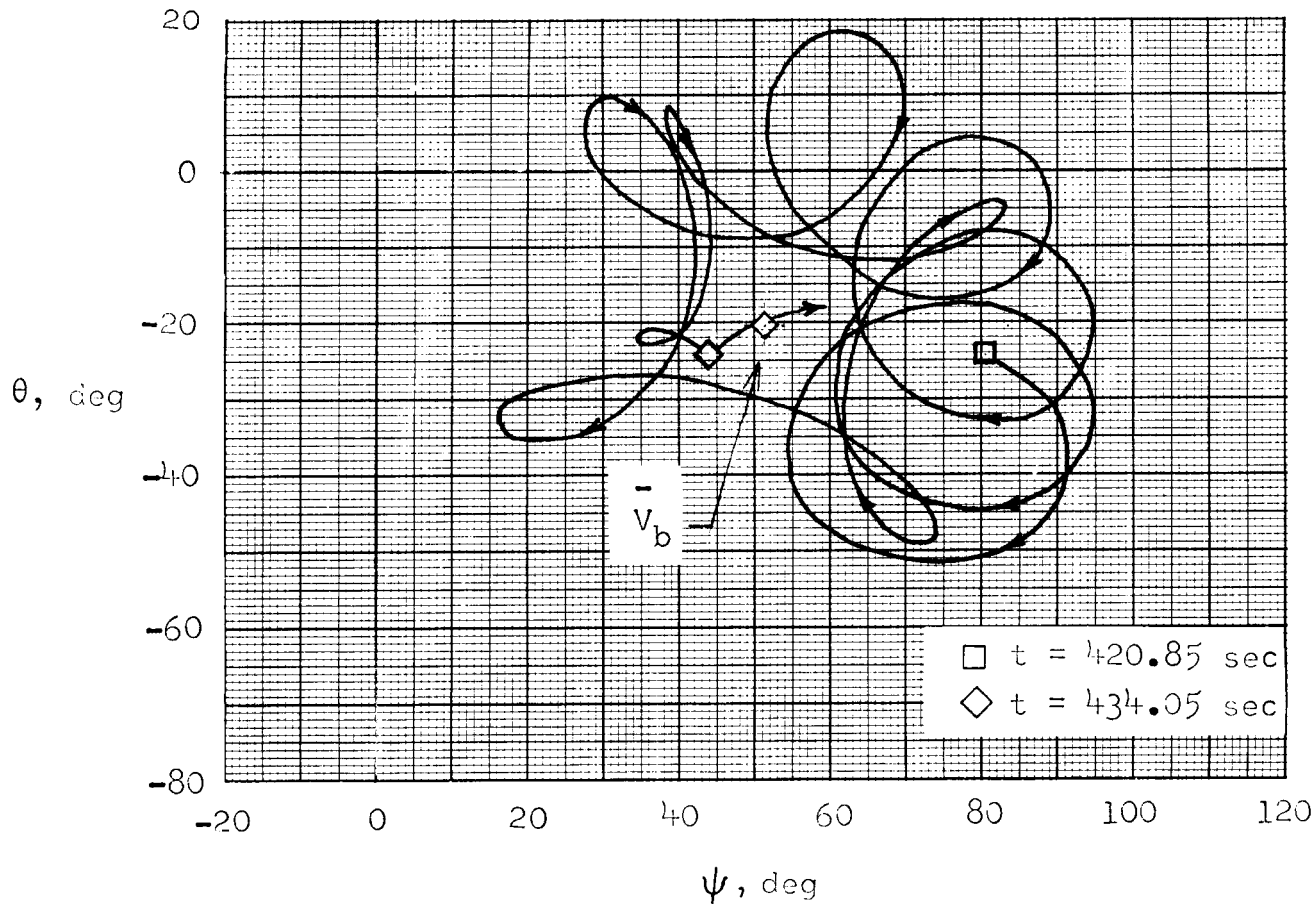

(b) Coasting (t = 420.85 to 434.05 sec).

Figure 28.- Continued.

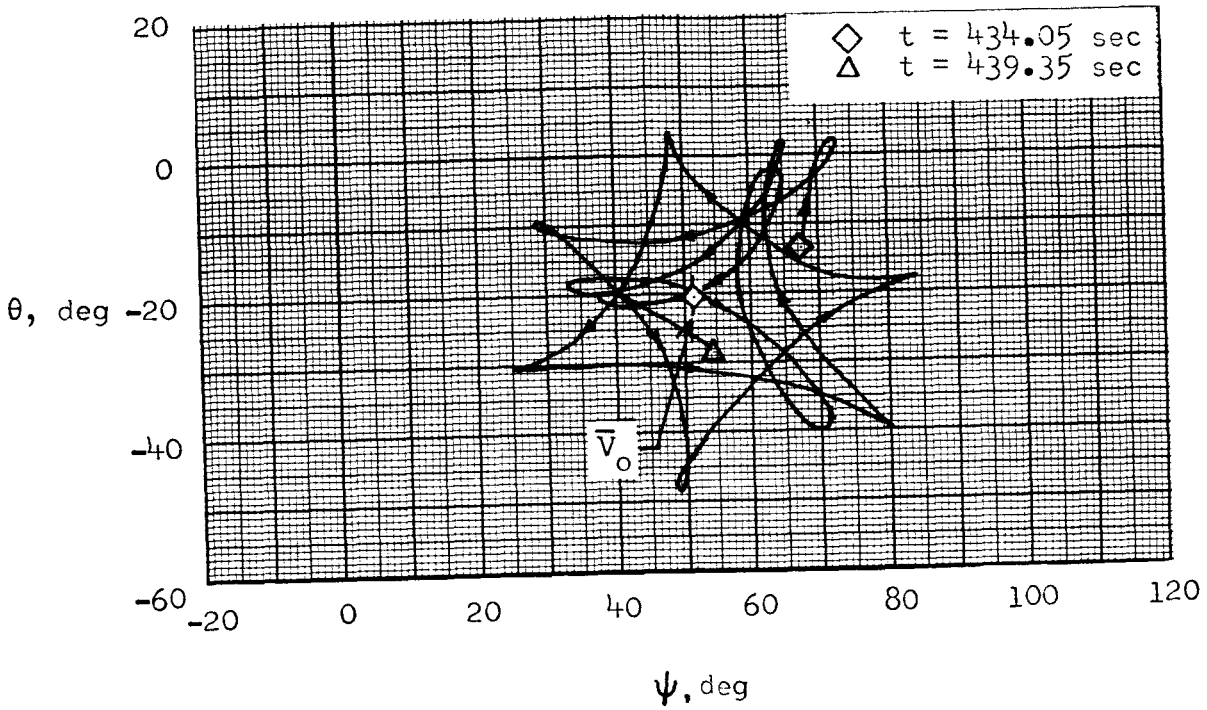

(c) Nose cap burnoff (t = 434.05 to 439.35 sec).

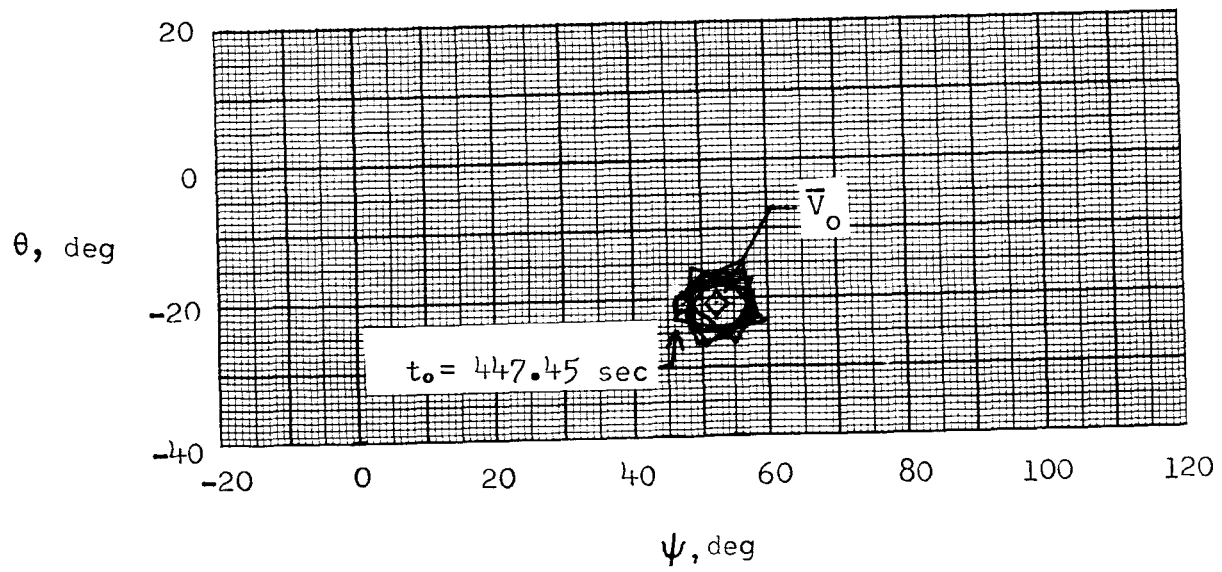

(d) Near maximum dynamic pressure (t = 447.45 to 451.35 sec).

Figure 28.- Concluded.

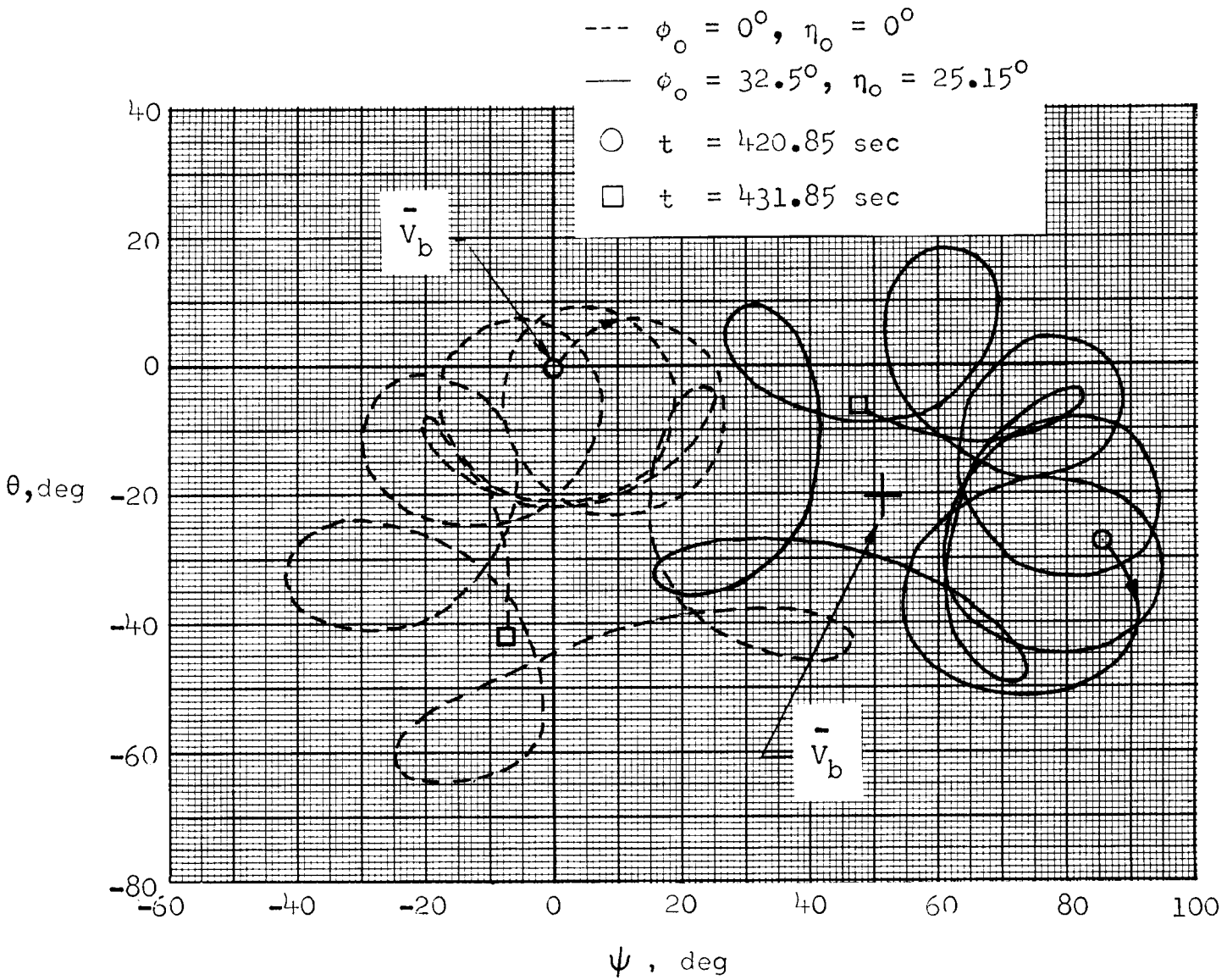

Figure 29.- Rotation and translation of basic motion pattern at burnout.

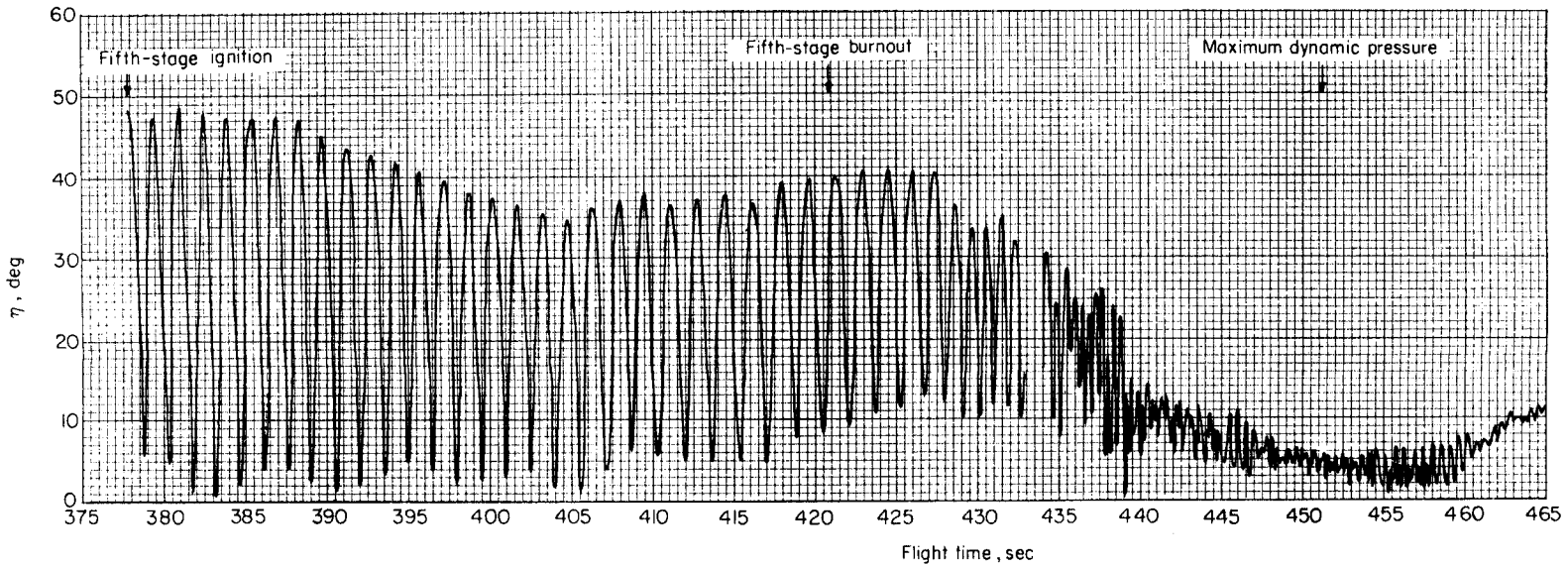

Figure 30.- Time history of spacecraft computed resultant angle of attack.

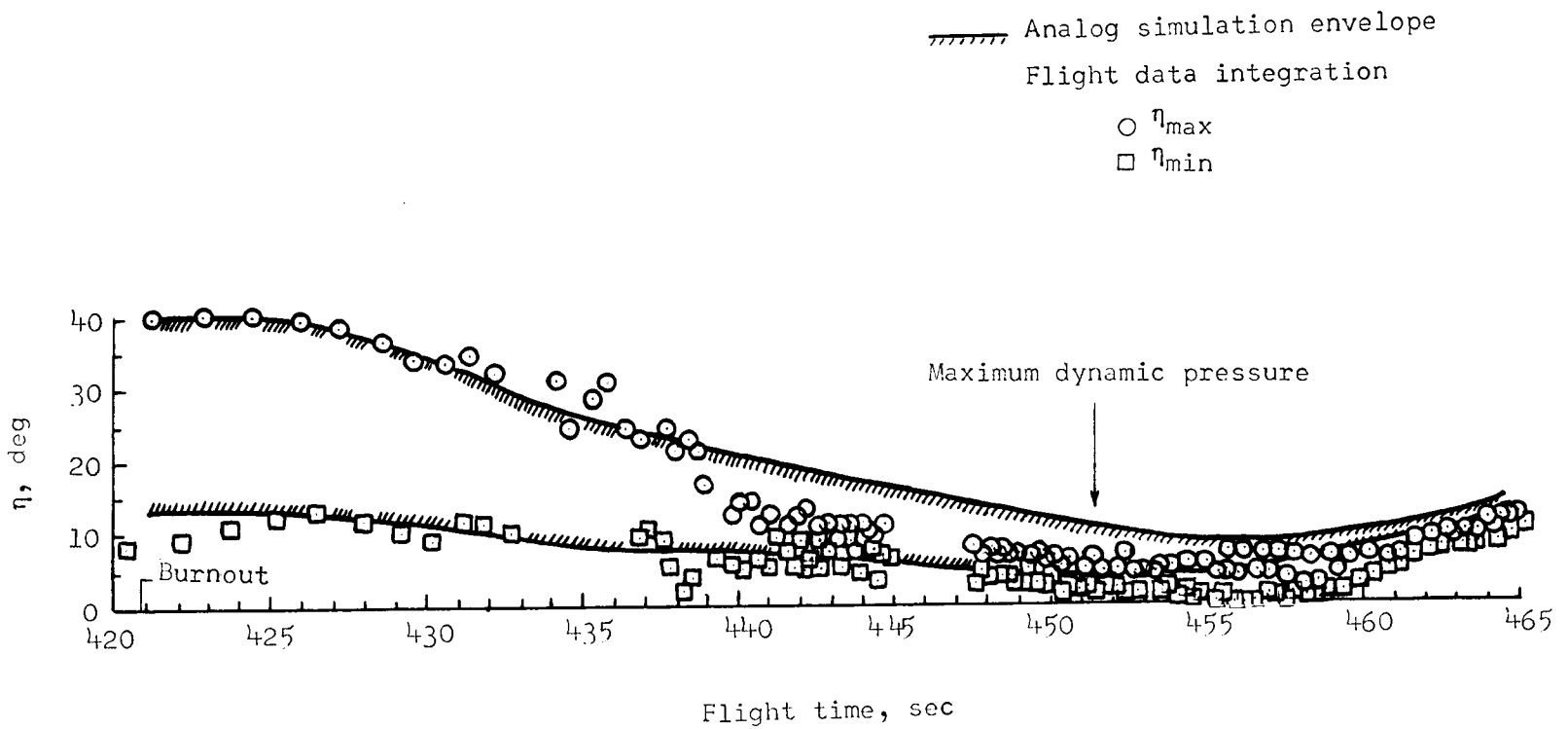

Figure 31.- Comparison between computed resultant angle-of-attack envelopes.

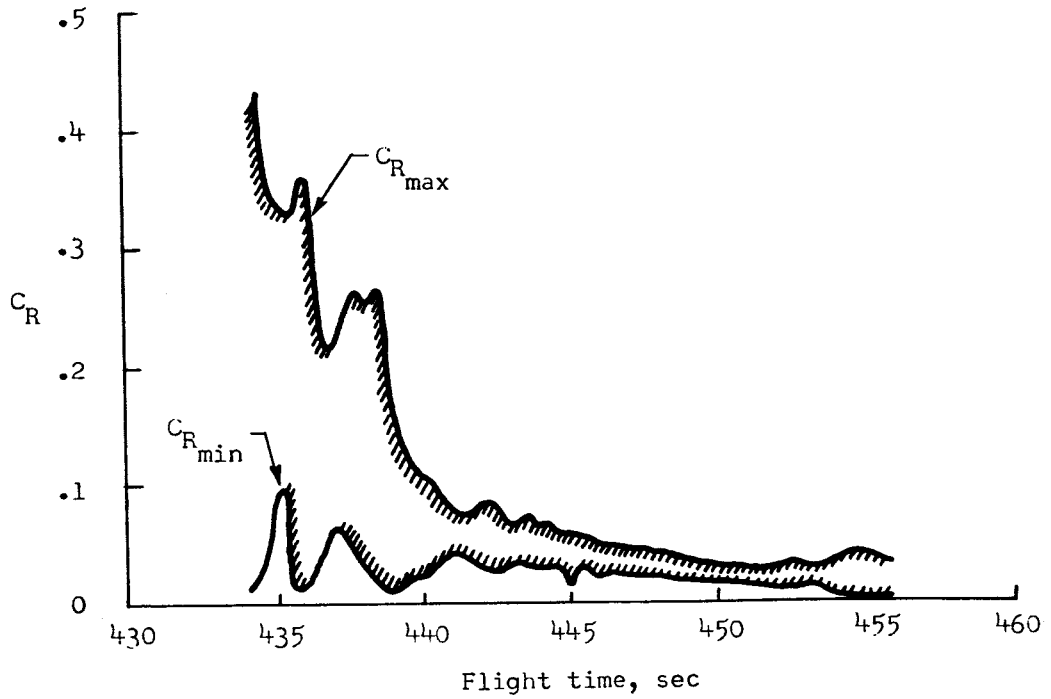

(a) Time history of resultant force-coefficient envelope.

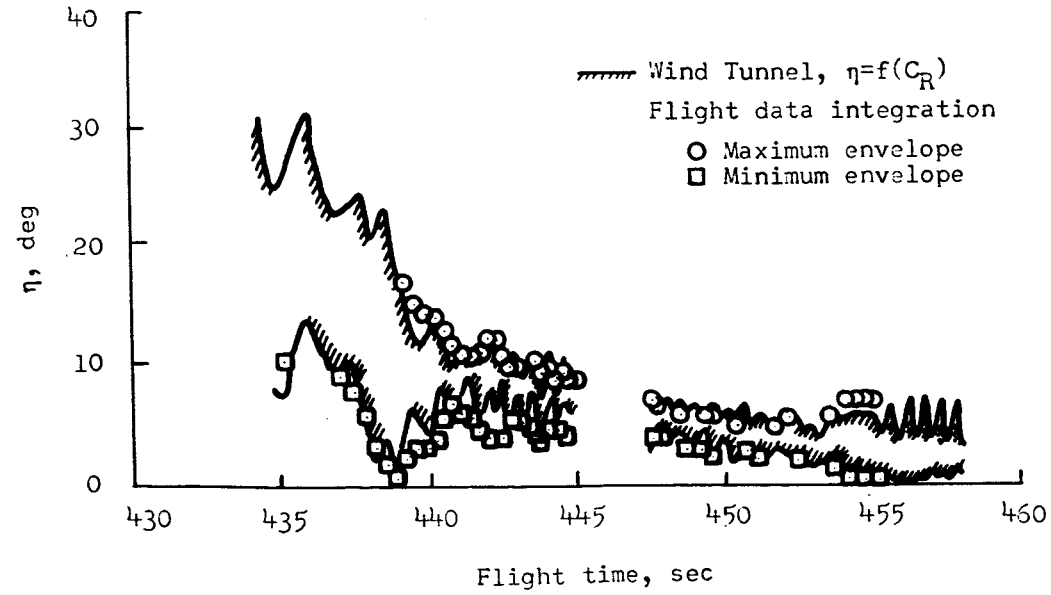

(b) Comparison of resultant angle-of-attack envelopes.

Figure 32.- Time history of resultant-force coefficient and comparison between computed resultant angles of attack.

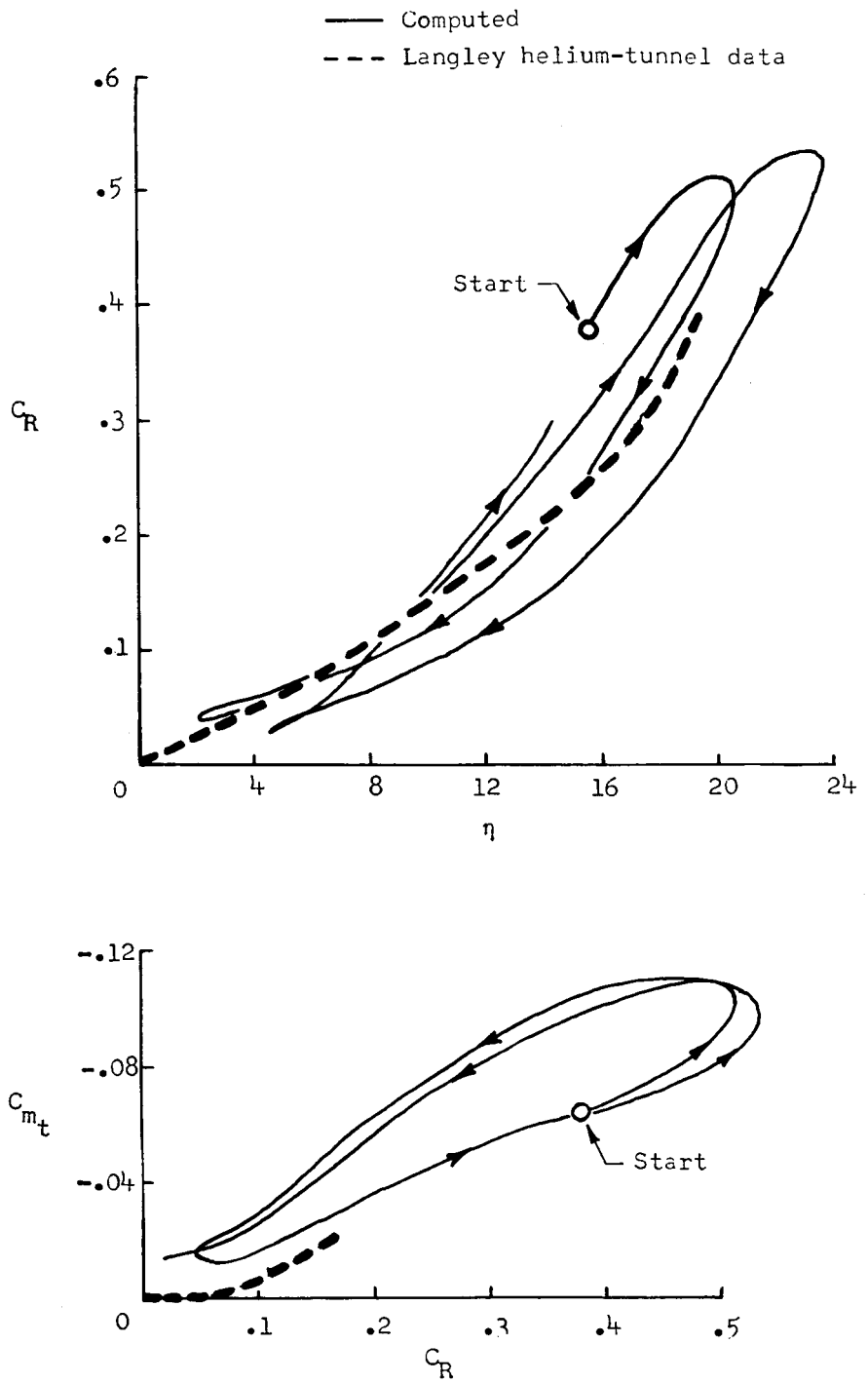

(a) Cap on at Mach number 20.65 (t = 437.95 to 438.63 sec).

Figure 33.- Comparison between wind-tunnel and computed flight resultant force and moment coefficients.

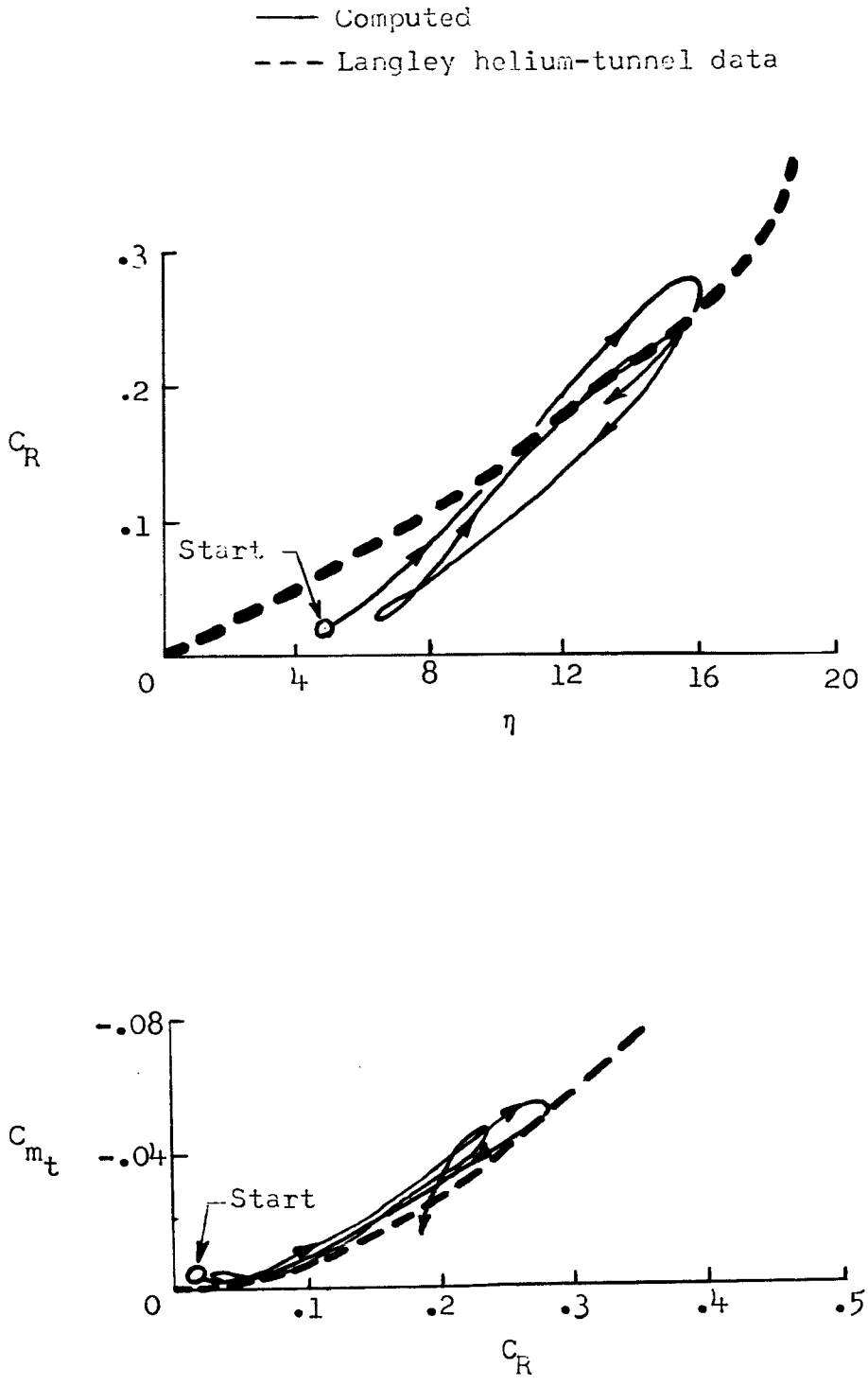

(b) Cap off at Mach number 20.52 (t = 438.97 to 439.53 sec).

Figure 33.- Continued.

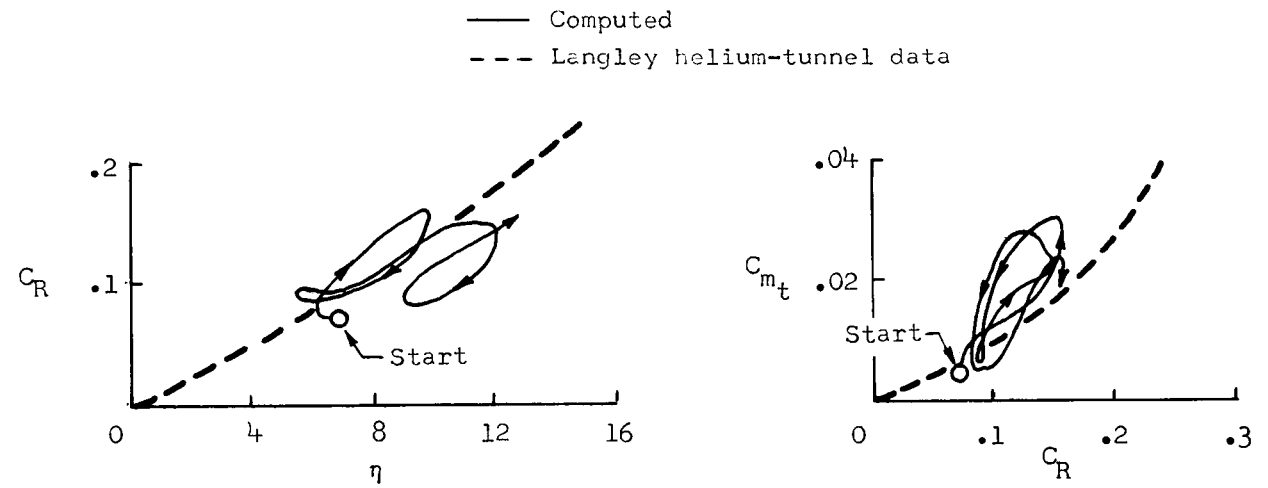

(c) Mach number 20.43 (t = 440.61 to 441.35 sec).

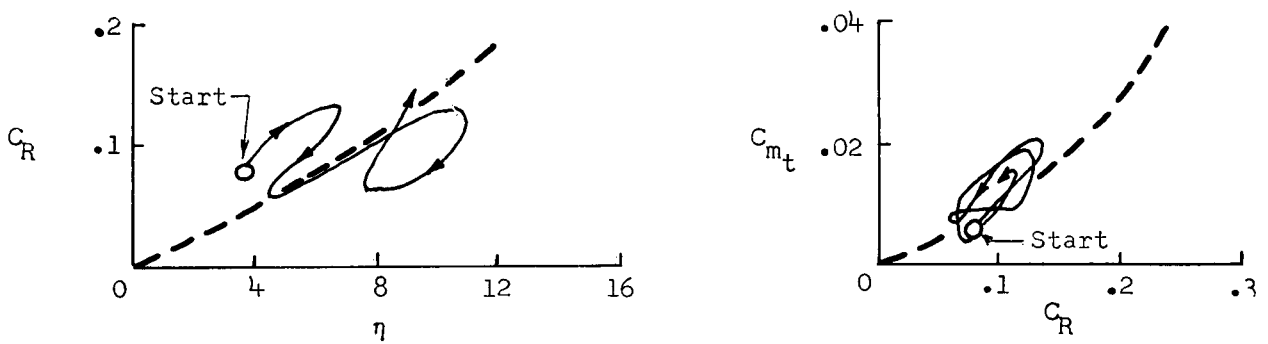

(d) Mach number 20.43 (t = 443.81 to 444.35 sec).

Figure 33.- Continued.

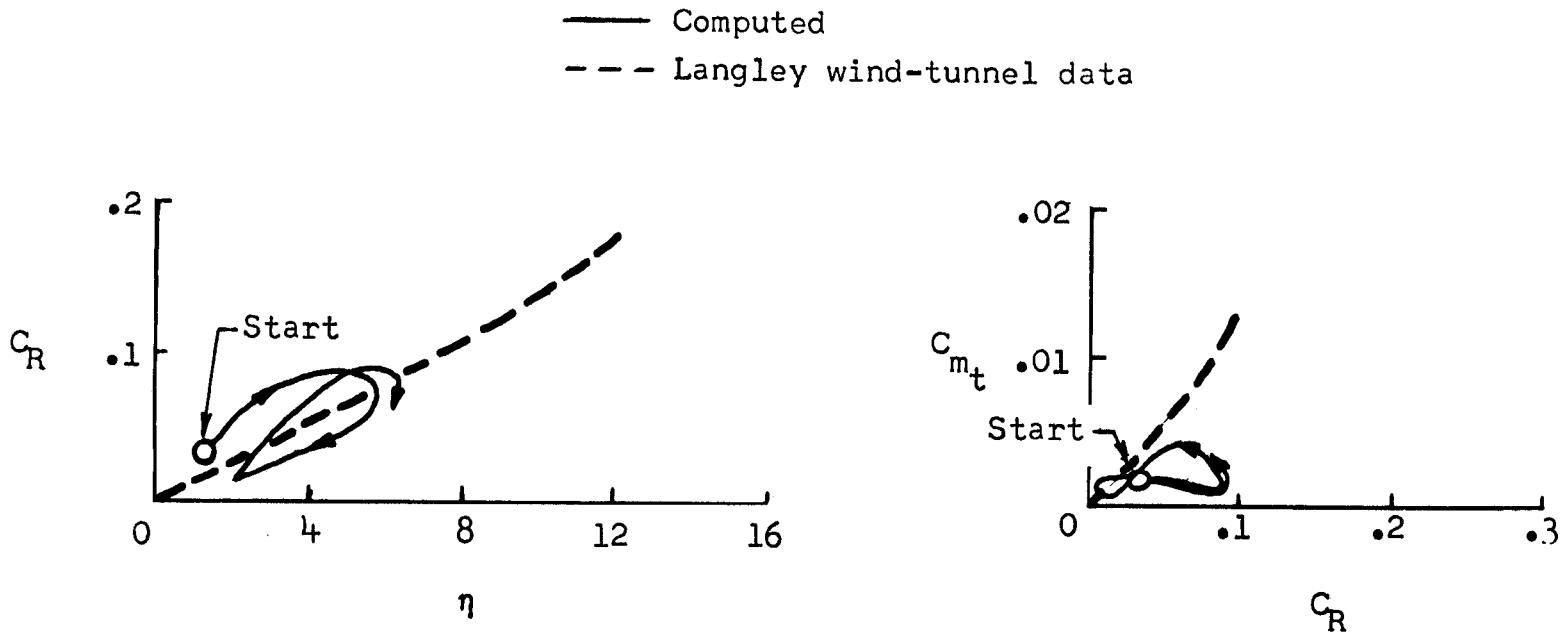

(e) Mach number 9.74 (t = 454.11 to 454.43 sec).

Figure 33.- Concluded.

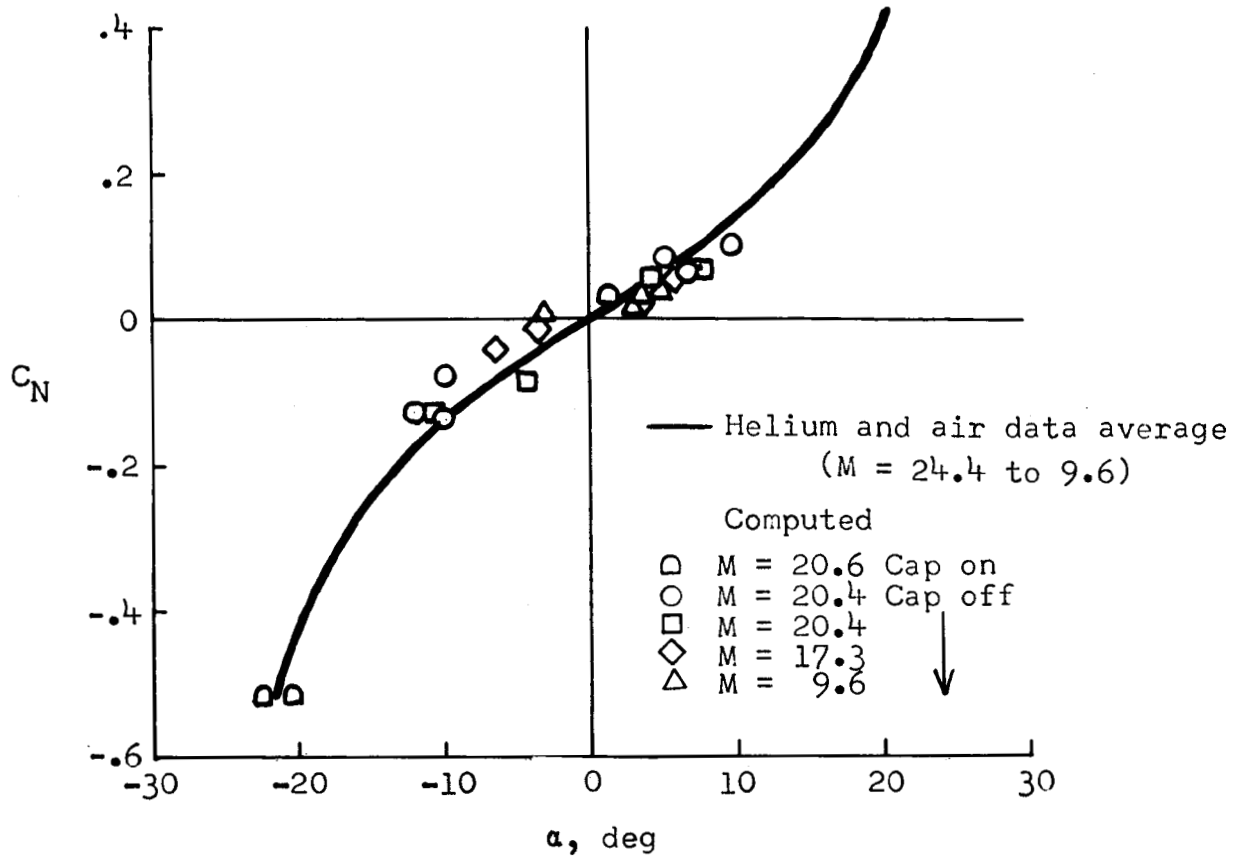

(a) Comparison of normal-force coefficient at $\beta = 0^{\circ}$.

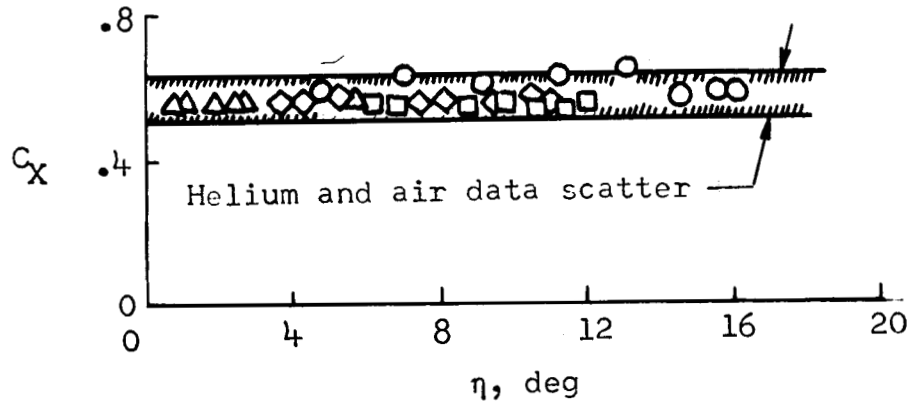

(b) Comparison of longitudinal-force coefficient from M = 24.4 to 9.6.

Figure 34.- Comparison of normal- and longitudinal-force coefficients at oscillation peaks.

NASA-Langley, 1965 L-4239